UNIVERSITY OF CALGARY

Elastic wave modelling and reverse-time migration by a staggered-grid finite-difference method

by

Zaiming Jiang

A THESIS

SUBMITTED TO THE FACULTY OF GRADUATE STUDIES

IN PARTIAL FULFILLMENT OF THE REQUIREMENTS FOR THE

DEGREE OF DOCTOR OF PHILOSOPHY

DEPARTMENT OF DEPARTMENT OF GEOSCIENCE

CALGARY, ALBERTA

September, 2012

UNIVERSITY OF CALGARY

FACULTY OF GRADUATE STUDIES

The undersigned certify that they have read, and recommend to the Faculty of Graduate Studies for acceptance, a thesis entitled "Elastic wave modelling and reverse-time migration by a staggered-grid finite-difference method" submitted by Zaiming Jiang in partial fulfillment of the requirements for the degree of DOCTOR OF PHILOSOPHY.

Supervisor, Dr. John C. Bancroft
Dept. of Geoscience

Co-supervisor, Dr. Laurence R. Lines
Dept. of Geoscience

Dr. Gary F. Margrave
Dept. of Geoscience

Dr. Michael P. Lamoureux
Dept. of Mathematics and Statistics

Dr. Jalel Azaiez
Dept. of Chemical and Petroleum Engineering

External Examiner, Dr. Matthew Yedlin
University Of British Columbia

Date

Abstract

Four aspects of reverse-time migration are discussed. They are wave modelling, computational boundaries, reverse-time migration algorithms, and computational resources.

Wave modelling is a part of reverse-time migration. Finite-difference methods based on staggered-grid schemes are studied to model wave phenomena in elastic media. Modelled wave cases include 1D P-wave, 2D SH-wave, 2D P-SV wave and 3D-wave cases, and analyzed wave phenomena and seismic problems include wave velocity, wavelength, geometrical spreading, seismic resolution, surface boundary, seismic reflection, transmission, and diffraction, different situations of head waves, guided waves, Rayleigh waves, rigid boundaries, and so on. It is found that the modelling results are usually faithful to the real world and are consistent with seismic theories.

The computational boundary problem has been a persistent topic in the literature of wave modelling. After examining two of the most popular solutions to the problem, absorbing boundary conditions, and a nonreflecting boundary condition, a method of combining these two solutions is proposed. The proposed method results in fewer boundary reflections with little computational cost.

Reverse-time migration is the heart of the dissertation. There are three special features of the method studied in the dissertation. One feature is the finite-difference method employed. People have practiced wave modelling on both non-staggered and staggered grids, but they rarely use staggered-grid schemes in reverse-time migration despite the known advantages the staggered-grid schemes. This dissertation applies

a staggered-grid scheme to reverse-time migration. The second feature about the migration method is a new method of imaging conditions for elastic reverse-time migration, which is referred to as 'source energy normalized imaging conditions'. The third feature is the reverse-time migration workflow for multicomponent seismic data processing. It is unique in some way. For example, ground roll suppression is not a necessary part in the workflow.

High demands of computational resources pose challenges and are a drawback for finite-difference depth migration methods. On this topic, the dissertation briefly discusses parallel computing and the problem of disk space.

Acknowledgements

I am grateful to the faculty, staff, and students of CREWES (the Consortium for Research in Elastic Wave Exploration Seismology) and the Department of Geoscience at the University of Calgary. First of all, I had the advantage of two supervisors during my Ph.D program, John C. Bancroft and Laurence R. Lines. This dissertation owes much to their wisdom, guidance, and encouragement. In addition I would like to acknowledge Gary Margrave and Michael Lamoureux for their encouragement and suggestions as my supervisory committee members, and Ed Krebes for his help on the seismic theory. My studies have been greatly influenced by Yongwang Ma and Peter Manning. Also suggestions from Kevin Hall, Kayla Bonham, Ben Wards, and Brian Russell, have been incorperated into this dissertation. Joe Wong has pointed out a mistake in one of my CREWES reports. I will always cherish the discussions and friendship with Jeff Chen, Jean Cui, Zimin Zhang, and Peng Cheng. I have unofficially auditted some courses by Don Lawton, Ed Krebes, Larry Lines, Gary Margrave, John C. Bancroft, Rob Stewart and Leslie Reid, with their permission.

I owe thanks to people from my current employer, Key Seismic Solutions. Especially, I am grateful to Bernie Law for training me during the last one and half years. Also, I would like to thank Richard Bale, a former 'CREWESer', for answering my questions at work from time to time, and for being the technical proofreader of the thesis. In addition, Keith Wilkinson and Jeff Deere have given me valuable advices.

Communications with the outside world have been helpful as well. I am grateful to Jean Virieux, Lawrence M. Gochioco, and David Powers for their quick responses to my emails about their publications. Also Ralph Phillip Bording has given me useful suggestions in the meetings arranged by Larry Lines. I also appreciate the people who have communicated with me on my publications, by email or in person.

CREWES and the University of Calgary have provided financial surport for my Ph.D program.

Finally, I would like to thank my wife, Rachel, and my son, Nathan. I have been blessed with a loving and supportive family. In addition to her support and encouragement as my dear wife, Rachel, a librarian, has helped me with literature search when I was starting the studies. Also she was the first proofreader of the dissertation.

Dedication

To my wife Rachel and my son Nathan.

Table of Contents

List of Tables

List of Figures

Symbols, notations, and abbreviations

Notations

- A vector is indicated by boldface type. For example, $\boldsymbol{u}$ denotes a displacement vector, while u_i is a scalar denoting a displacement component in the i^{th} direction.
- Newton's notation for differentiation, also called the dot notation: a dot placed over the function name to represent a time derivative, i.e., if $y = f(t)$, then $\dot{y}$ denotes the first derivative of y with respect to t and $\ddot{y}$ denotes the second derivative of y with respect to t.
- Complex exponential notation of harmonic waves: $\psi = Ae^{i(\kappa x - \omega t)}$ is used to describe an harmonic wave $\psi = A\cos(\kappa x - \omega t)$, where A is the amplitude, κ is the circular wavenumber, ω is the circular frequency, and it is understood that only the real part of the complex exponential is physically valid. That is, although mathematically $\psi = Ae^{i(\kappa x - \omega t)} = A\cos(\kappa x - \omega t) + iA\sin(\kappa x - \omega t)$, only the part of $A\cos(\kappa x - \omega t)$ describes the physical quantity of the wave. With the use of complex exponential notation, the calculations must be linear (Krebes, 2006).

Symbols

Symbol	Definition
c	Rayleigh wave velocity
$\mathcal{D}$	Dilatation
$\boldsymbol{e}$	A unit vector
e_{ij}	Strain tensor
f	Frequency
f_i	Body force density in the i^{th} direction
i, j, k, n	Indices for discretization of Cartesian spatial coordinates and time
κ	Circular wavenumber, or radial wavenumber
R, T	Reflection and transmission coefficient.
t	Time
u_i	Displacement component in the i^{th} direction
v_i	Particle velocity component in the i^{th} direction
v_P, v_S	P-wave and S-wave velocity
x, y, z or x_1, x_2, x_3	Cartesian spatial coordinates
α, β	P-wave and S-wave velocity
δ_{ij}	Kronecker delta. $\delta_{ij} = \begin{cases} 1, & \text{if } i = j, \\ 0, & \text{if } i \neq j. \end{cases}$
λ	Wavelength
λ, μ	Lamé constants
ω	Circular frequency, or radial frequency
σ	Poisson's ratio
σ_{ij}	Stress tensor

Abbreviations

Abbreviation	Definition
1D/2D/3D	One/two/three dimension
AVO	Amplitude versus offset
CDP	Common depth point
CPU	Central processing unit
I/O	Input/output, or read/write, of disk or memory
GB	Gigabyte
Intel® TBB	Intel® Threading Building Blocks
MB	Megabyte
MPI	Message-passing interface
NMO	Normal MoveOut
P waves	Primary waves, also known as dilatational waves, compressional waves, or longitudinal waves
RAM	Random access memory
S waves	Secondary waves, also known as rotational waves, shear waves, or transverse waves
SH waves	Shear-horizontal waves
SV waves	Shear-vertical waves
SI derived units	Derived Units of the International System (SI)
VSP	Vertical seismic profile

Chapter 1

Introduction

The main objectives of this dissertation are to study an elastic wave modelling method and to sketch a reverse-time migration algorithm, which is a prestack depth migration for processing multicomponent seismic records.

This chapter starts with two background concepts, multicomponent and depth migration, and then briefly reviews four aspects: wave modelling, computational boundary conditions in modelling, reverse-time migration, and challenges of computational resources. At the end of this chapter, the agenda of this dissertation is listed.

1.1 Background: multicomponent and depth migration

1.1.1 Single-component and multicomponent

Seismic imaging technologies have advanced to a stage featured by elastic wave and multicomponent seismic data, although single-component seismic reflection surveying is still the working horse of exploration seismology.

Single-component (P-wave, or acoustic) surveying remains the primary seismic method in oil and gas exploration. This is due to at least two reasons. First, single-component reflection seismology simplifies yet highly abstracts the real wave phenomenon. Regarding surface waves as noise, among all the other strongest waves,

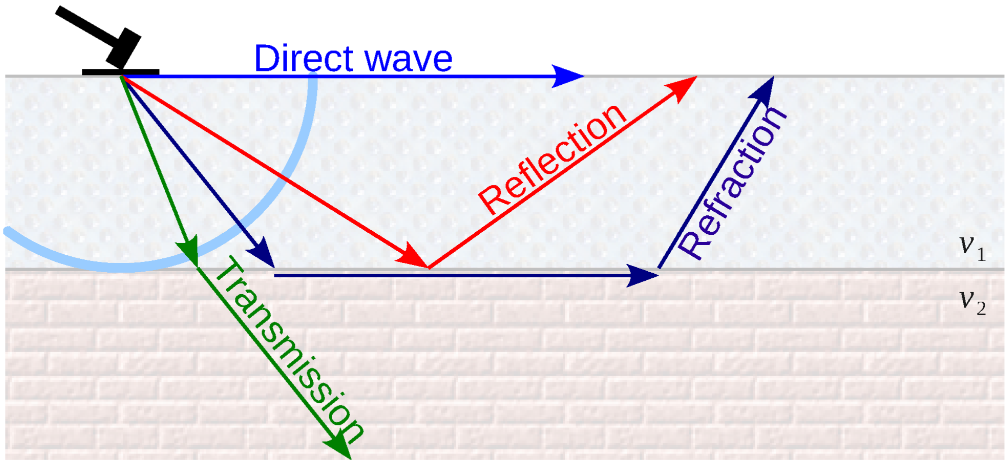

Figure 1.1: Single-component reflection and refraction concepts.

such as direct arrivals, reflected waves, and refracted waves, the P wave is usually the strongest mode with the highest signal-to-noise ratio (Figure 1.1). When the source-receiver offset is not very far and the subsurface reflectors are deep enough, vertical particle motions recorded on the earth surface are mainly caused by P waves. Thus, seismic images derived from the single-component reflection and refraction surveying are very reliable. Second, based on the layered earth model and the concept of Common Depth Point (CDP), which, again, are highly abstracted, academic and commercial organizations have developed very elegant algorithms and software systems to retrieve the subearth structures. Among all the algorithms of statics corrections, velocity analysis, NMO correction, deconvolution, migration, and so on, CDP stacking is a very important step for the reduction of noise (Lines and Newrick, 2004, chap. 5).

Multicomponent surveying started to be widely employed, for good reason. A model of elastic media is a more accurate approximation of the real earth, compared to the acoustic model for single-component surveying. Thus, multicomponent survey-

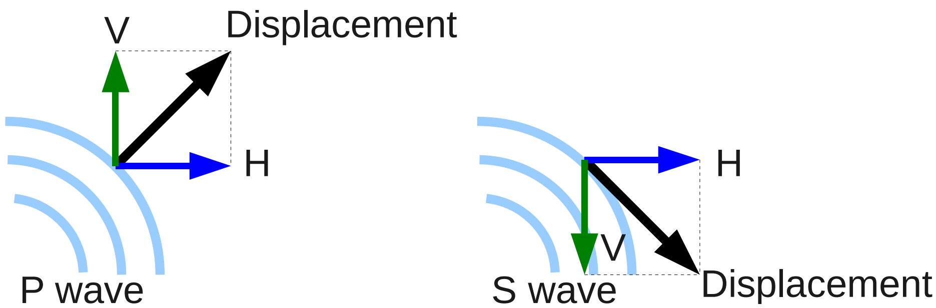

Figure 1.2: Particle displacements in a 2D elastic medium can be decomposited to horizontal(H) and vertical(V) components.

ing, which is based on the elastic model, usually provides more details on subearth structures.

To record waves on surface of elastic media, one needs multicomponent receivers. Particle displacements of waves can be decomposed into X-Y-Z components in 3D. Figure 1.2 illustrates the decomposition of P and S waves in 2D, with 'H' denoting a horizontal component and 'V' denoting a vertical component. Thus, any of the three components (vertical, radial, and transverse) of a surface record always include both P and S waves.

However, the vertical component of surface records is called PP data or PP waves, and the horizontal component is called PS data or PS waves in exploration seismic literature. There are two reasons. The first reason is the way people work with elastic waves. People are focusing on a particular conversion: a downward-propagating P wave, converting on reflection at its deepest point of penetration to an upward-propagating S wave (Stewart et al., 2002). Comparing to S-to-S, S-to-P, or any other transmitted or multiple conversions, the P-to-S conversion is usually the primary one, with higher amplitudes. The second reason is that people make an assumption that ray-paths of reflections are predominantly vertical in the near surface.

In this dissertation, the author uses the names of vertical/horizontal component instead of following the PP/PS tradition. Nevertheless, the term 'PP' is used to denote a P-wave reflection of an incident P wave, and 'PS' an S-wave reflection of an incident P wave, and so on and so forth.

1.1.2 Time migration and depth migration

Migration algorithms are categorized into two fundamental types: time migration and depth migration. "We take the view that, roughly speaking, 'time migration' refers to migration algorithms that pay no attention to ray bending, and 'depth migration' refers to algorithms that do honor ray bending. The distinction between time and depth migration is actually more vague than that, ... In practice there is a sizeable 'gray area' between time and depth migration" (Gray et al., 2001). Reverse-time migration is regarded as a typical depth migration algorithm, although there is the word 'time' in the name.

There are advantages of time migration over depth migration. First of all, time migration generally requires much less computational resources, in terms of computing CPU time and computer memory requirement. In fact, this is the main reason that historically the development of time migration proceeded in advance of depth migration. Second, time migration is more robust to subsurface model errors, while depth migration is very sensitive to those errors. Third, seismic processors and interpreters often need to work in time coordinates, because surface seismic data, most of the available processing (filtering, migration, etc.) and interpretation techniques and tools, are in time and frequency.

Time migration mispositions subearth events in the presence of lateral velocity

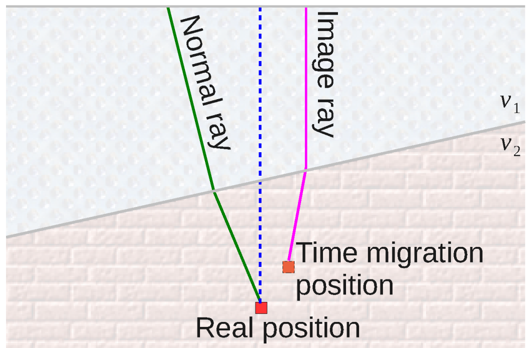

Figure 1.3: Time migration mispositions a point diffractor below a dipping layer interface (adopted from Black and Brzostowski (1994)). A similar subearth model shown in Figure 4.20 is used in reverse-time migration, and the migrated section is shown in Figure 4.22.

variation (Black and Brzostowski, 1994; Bevc and Palacharla, 1995; Gray et al., 2001). Even if the correct velocity is used, time migration mispositions events whenever the velocity changes laterally (Figure 1.3). These errors increase with lateral velocity variation, depth of burial, and dip angle. Black and Brzostowski (1994) listed formulae for error calculation.

Depth migration is more ambitious than time migration, but it has not always lived up to expectations. Nevertheless, depth migration is a more powerful interpretive processing tool, and its results can give us greater confidence in both the geologic structure and the velocity field than the results of time migration can (Gray et al., 2001). Also, we ultimately drill to geologic targets that are in depth, so at some point, there must be a conversion of seismic reflections in time to the depth domain. Depth migration can provide the best method for such conversion.

1.2 Elastic wave modelling

Seismic modelling plays an important role in data acquisition, processing, and interpretation. Lines and Newrick (2004, chap. 15) summarized six uses of seismic modelling: design of seismic experiments, prediction of results, enhanced interpretation, inversion, testing processing algorithms, and examining effects of noise.

Lines and Newrick (2004, chap. 15) also listed most typical modelling methods, including normal-incidence reflectivity, amplitude variation with offset, ray tracing, wave-equation finite-difference (FD) or finite-element (FE) solutions, and physical modelling. Among them, wave-equation methods are regarded as a more expensive category, but they can offer more general and complete seismic models than other methods.

Finite-difference methods are practiced on numerical grid of nodal points both in space and time. Depending on the choice of the nodal points, the grid scheme can be classified in two broad categories: staggered and non-staggered. Seismologists use both schemes to simulate elastic wave phenomena.

Two classic papers about non-staggered grid schemes are by Alterman and Karal (1968) and by Kelly, Ward, Treitel, and Alford (1976). Alterman and Karal (1968) proposed a very successful seismic source modelling method. Kelly et al. (1976) generalized non-staggered grid schemes for heterogeneous media, further developed the seismic source modelling method by Alterman and Karal (1968), and proposed free-surface boundary conditions. The free-surface boundary conditions are widely referred to as 'the vacuum method'.

Two classic papers about staggered-grid schemes are authored by Virieux (1984, 1986). The first one (Virieux, 1984) talks about SH wave modelling, and the second one P-SV wave case. Both methods use particle velocities and stresses, with the physical nodes on staggered grids. The models used are in 2D. Finite-difference approximations are in the second order. The algorithms are in the time domain.

Staggered-grid schemes have been further developed ever since Virieux's two papers. Levander (1988) proposed a forth-order method. Ohminato and Chouet (1997) extended the method to 3D. Manning (2008) proposed techniques to enhance the accuracy and efficiency of modelling in the frequency domain, using only particle displacement in his modelling. The most recent development based on the staggered-grid is on anisotropic fractured coalbed modelling (Pei, Fu, Sun, Jiang, and Zhou, 2012).

There are advantages of staggered-grid schemes over non-staggered grid ones. It has been shown that staggered-grid schemes deal with liquid-solid interface without the need for special treatment, which is not the case for non-staggered grid schemes (Virieux, 1986; Levander, 1988; Stephen, 1988). Besides, the implementation of seismic energy sources is much easier in staggered-grid schemes.

1.3 Computational boundary

A computational boundary problem arises from the limitation of available computational resources. This problem has been a persistent topic in the field of wave phenomena modelling. Migration algorithms also have to deal with these boundaries.

1.3.1 The problem

Computational boundaries are different from the physical boundaries in media. In the real world, physical boundaries are rock-rock, rock-water, water-air, rock-air interfaces. In seismic modelling, in addition to those physical boundaries, there exist

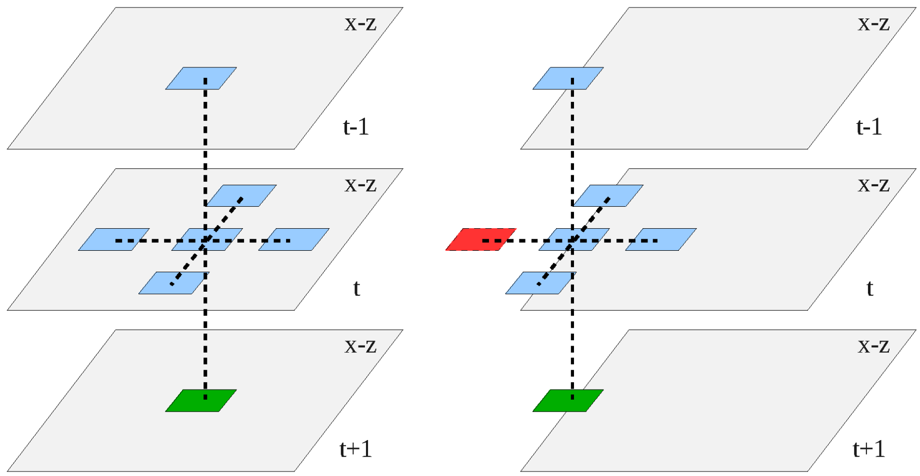

(a) A finite difference approximation for 2D acoustic wave equation

(b) Problem: an unavailable value at a computational boundary

Figure 1.4: The computational boundary problem of a 2D finite-difference grid. Figure 3.7 illustrates one of the solutions.

computational boundaries. For example, for a 2D subsurface model of the shape of a rectangle, the physical boundaries are a free surface on the top and rock boundaries inside the subsurface, and the computational boundaries are a bottom boundary and two sides on the left and right.

The computational boundary problem arises as follows. Finite-difference methods estimate a wavefield value of a given subsurface node at a given time from the wave field values of the same node and surrounded nodes at the previous times. Figure 1.4a sketches a finite difference approximation for the acoustic wave equation. When a node is surrounded by other nodes in all four directions, the approximation can be done. However, if a node is at the subsurface computational boundary and one of its surrounding nodes is missing, how should one do the finite-difference calculation? Figure 1.4b shows the problem.

If the wavefield values on the computational boundaries are set to zero, the resulting boundaries act like physical rigid boundaries. All the incident seismic energy strikes upon a rigid boundary will be reflected back.

1.3.2 Known solutions

There are a lot of solutions to the boundary condition problems. The most cited method for boundary conditions is the 'absorbing boundary conditions' proposed by Clayton and Engquist (1977). Another popular method, called the 'nonreflecting boundary condition', was presented by Cerjan, Kosloff, Kosloff, and Reshef (1985). There are some other solutions as well, such as 'transparent boundary' by Long and Liow (1990) and 'Perfectly Matched Layer' method by Collino and Tsogka (2001).

1.4 Reverse-time migration

Recent advances in technologies have made reverse-time migration commercially available, although the method was considered impractical due to its high requirements on computational resources and its sensitivity to velocity models. For example, ION's subsidiary, GX Technology (GXT), states that it commercially introduced reverse-time migration in 2005, and has used it effectively on 26 projects spread throughout the world. "Significant improvement can be achieved both in the model building and final migration by employing the two-way reverse time migration technique. It is the combination of model building and migration that is the key to successful imaging" (Ion, 2012).

Reverse-time migration is far more faithful in representing the full wave propagation phenomena than most of the other migration methods, such as Kirchhoff migration, and one-way wavefield extrapolation migration (Leveille1 et al., 2011).

Due to high prices and increased difficulties in finding shallow deposits, exploration and exploitation of hydrocarbon resources are expected to be moving to greater depths and to deal with more complicated subearth structures. Consequently, reverse-time migration will become a more important tool.

Reverse time migration was first derived for acoustic poststack migration based on the exploding reflector model by McMechan (1983) and Whitmore (1983). Since then it has advanced to elastic prestack forms (Chang and McMechan, 1986; Sun and McMechan, 1986; Chang and McMechan, 1987; Sun and McMechan, 1988). Bording and Lines (1997) presented an excellent tutorial on modelling and reverse-time migration.

The imaging principle and imaging conditions are the heart of reverse-time migration algorithms, and there is extensive literature about it. Claerbout (1971) stated the imaging principle, “Reflectors exist at points in the ground where the first arrival of downgoing wave is time coincide with an upgoing wave”, and proposed two methods for imaging conditions, with one using a ratio of upgoing over downgoing wavefield amplitudes, and the other using cross-correlation between downgoing and upgoing wavefields, formulated in both frequency and time domains. Whitmore and Lines (1986) proposed source normalized cross-correlation method. Chang and McMechan (1987) used ray tracing. Loewenthal and Hu (1991) proposed two methods: one is by maximum amplitude criteria, and the other is by minimum time criteria. Biondi and Shan (2002) practiced the cross-correlation method. Kaelin and Guitton (2006) proposed to normalize the cross-correlation by upgoing wavefields. Chattopadhyay and McMechan (2008) summarized several methods: excitation-time imaging conditions, which is similar to methods of Loewenthal and Hu (1991), cross-correlation imaging conditions, and ratio of upgoing over downgoing wavefield amplitudes. The most recent technologies on imaging conditions are developed for elastic reverse-time migration. For example, Yan and Sava (2007) presented elastic imaging conditions based on wavefield decomposition, and Du, Zhu, and Ba (2012) applied source normalized cross-correlation method with polarity reversal correction for elastic reverse-time migration.

People apply finite-difference methods for elastic wave modelling on both non-staggered and staggered grid. However, only non-staggered grid schemes are widely employed in elastic reverse-time migration, while staggered-grid schemes are rarely employed in reverse-time migration algorithms. When I was starting my elastic reverse-time migration studies in 2009, the only document that I had found using a staggered-grid scheme is by Wang (2000). However, that algorithm needs both particle velocity and pressure data to be recorded.

1.5 Computational resources

High demand of computational resources, such as CPU time, memory, disk space, network speed, and so on, is a drawback for finite-difference methods. Among the challenges, CPU time is the number one. For example, Martin (2004) used 8 CPU years to do modelling with Marmousi2 model.

The solution to the high demand of computational CPU time is parallel computing. According to the hardware used, parallel computing can be roughly classified to two types: multi-core and multi-processor (hereafter referred to as multi-core) parallel computing using a single computer, and distributed parallel computing using multiple computers, such as cluster computers.

In the exploration seismology literature, Gavrilov, Lines, Bland, and Kocurko (2000) have already practiced parallel computing to accelerate reverse-time migration. They used the message-passing interface (MPI) to develop the distributed parallel implementation and carried out the computing on a cluster computer.

Multi-core computing is a relatively new and rapidly developing technique. It has become popular since 2005. During 2005, Intel® developed its first dual-core processor. In the following year it released Intel® Threading Building Blocks (TBB), a C++ template library, for writing software programs that take advantage of multi-core processors. Computer hardware and software have been rapidly developed ever since. Nowadays, computers with 16-core CPU's are very common, and Intel® TBB has upgraded to version 4.0.

1.6 Dissertation outline

The main content of the dissertation is organized into four chapters: wave modelling, computational boundary conditions, reverse-time migration, and computational resources.

The next chapter, Chapter 2, is about elastic wave modelling by a staggered-grid finite-difference scheme. Starting from equations about seismic waves, the chapter details 1D P wave, 2D SH wave, 2D P-SV wave, and 3D wave modelling. Wave modelling ingredients, including finite-difference scheme, free-surface boundary, seismic energy source, subsurface model building, and so on, are integrated together to form an elastic wave modelling system. In order to validate the correctness of the modelling algorithms and coded programs and to find the pitfalls coming with them, numerical modelling results are compared to mathematical analysis. And doing so, for myself, leads to better understandings of wave phenomena and seismic concepts, including seismic energy sources, guided waves, head waves of different situations, Rayleigh waves, and so on.

Chapter 3 addresses computational boundary conditions. First, rigid boundaries are mathematically analyzed and numerically modelled. Then, absorbing boundary conditions (Clayton and Engquist, 1977) and a nonreflecting boundary condition (Cerjan et al., 1985) are examined. At last, a combined boundary condition is proposed and results are compared to those of absorbing and nonreflecting boundary conditions.

A prestack reverse-time migration workflow is sketched in Chapter 4. Some well-known methods of imaging conditions in the literature are examined using a point reflector subsurface model. Then, a new imaging condition for multicomponent data processing, called energy normalized imaging condition, is described, and the results are compared to other imaging conditions. The sketched workflow is very different from traditional seismic data processing. For example, removal of ground roll in surface records is not needed at all. Migration results of a shrunk Marmousi2 model are created and interpreted, to demonstrate the characteristics of the proposed imaging condition. Finally, in order to further demonstrate the correctness of reverse-time migration, a migrated section from a dipping-layer model is presented.

Discussions on challenges of computational resources are included in Chapter 5. The problems of computational time and disk space requirement are described, and solutions to those problems are proposed.

Chapter 2

Elastic wave modelling

After the theory on seismic waves and seismic source wavelets, this chapter details modelling of 1D P wave, 2D SH wave, 2D P-SV wave, and 3D wave.

The discussion is not only about the modelling method itself, but also about understanding wave phenomena and seismic theories by modelling. A modelling algorithm integrates a finite-difference implementation, a seismic energy source scheme, a free-surface boundary condition, computational boundary conditions, and subsurface models. Comparing modelling results to theoretical analysis leads to not only better understandings of the modelling method itself, but also better understandings of wave phenomena and theory, such as free-surface effect, guided waves, Rayleigh waves, tuning effect, geometrical spreading, different kind of head waves, seismic diffractions, and amplitude variation with offset (AVO).

2.1 Equations about seismic waves

Equations describing waves in elastic media include three relations: displacement-stress relations, stress-strain relations, and displacement-strain relations. In addition, the relations between traction and stress are important in describing free surfaces.

2.1.1 Equation of motion: displacement-stress relations

By applying Newton's second law of motion to a volume, the equation of motion can be derived as,

$$\sum_{j=1}^{3} \frac{\partial \sigma_{ij}}{\partial x_j} + f_i = \rho \frac{\partial^2 u_i}{\partial t^2}, \quad i = 1, 2, 3, \tag{2.1}$$

where i and j are directions, σ_{ij} is a stress tensor, f_i is a force density, ρ is density, and u_i is a displacement component. Assuming body forces (e.g., gravity) are negligible, the equation of motion becomes,

$$\sum_{j=1}^{3} \frac{\partial \sigma_{ij}}{\partial x_j} = \rho \frac{\partial^2 u_i}{\partial t^2}, \quad i = 1, 2, 3. \tag{2.2}$$

Thus, equation of motion indicates the relationship between particle displacements and stresses.

In this dissertation, x_1, and x_2 are horizontal directions, and x_3 is the vertical direction. Sometimes, x, y, and z are used instead.

2.1.2 Stress-strain relations

Hooke's law tells us that the force acting on a spring is a linear function of the spring's displacement. Similarly, stresses acting on an elastic medium are linearly related to strains. Thus, the stress-strain relations for an isotropic medium are

$$\sigma_{ij} = \sum_{k=1}^{3} \sum_{l=1}^{3} c_{ijkl} e_{kl}, \quad i, j = 1, 2, 3, \tag{2.3}$$

where σ_{ij} is a stress tensor, c_{ijkl} is an elastic constant, and e_{kl} is a strain tensor.

For an isotropic medium, whose physical properties are the same in all directions, an elastic constant can be denoted by Lamé constants as

$$c_{ijkl} = \lambda\delta_{ij}\delta_{kl} + \mu(\delta_{ik}\delta_{jl} + \delta_{il}\delta_{jk}) \tag{2.4}$$

where λ and μ are Lamé constants, and δ_{ij} is Kronecker delta, which is defined by

$$\delta_{ij} = \begin{cases} 1, & \text{if } i = j; \\ 0, & \text{if } i \neq j. \end{cases} \tag{2.5}$$

Thus, the stress-strain relations for an elastic medium can be derived as,

$$\sigma_{ij} = \lambda\mathcal{D}\delta_{ij} + 2\mu e_{ij}, \quad i, j = 1, 2, 3, \tag{2.6}$$

where $\mathcal{D} = \sum_k e_{kk} = \nabla \cdot \boldsymbol{u}$ is the dilatation.

2.1.3 Displacement-strain relations

Displacement-strain relations, mathematically shown below, are gained from the definition of strain.

$$e_{ij} = \frac{1}{2}(\frac{\partial u_i}{\partial x_j} + \frac{\partial u_j}{\partial x_i}), \quad i, j = 1, 2, 3 \tag{2.7}$$

2.1.4 Displacement-stress-strain relations

Combining the equation of motion, the stress-strain relations for an isotropic medium, and the displacement-strain relations, one obtains a system as follows:

$$\rho\frac{\partial^2 u_i}{\partial t^2} = \sum_{j=1}^{3} \frac{\partial \sigma_{ij}}{\partial x_j}, \quad i = 1, 2, 3, \tag{2.8a}$$

$$\sigma_{ij} = \lambda \mathcal{D} \delta_{ij} + 2\mu e_{ij}, \quad i,j = 1,2,3, \tag{2.8b}$$

$$e_{ij} = \frac{1}{2}(\frac{\partial u_i}{\partial x_j} + \frac{\partial u_j}{\partial x_i}), \quad i,j = 1,2,3. \tag{2.8c}$$

The above equation system is referred to as 3D displacement-stress-strain relations for an isotropic elastic medium in this dissertation. All the modelling cases described in the dissertation, including 1D P waves, 2D SH waves, 2D P-SV waves, and 3D waves, are derived or simplified from the displacement-stress-strain relations.

2.1.5 Traction, stress tensor, and free-surface boundary condition

Following the convention of the course notes by Krebes (2006), one can denote the relations between traction and stress tensor as

$$\sigma_{ij} = T_i(\boldsymbol{e}_j) \tag{2.9}$$

where T_i denotes a traction component, $\boldsymbol{e}$ denotes a unit vector normal to a surface, the index i denotes the direction of the traction component, and the index j denotes the direction normal to the surface on which the traction is applied.

Suppose one uses the top of a 3D cubic volume to model the free earth surface, the traction component normal to this horizontal planar top is zero. That is

$$T_3 \Big|_{x_3=0} \equiv 0. \tag{2.10}$$

Thus for 3D wave propagation, the free-surface boundary conditions at a horizontal planar surface are

$$\sigma_{3j}\Big|_{x_3=0} = T_3(\boldsymbol{e}_j)\Big|_{x_3=0} = 0, \quad j = 1, 2, 3. \tag{2.11}$$

Later in the dissertation, for modelling cases other than 3D, i.e., for 1D P waves, 2D SH waves, and 2D P-SV waves, the above conditions are simplified and used.

The stress tensor is symmetric:

$$\sigma_{ij} = \sigma_{ji} \quad i, j = 1, 2, 3. \tag{2.12}$$

This property is used in the dissertation later without being referred to.

2.2 Seismic wavelets

There are many choices of wavelets in the literature. Ryan (1994) discussed four common ones, Ricker, Ormsby, Klauder, and Butterworth wavelets. Alterman and Karal (1968) proposed a time source. Manning (2008) discussed a time differentiated Ricker wavelet. The characteristics and shapes of these wavelets are different from each other.

Among the various wavelets mentioned above, Ricker, Ormsby, and time differentiated Ricker wavelets have the benefit that it is easy to control their frequency range. Their characteristics are analyzed below. Eventually, Ricker and time differentiated Ricker wavelets are used in this dissertation.

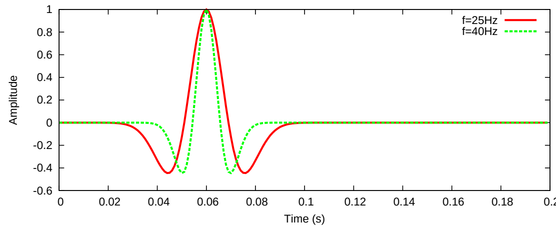

(a) Two Ricker wavelets

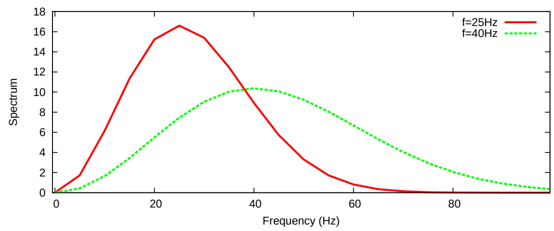

(b) Spectra of Ricker wavelets

Figure 2.1: Two Ricker wavelets and their spectra. The peak frequencies are 25Hz and 40Hz.

2.2.1 Ricker wavelets

Ricker wavelets are employed throughout the dissertation. A Ricker wavelet $r(f_p, t)$ with a given peak frequency f_p is denoted as

$$r(f_p, t) = (1 - 2\pi^2 f_p^2 t^2)e^{-\pi^2 f_p^2 t^2}, \tag{2.13}$$

where t denotes time.

Figure 2.1 shows two Ricker wavelets and their amplitude spectra. Note that there is a time shift of 0.6s applied for the Ricker wavelets.

The characteristics of a Ricker wavelet are uniquely decided by the peak frequency f_p. As shown in Figure 2.1a, the breadth of a wavelet in time domain is inversely proportional to the peak frequency; on the other hand, as shown in Figure 2.1b, the spectrum amplitude at the peak frequency is the highest.

2.2.2 Ormsby wavelets

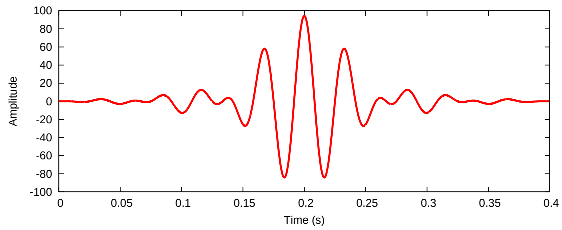

(a) An Ormsby wavelet

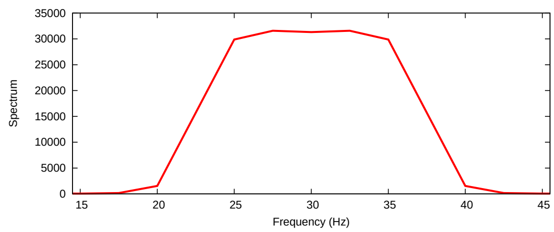

(b) Spectrum of the wavelet

Figure 2.2: An Ormsby wavelet and its spectrum. The characteristic frequencies are 20Hz, 25Hz, 35Hz, and 40Hz.

Ormsby wavelets was used in Marmousi2 modelling by Martin (2004). An Ormsby wavelet $o(f_1, f_2, f_3, f_4, t)$ with a given frequency range f_p is denoted as

$$\begin{aligned} o(f_1, f_2, f_3, f_4, t) = \pi f_4^2 sinc^2(\pi f_4 t)/(f_4 - f_3) \\ - \pi f_3^2 sinc^2(\pi f_3 t)/(f_4 - f_3) \\ - \pi f_2^2 sinc^2(\pi f_2 t)/(f_2 - f_1) \\ - \pi f_1^2 sinc^2(\pi f_1 t)/(f_2 - f_1), \end{aligned} \tag{2.14}$$

where f_1, f_2, f_3, and f_4 are, respectively, low-cut, low-pass, high-pass, and high-cut frequencies of the Ormsby wavelet. The characteristics of an Ormsby wavelet are decided by those four frequencies.

Figure 2.2 shows an Ormsby wavelet, with characteristic frequencies 20Hz, 25Hz, 35Hz, and 40Hz, and its spectrum feature. Note that there is a time shift applied to the wavelet.

As observed, a Ricker wavelet has only two side lobes, while an Ormsby wavelet has many side lobes. Both wavelets are symmetric.

2.2.3 Time differentiated Ricker wavelets

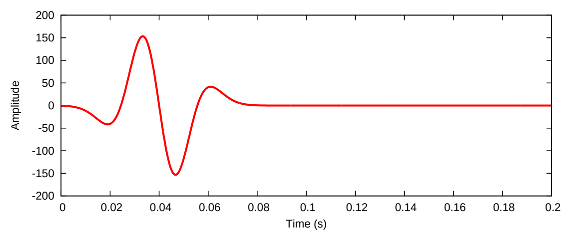

(a) Time-differentiated Ricker wavelet

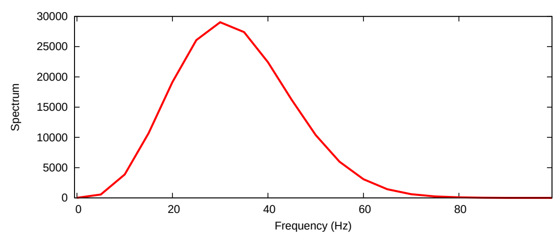

(b) Spectrum of the wavelet

Figure 2.3: A wavelet obtained by taking time derivative of a Ricker wavelet. The peak frequency of the original Ricker wavelet is 25Hz.

Both the Ricker wavelet and the Ormsby wavelet discussed are symmetric. Occasionally, one may need wavelets that are not symmetric. For example, in order to observe the phase change of a wave reflected upon a free surface or a rigid boundary, it is inconvenient if the incident wave has a symmetric waveform.

There are many forms of asymmetrical wavelets available, such as Butterworth wavelets, time derivative of a Gaussian function, and a wavelet presented by Alterman and Karal (1968). However, a wavelet obtained by taking time derivative of a Ricker wavelet is selected as the asymmetrical wavelet used in this dissertation. The wavelet is referred to as a time differentiated Ricker wavelet. The main reason that this wavelet is chosen is that when double Ricker seismic source is applied, some times the resulting wavelet is in the shape of the time derivative of a Ricker wave (Manning, 2008).

A time differentiated Ricker wavelet $\dot{r}$ can be obtained by taking derivative with respect to time of the Ricker function (2.13).

$$\dot{r}(t) = 2\pi^2 f_p^2 t(2\pi^2 f_p^2 t^2 - 3)e^{-\pi^2 f_p^2 t^2}. \tag{2.15}$$

However, a convenient alternative is using central difference approximation to calculate the discrete series of a time differentiated Ricker wavelet from a Ricker wavelet with a given peak frequency as

$$\dot{r}(t_n) = \frac{r(t_{n+1}) - r(t_{n-1})}{2\Delta t}, \tag{2.16}$$

where Δt is the numerical time step.

Figure 2.3 shows a time differentiated Ricker wavelet, with the original Ricker wavelet peak frequency 25Hz, and its amplitude spectrum. A Ricker wavelet with a peak frequency of 25HZ and its amplitude spectrum are shown in Figure 2.1. It is observed that the peak frequency of the time differentiated Ricker wavelet is around 30Hz, which is higher than the original Ricker wavelet.

Mathematically the peak frequency change is reasonable. Denoting spectrum of $r(t)$ as $\bar{r}(\omega)$, the spectrum of $\dot{r}(t)$ is $-i\omega\bar{r}(\omega)$, where $-i$ is a $90°$ phase shift operator not changing the amplitude spectrum, and the factor ω leads to richer higher frequency spectrum and poorer lower frequency spectrum of $\dot{r}(t)$ than those of $r(t)$. For more details, please see Chapter 6 of Krebes (2006).

2.3 1D P wave modelling

Following the description of the modelling algorithm, some modelling examples are presented to analyze the algorithm.

2.3.1 Algorithm

Usually a wave modelling algorithm based on a staggered-grid scheme involves the following items.

- A simplified elastodynamic equation system. This is derived from equations about seismic waves (Equation 2.8).
- A velocity-stress system. This is derived from the elastodynamic equation system.
- A finite-difference implementation.
- A free-surface boundary scheme.
- Computational boundary conditions.
- A seismic source scheme.

- Subsurface models.

Elastodynamic equations

Consider a plane P wave travelling in the vertical direction x_3, with particle vibrations in the direction of wave propagation. In this case, there is no horizontal particle vibrations, and only the normal stresses and normal strains parallel to the vertical direction exist, i.e.,

$$u_i \equiv 0, \quad i \neq 3, \tag{2.17a}$$

$$\sigma_{ij} \equiv 0, \quad i,j \neq 3, \tag{2.17b}$$

$$e_{ij} \equiv 0, \quad i,j \neq 3. \tag{2.17c}$$

Substituting the above equations into the 3D displacement-stress-strain relations (2.8), one can get 1D P-wave elastodynamic equations

$$\rho \frac{\partial^2 u_3}{\partial t^2} = \frac{\partial \sigma_{33}}{\partial x_3}, \tag{2.18a}$$

$$\sigma_{33} = (\lambda + 2\mu) \frac{\partial u_3}{\partial x_3}, \tag{2.18b}$$

Velocity-stress system

Denoting particle vibration velocity as v, the relationship between particle velocity and particle displacement can be denoted as

$$\frac{\partial u_3}{\partial t} = v_3. \tag{2.19}$$

Substitution of Equation (2.19) into Equation (2.18a) yields

$$\rho \frac{\partial v_3}{\partial t} = \frac{\partial \sigma_{33}}{\partial x_3} \tag{2.20}$$

Taking partial derivative with respect to time in equation (2.18b), and substituting equation (2.19) into the resulting equation, one obtains

$$\frac{\partial \sigma_{33}}{\partial t} = (\lambda + 2\mu) \frac{\partial v_3}{\partial x_3}. \tag{2.21}$$

Combining the above two equations, (2.20) and (2.21), one obtains 1D velocity-stress system for an isotropic medium as

$$\rho \frac{\partial v_3}{\partial t} = \frac{\partial \sigma_{33}}{\partial x_3}, \tag{2.22a}$$

$$\frac{\partial \sigma_{33}}{\partial t} = (\lambda + 2\mu) \frac{\partial v_3}{\partial x_3}. \tag{2.22b}$$

Note that the word "velocity" in the term "velocity-stress system" stands for the particle vibration velocity, which is different from a wave propagation velocity.

Although the more commonly referred wave equations are not used in this dissertation, it is interesting to find the connections between wave equations and the velocity-stress wave systems. For example, if one substitutes equation (2.18b) into equation (2.18a), one gets

$$\rho \frac{\partial^2 u_3}{\partial t^2} = \frac{\partial ((\lambda + 2\mu) \frac{\partial u_3}{\partial x_3})}{\partial x_3}. \tag{2.23}$$

For a homogeneous medium, where physical properties do not vary with position, the above equation is simplified to

$$\rho \frac{\partial^2 u_3}{\partial t^2} = (\lambda + 2\mu) \frac{\partial^2 u_3}{\partial x_3^2}. \tag{2.24}$$

which is the 1D wave equation for a P wave travelling in a homogeneous medium. Thus, wave equations and velocity-stress wave systems are connected.

Finite-difference implementation

If a grid step h is used for x_3 axis and Δt is used for the time step, similar to the 2D staggered-grid schemes by Virieux (1984, 1986), 1D velocity-stress system (2.22) of a P wave can be approximated as

$$v_{3_k}^{n+1/2} = v_{3_k}^{n-1/2} + \frac{\Delta t}{h\rho_k}(\sigma_{33_{k+1/2}}^{n} - \sigma_{33_{k-1/2}}^{n}), \tag{2.25a}$$

$$\sigma_{33_{k+1/2}}^{n+1} = \sigma_{33_{k+1/2}}^{n} + \frac{(\lambda + 2\mu)_{k+1/2}\Delta t}{h}(v_{3_{k+1}}^{n+1/2} - v_{3_k}^{n+1/2}), \tag{2.25b}$$

where k is the index for x_3 discretization, and n is the index for time discretization.

According to Virieux (1986), the stability consition for an n-D space, is

$$v_p \frac{\Delta t}{h} < \frac{1}{\sqrt{n}} \tag{2.26}$$

The staggered grid is shown in Figure 2.4.

Two implementations of a free-surface boundary

The surface is stress-free, i.e.,

$$\sigma_{33}\Big|_{x_3=0} \equiv 0. \tag{2.27}$$

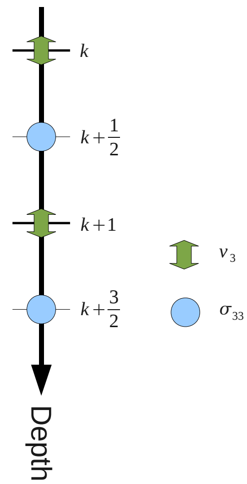

Figure 2.4: A staggered grid for 1D wave modelling.

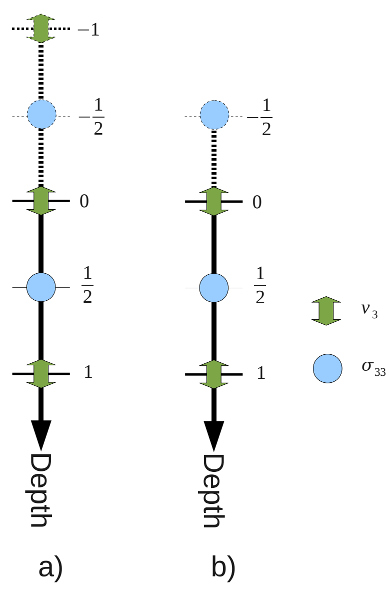

Figure 2.5: Two implementations of a free-surface boundary for 1D wave modelling. a) is based on particle velocity, and b) is based on stress.

This is a simplified case of Equation 2.11.

There are two ways to implement the free-surface boundary condition for the grid shown in Figure 2.4. Schemes of both implementations are shown in Figure 2.5.

One way is to implement the boundary condition on particle velocities.

Substitution of

$$\sigma_{33} = (\lambda + 2\mu)e_{33} = (\lambda + 2\mu)\frac{\partial u_3}{\partial x_3}, \tag{2.28}$$

into Equation 2.27 yields

$$\left.\frac{\partial u_3}{\partial x_3}\right|_{x_3=0} = 0. \tag{2.29}$$

Taking derivative with respect to time, with $v_3 = \frac{\partial u_3}{\partial t}$ one gets

$$\left.\frac{\partial v_3}{\partial x_3}\right|_{x_3=0} = 0. \tag{2.30}$$

Suppose that above the surface, there is a fictitious cell with the same elastic properties as the cell on the surface, where the particle velocity node has a sequence number of -1, and the stress node has a sequence number of $-\frac{1}{2}$. Since on the surface the stress is zero, it is possible to use central difference to approximate the above equation and obtain the following discretized form of the free-surface boundary condition

$$v_{3}{}_{-1}^{n+1/2} = v_{3}{}_{1}^{n+1/2}, \tag{2.31}$$

where $v_{3}{}_{-1}^{n+1/2}$ is the particle velocity of the fictitious cell above the surface at discretized time $n + 1/2$. Thus, on the surface

$$v_{3}{}_{0}^{n+1/2} = v_{3}{}_{0}^{n-1/2} + \frac{\Delta t}{h\rho_0}(\sigma_{33}{}_{1/2}^{n} - \sigma_{33}{}_{-1/2}^{n}), \tag{2.32a}$$

$$\sigma_{33}{}^{n+1}_{-1/2} = \sigma_{33}{}^{n}_{-1/2} + \frac{(\lambda + 2\mu)_{1/2}\Delta t}{h}(v_{30}{}^{n+1/2} - v_{31}{}^{n+1/2}), \tag{2.32b}$$

where $\sigma_{33}{}^{n+1}_{-1/2}$ is the stress of the fictitious cell above the surface at discretized time $n + 1$.

The second way of implementing free-surface boundary condition is based on stresses.

Using central difference to approximate the free-surface boundary condition (2.27), one obtains the following discretized from

$$\sigma_{33}\Big|_{x_3=0}^{t(n)} = \frac{\sigma_{33}{}^{n}_{-1/2} + \sigma_{33}{}^{n}_{1/2}}{2} = 0. \tag{2.33}$$

Thus,

$$\sigma_{33}{}^{n}_{-1/2} = -\sigma_{33}{}^{n}_{1/2}. \tag{2.34}$$

The method of stress is much easier than that of particle velocity. However, the method of particle velocity is useful in finite-difference methods that only deal with particle velocities or displacements. For example, the method of particle velocity (displacement) is used in the dissertation by Manning (2008).

Computational boundary

An absorbing boundary condition proposed by Clayton and Engquist (1977) is applied to 1D wave modelling. The details of computational boundary conditions are addressed in Chapter 3.

2.3.2 Modelling examples

The finite-difference modeling method simulates seismic-wave propagation by approximating elastodynamic equation system. There is no explicit implementation on media interfaces except for free surfaces. Can the finite-difference method accurately simulate the reflection and transmitted waves upon media interfaces? Do the modelled waves travel at the wave velocities specified in the subsurface model? Do the modeling results match with analytical results? How accurate do they match? To answer these questions, two modeling results are presented here, and they are compared to corresponding analytical results.

2.3.2.1 A homogeneous medium with a buried plane wave source

The subsurface medium used in this example is homogeneous. The top of the model is the ground surface, and the bottom is at the depth of $1km$. The P-wave velocity inside the medium is $3000km/s$, and the density of the medium is $2290.89kg/m^3$. The time step is $0.00025s$, and the space grid step is $1m$.

In this modeling experiment, a plane wave source of a time-differentiated-Ricker wavelet is placed at the depth of $300m$, and two plane waves are generated from the seismic source. One travels down towards the bottom of the model, and it seems to go through the bottom boundary and disappear. The other one travels up towards the surface of the model, and it strikes the surface on the top of the model. There are no transmitted waves generated. All the wave energy is reflected back into the subsurface. Then the wave travels down and disappears at the bottom of the model.

With this model, we can check the following aspects of the modelling method: modelled wave velocity, reflection coefficient upon free surface, and absorbing boundary on the bottom.

Table 2.1: Travel times, distances, and amplitudes of modelled 1D waves in a homogeneous medium.

Figure	Time (s)	Depth (m)	Distance (m)	Amplitude
2.6c	0.0625	424	0	163.34
2.6d	0.0875	599	75	163.20
2.6e	0.1125	574	150	163.00
2.6f	0.1375	649	225	162.85
2.6g	0.1625	724	300	162.73
2.6h	0.1875	799	375	162.58
2.6i	0.2125	874	450	162.40
2.6j	0.2375	949	525	162.25

Modelled wave velocity

By checking wave peaks at different modelling times, shown in Table 2.1, it can be observed that modelled waves travel at the specified velocity: 3000m/s.

Modelled free-surface reflectivity

Let $u^{(I)}$ and $u^{(R)}$ denote, respectively, the incident and reflected wave displacement at an interface of two media, where the densities of the first and the second media are, respectively, ρ_1 and ρ_2, and the wave velocities of the first and the second media are, respectively, α_1 and α_2. From the stress-strain relations one can derive that

$$u^{(R)} = -Ru^{(I)}, \tag{2.35}$$

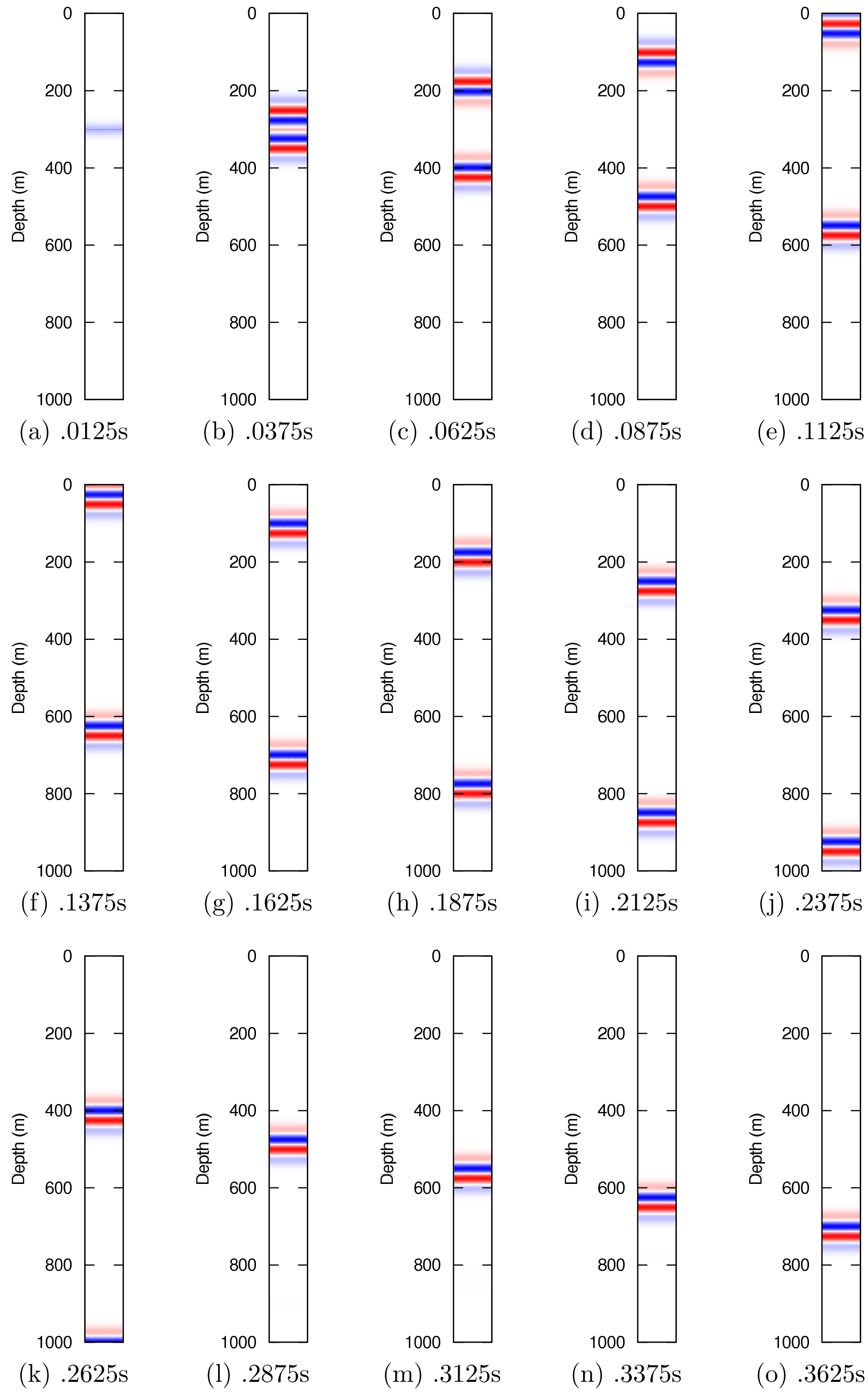

(a) .0125s (b) .0375s (c) .0625s (d) .0875s (e) .1125s

(f) .1375s (g) .1625s (h) .1875s (i) .2125s (j) .2375s

(k) .2625s (l) .2875s (m) .3125s (n) .3375s (o) .3625s

Figure 2.6: Waves in a 1D homogeneous medium with a buried source.

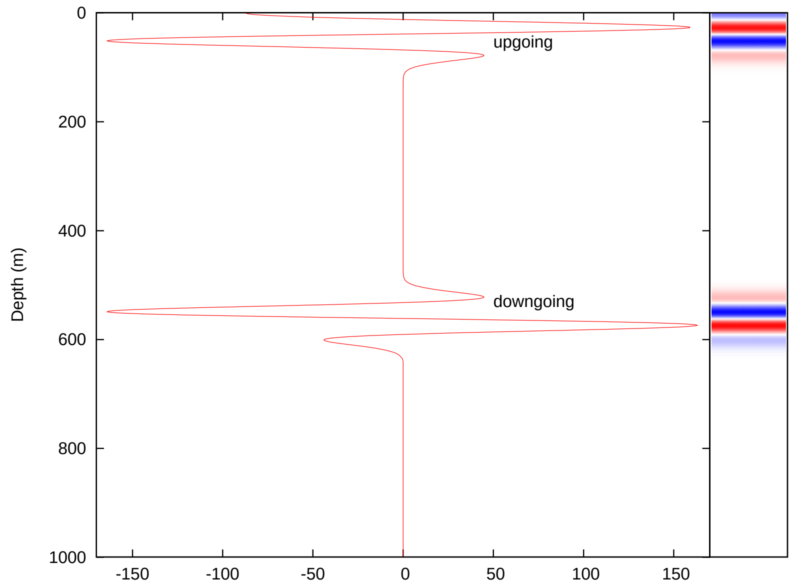

(a) An upgoing wave striking a surface from the bottom of the surface - enlarged Figure 2.6e and its wiggle plot

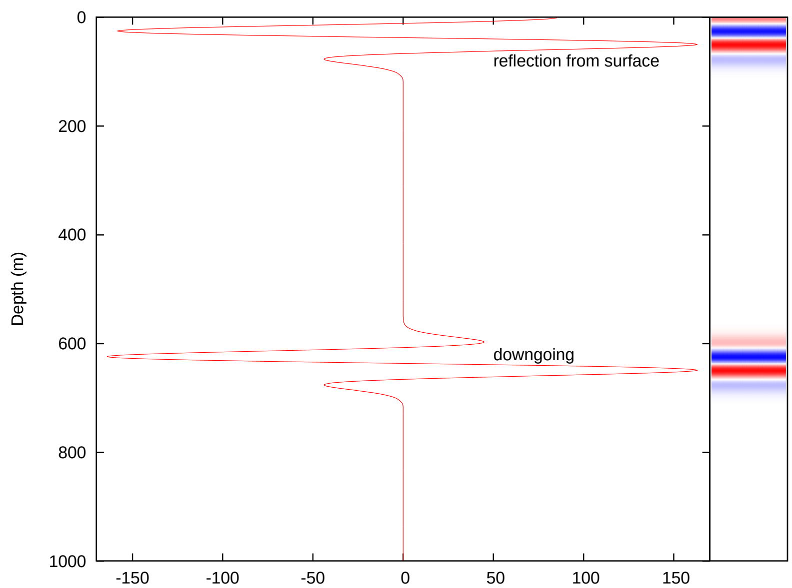

(b) Reflection from surface - enlarged Figure 2.6f and its wiggle plot

Figure 2.7: Incident and reflected waves upon a free surface.

where R is the particle displacement reflection coefficient at the interface of the two media:

$$R = \frac{\rho_2\alpha_2 - \rho_1\alpha_1}{\rho_2\alpha_2 + \rho_1\alpha_1}. \tag{2.36}$$

For an upgoing P-wave normally striking a ground surface from the bottom of the surface, the second medium is air, where $\rho_2 \approx 0$. Therefore, the reflection coefficient is $R = -1$ and $u^{(R)} = u^{(I)}$. In physical terms, this means that there is no amplitude reduction or polarity reversal in the displacement upon reflection from a free surface (Krebes, 2006).

Figure 2.7 shows a wave striking a ground surface from the bottom and its reflection. It can be observed that the reflection upon the free surface has the same amplitude as the incident wave. This is consistent with the theoretical result.

Geometrical spreading of modelled wave

The peak amplitudes shown in Table 2.1 indicate that there is no geometrical spreading. This is consistent with the theory. Theoretically, there should be no geometrical spreading for a 1D wave (or a plane wave in 2D or 3D), since there is no wavefront expansion.

2.3.2.2 A heterogeneous medium with a surface plane wave source

A heterogeneous model, shown in Figure 2.8, contains two layers, with the interface being at the depth of $300m$. The P-wave velocity in the shallow layer is $1000m/s$, and the density is $1741kg/m^3$. The P-wave velocity in the bottom layer is $3000m/s$, and the density is $2291kg/m^3$. The time step is $0.00025s$, and the space grid step is $1m$.

A plane wave source of a symmetric Ricker wavelet is placed at the surface. The

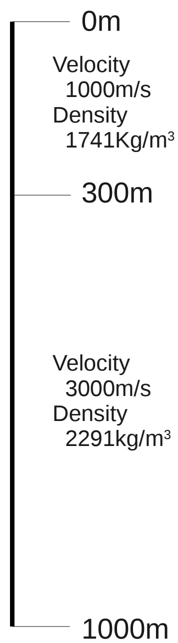

Figure 2.8: A 1D heterogeneous medium.

wave travels down, until it hits the interface between two layers and generates reflected and transmitted waves . The snapshots are shown in Figure 2.9.

With the model, we can check the aspects of modelled wave velocities, modelled wavelengths, reflections and transmissions upon the media interface.

Modelled wave velocity

It is measured that the waves travel at two different velocities, $1000m/s$ and $3000m/s$, when they are in the different media.

Modelled wavelengths

It is observed that the wavelength of the wave at the bottom layer is approximately as three times long as that in the shallow layer. This is reasonable since the wavelength

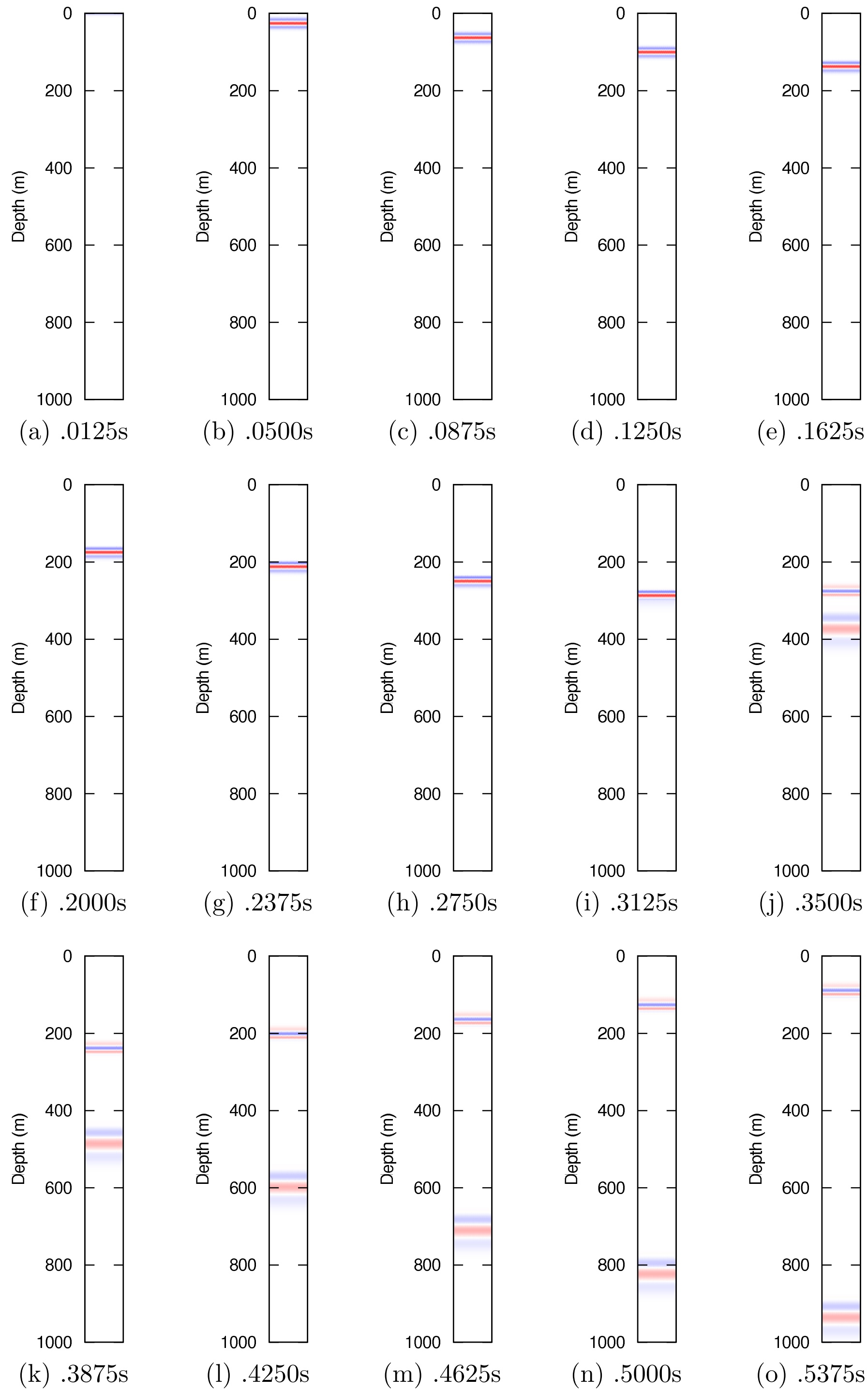

Figure 2.9: Waves in a 1D layered medium (Figure 2.8) with a surface source.

of a wave is determined by wave velocity for a given frequency:

$$\lambda = \frac{v}{f}. \tag{2.37}$$

Modelled wave reflection and transmission

Theoretically, the reflection and transmission coefficients upon the media interface are:

$$\begin{aligned} R &= \frac{\rho_2\alpha_2 - \rho_1\alpha_1}{\rho_2\alpha_2 + \rho_1\alpha_1} \\ &= \frac{2291 \times 3000 - 1741 \times 1000}{2291 \times 3000 + 1741 \times 1000} \\ &= 0.595774, \\ T &= 1 - R \\ &= 1 - 0.595774 \\ &= 0.404226. \end{aligned}$$

The modelled reflection and transmission coefficients can be calculated from measured amplitudes. As shown in Figure 2.10a, The peak of a downgoing wave at time $0.2750s$ is 1.995837 at depth of $249m$. As shown in Figure 2.10b, at time $0.3875s$ the peak amplitude of the upgoing wave is -1.148883 at depth of $238m$, and the peak of the transmitted wave is 0.792668 at depth of $484m$. Since there is no geometrical

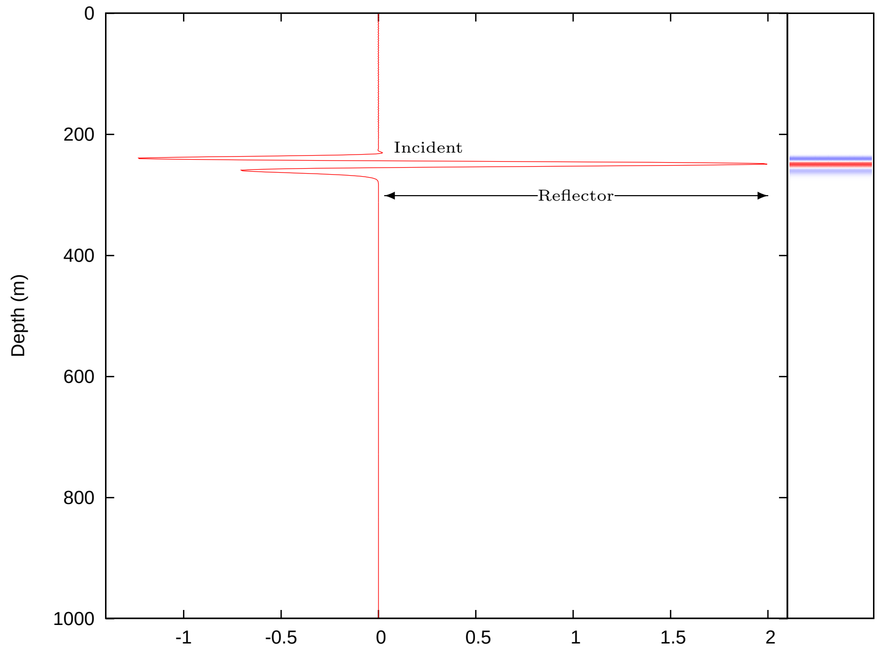

(a) An incident wave at 0.2750s

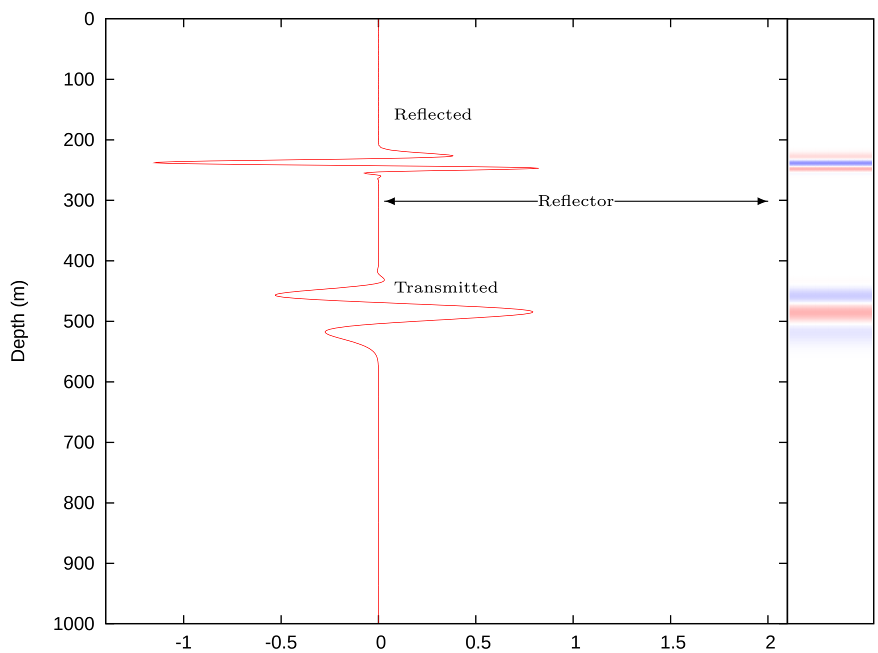

(b) Reflected and transmitted waves at 0.3875s

Figure 2.10: Incident, reflected and transmitted waves in a 1D layered medium (Figure 2.8). The reflector is at the depth of 300m.

spreading, the reflection and transmission coefficients are calculated as:

$$\begin{aligned} R &= \frac{1.148883}{1.995837} \\ &= 0.586783, \\ T &= \frac{0.792668}{1.995837} \\ &= 0.397161, \end{aligned}$$

Thus, the modelled reflection and transmission coefficients are approximately consistent with the analytical results.

2.3.2.3 1D wave modelling summary

From the above experiments, one can conclude that the finite-difference method implicitly implements a lot of wave propagation features, such as wave velocity, reflection and transmission coefficients, wavelength, and geometrical spreading.

2.4 2D SH-wave modelling

It is important to study shear-horizontal (SH) wave, in addition to the more popular P-SV case. "The fact that surface SH waves are observed in nature has been used to infer that the Earth's crust is layered." (Krebes, 2006). SH-wave seismic reflection methods are also employed in natual resource exploration in recent years. For example, Haines and Ellefsen (2010) used SH-wave methods to solve near-surface problems.

2.4.1 Algorithm

Elastodynamic equations

Consider a wave travelling in the plane of $x_1 - x_3$, with the particle vibrations perpendicular to the plane. In this case, only displacements perpendicular to the plane $x_1 - x_3$ exist, and only shear stresses and strains connected to these displacements exist, i.e.,

$$u_1 = u_3 \equiv 0, \tag{2.38a}$$

$$\sigma_{11} = \sigma_{22} = \sigma_{33} = \sigma_{13} = \sigma_{31} \equiv 0, \tag{2.38b}$$

$$e_{11} = e_{22} = e_{33} = e_{13} = e_{31} \equiv 0. \tag{2.38c}$$

Substitution of the above equations into the 3D displacement-stress-strain relations (2.8), one can get elastodynamic equations for the 2D SH-wave case as

$$\rho\frac{\partial^2 u_2}{\partial t^2} = \frac{\partial \sigma_{12}}{\partial x_1} + \frac{\partial \sigma_{23}}{\partial x_3} \tag{2.39a}$$

$$\sigma_{12} = \mu\frac{\partial u_2}{\partial x_1}, \tag{2.39b}$$

$$\sigma_{23} = \mu\frac{\partial u_2}{\partial x_3}, \tag{2.39c}$$

Velocity-stress system

Similar to the conversion from 1D elastodynamic system (2.18) to the 1D velocity-stress wave system (2.22), a 2D velocity-stress SH-wave system can be derived from system (2.39) as

$$\rho \frac{\partial v_2}{\partial t} = \frac{\partial \sigma_{12}}{\partial x_1} + \frac{\partial \sigma_{23}}{\partial x_3}, \tag{2.40a}$$

$$\frac{\partial \sigma_{12}}{\partial t} = \mu \frac{\partial v_2}{\partial x_1}, \tag{2.40b}$$

$$\frac{\partial \sigma_{23}}{\partial t} = \mu \frac{\partial v_2}{\partial x_3}, \tag{2.40c}$$

where v_2 is the shear horizontal particle vibration velocity.

Finite-difference implementation

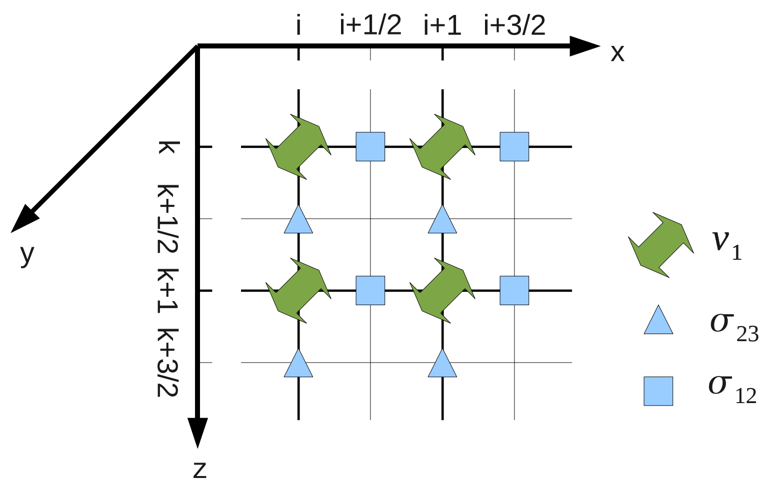

Figure 2.11: A staggered grid for 2D SH-wave modelling.

If a grid step h is used for both x_1 and x_3 axes and Δt is used for the time step, using the staggered-grid schemes introduced by Virieux (1984), one can approximate the 2D velocity-stress system of SH waves as

$$v_{2}{}_{i,k}^{n+1/2} = v_{2}{}_{i,k}^{n-1/2} + \frac{\Delta t}{h\rho_{i,k}} (\sigma_{12}{}_{i+1/2,k}^{n} - \sigma_{12}{}_{i-1/2,k}^{n} + \sigma_{23}{}_{i,k+1/2}^{n} - \sigma_{23}{}_{i,k-1/2}^{n}), \tag{2.41a}$$

$$\sigma_{12}{}^{n+1}_{i+1/2,k} = \sigma_{12}{}^{n}_{i+1/2,k} + \frac{\mu_{i+1/2,k}\Delta t}{h}(v_2{}^{n+1/2}_{i+1,k} - v_2{}^{n+1/2}_{i,k}), \tag{2.41b}$$

$$\sigma_{23}{}^{n+1}_{i,k+1/2} = \sigma_{23}{}^{n}_{i,k+1/2} + \frac{\mu_{i,k+1/2}\Delta t}{h}(v_2{}^{n+1/2}_{i,k+1} - v_2{}^{n+1/2}_{i,k}), \tag{2.41c}$$

where i is the index for x_1 discretization, k is the index for x_3 discretization, and n is the index for time discretization. A schematic diagram of the staggered-grid is shown in Figure 2.11.

Seismic source scheme

Ricker wavelets are introduced into the staggered-grid onto a particle velocity node as shown in Figure 2.12.

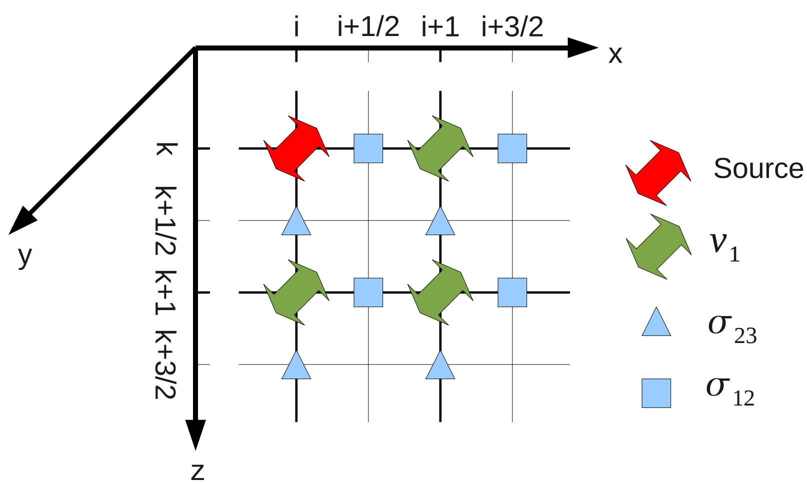

Figure 2.12: Introducing an SH-wave source into a modelling grid.

Seismic resolution is related to seismic source frequencies. One can expect that seismic waves with different frequencies have different spatial wavelengths when they propagate in rocks.

Free-surface boundary condition

In the 2D SH-wave case, the free-surface boundary condition can be denoted as

$$\sigma_{23}\Big|_{x_3=0} \equiv 0, \tag{2.42}$$

since this is the only stress caused by the SH wave that is acting normal to the surface.

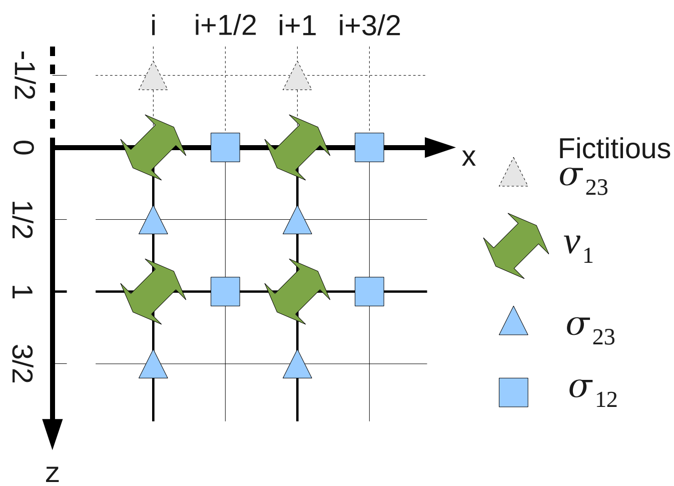

Figure 2.13: A free-surface boundary condition for the SH-wave case.

The discretization form of Equation 2.42 in the specified grid shown in Figure 2.11 is

$$\sigma_{23}\Big|_{k=-1/2} = -\sigma_{23}\Big|_{k=1/2}, \tag{2.43}$$

where subscript $-1/2$ denotes a fictitious stress node about the surface. Since this boundary condition is true at any time at any place on the surface, both the indices for time and offset are ignored. The schematic diagram is shown in Figure 2.13.

Using the boundary condition, one can calculate fictitious stresses above the surface, which in turn, can be used to calculate particle velocities on the free surface at the next half time step.

The method above is based on stresses. Similar to the free-surface boundary condition in section 2.3, another implementation based on particle velocities is also possible.

Computational boundary conditions

Absorbing boundary condition works very well for 1D P-wave case. However, it works not as well in 2D SH case.

To reduce the artificial reflections that are introduced by the edge of the computational grid, a method of combining absorbing boundary conditions (Clayton and Engquist, 1977) and nonreflecting boundary condition (Cerjan et al., 1985) is applied to the sides and bottom of subsurface models. For details about the combined boundary conditions, please refer to Chapter 3 in this dissertation.

2.4.2 Modelling examples

To check the correctness and effectiveness of the wave modelling implementation, a few subsurface models are created, and the modelling results are presented. At the same time, by analyzing these results, one may gain some perceptual knowledge about guided surface SH waves, seismic resolution problem, geometrical spreading, and seismic wave multiples.

2.4.2.1 A homogeneous subsurface with a buried seismic source

The first subsurface model for SH-wave modelling is a $750m$x$750m$ homogeneous medium, with S-wave velocity of $2020.73m/s$ and density of $2380.90kg/m^3$. The grid spatial step is $1.25m$, and the time step is $0.00025s$.

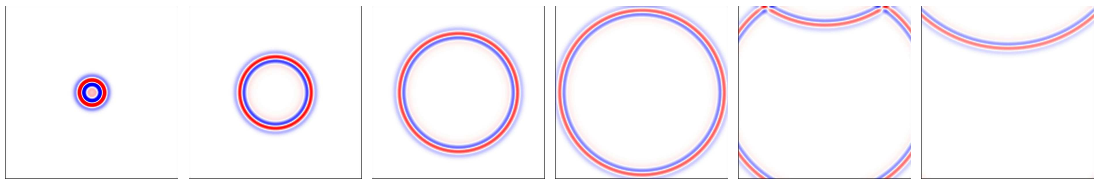

(a) t=0.05s (b) t=0.10s (c) t=0.15s (d) t=0.20s (e) t=0.25s (f) t=0.30s

Figure 2.14: SH waves in a homogeneous media, with a buried seismic source.

By burying a seismic source at the centre of the model and firing it, a shear wave is generated and it propagates outwards. Figure 2.14 shows the wave propagation. When the shear wave hits the bottom as well as both left and right sides of the subsurface model, it just disappears. When the wave reaches the surface from the bottom of the surface, reflections are generated. It can also be observed that the amplitude of the reflection is approximately the same as that of the incident.

Obviously the computational boundary conditions applied to the bottom and the left and the right sides of the subsurface work very well, since there is no noticeable reflections generated from these boundaries.

Similar to the 1D free-surface boundary condition, the 2D free-surface boundary condition applied here for SH waves also works very well.

2.4.2.2 A homogeneous subsurface with a surface seismic source

From a seismic source put at the surface centre of the same subsurface model as the last subsection, an SH wave is generated and it propagates downwards. Figure 2.15 shows the wave propagation.

The distances that wave peaks travelled at different modelling times are shown in table 2.2. It is calculated that the modelled waves travel at the velocity of $2020.00 m/s$, which is very close to the specified value in the subsurface model. That is, the finite-

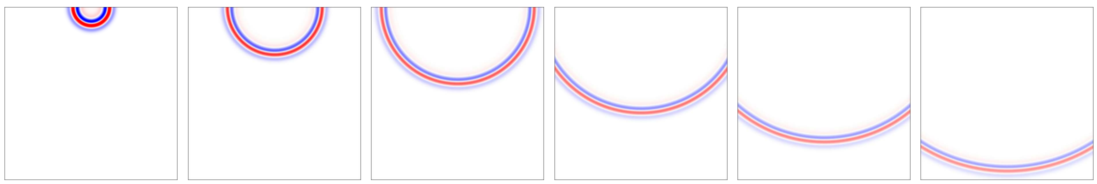

(a) t=0.0625s (b) t=0.1250s (c) t=0.1875s (d) t=0.2500s (e) t=0.3125s (f) t=0.3750s

Figure 2.15: SH waves in a homogeneous media, with a surface seismic source.

Table 2.2: Travel times, distances, and amplitudes of modelled 2D SH waves in a homogeneous medium.

Figure	Time (s)	Distance (m)	Amplitude	Amplitude $\times \sqrt{\text{distance}}$
2.15a	0.0625	80.00	0.02416	0.216
2.15b	0.1250	206.25	0.01495	0.215
2.15c	0.1875	332.50	0.01169	0.213
2.15d	0.2500	458.75	0.00986	0.211
2.15e	0.3125	585.00	0.00863	0.209
2.15f	0.3750	711.25	0.00773	0.206

difference method implicitly implements the propagation velocity of an SH wave.

In addition, from the calculation results of $Amplitude \times \sqrt{distance}$ shown in table 2.2, one can find that the amplitude scales as $\frac{1}{\sqrt{distance}}$. This is different from the plane wave case in 1D wave modelling, where there is no geometrical spreading. This is not the same as the spherical wave propagation in the 3D either, where amplitude scales as $\frac{1}{distance}$. Books, such as the one by Shearer (1999), have explained in detail about the amplitude-distance relation for spherical waves. One can apply the same principles to explain the amplitude-distance relation for circular waves in two dimensional modelling.

Although there are amplitude differences between the 3D real world and 2D modelling, most of the time, this does not cause problems when one utilizes 2D algorithms to process seismic data from the 3D world. However, for amplitude sensitive technologies, such as AVO, we need to have the concept of amplitude differences in mind.

Another interesting observation on this modelling experiment is: there is no surface wave generated in this experiment, which is different from modelling experiments of P-SV case described later. However, this is consistent with the theoretical predictions, "surface SH waves cannot exist on the surface of a homogeneous half-space" (Krebes, 2006). Analysis also tells us, though, surface SH waves can exist on the surface of an inhomogeneous half-space. The next subsection is about an experiment with an inhomogeneous medium, and we can check into surface SH waves.

2.4.2.3 A surface layer above a high velocity half-space

A surface layer model contains two layers: the surface layer is a low wave velocity medium, and below the surface layer is a high speed half-space. For detailed geometry and rock properties of the model, please refer to Table 2.3 and Figure 2.16. The numerical grid spatial step is $0.6m$, and the time step is $0.0001s$. The total modelling time is $0.6001s$

Table 2.3: Parameters of a surface layer model.

Layer	S-wave velocity (m/s)	Density (kg/m^3)	Thickness (m)
Surface layer	577.35	1740.70	60
Half-space	1732.05	2290.89	30

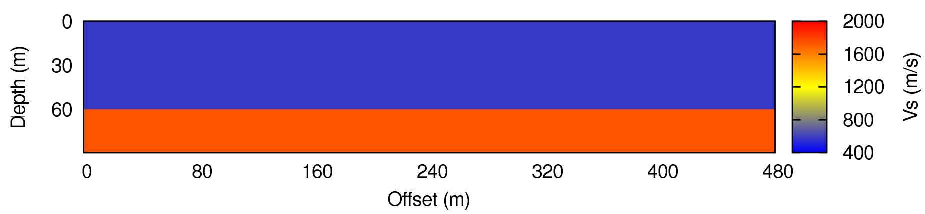

Figure 2.16: A surface layer above a high speed half-space.

In the modelling experiment, a seismic source is placed close to the top-left corner on the surface. Snapshots from the modelling experiment are shown in Figure 2.17. From the snapshots, one can identify direct arrivals, primary reflected waves, transmitted waves, head waves, and multiple reflections. Significantly, most of the wave energy is trapped inside the surface layer and the surface layer acts as a wave guide. That is why the waves are called guided waves.

2.4.2.4 A thin layer model

"How thin is a thin layer?" This is a question posed in a paper (Widess, 1973) and then referenced in a book (Lines and Newrick, 2004). This is a problem of seismic resolution. By analyzing the coming modelling results, one can gain some perceptual

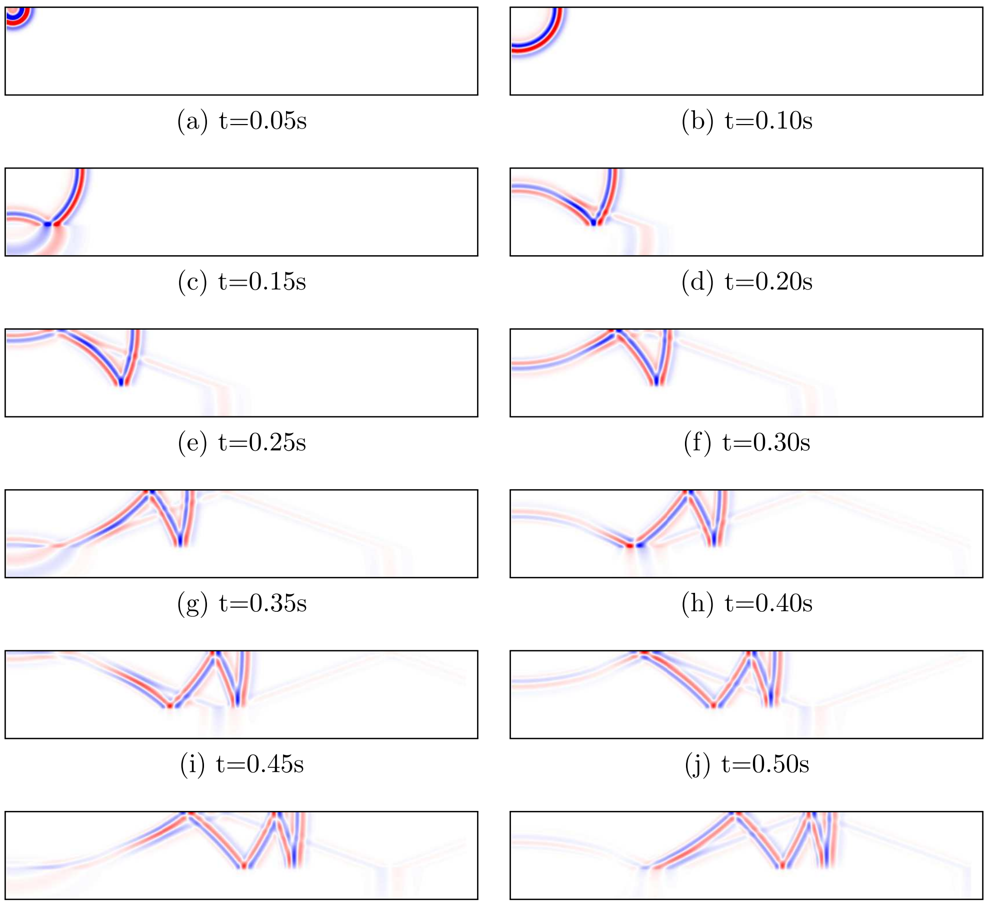

(a) t=0.05s (b) t=0.10s

(c) t=0.15s (d) t=0.20s

(e) t=0.25s (f) t=0.30s

(g) t=0.35s (h) t=0.40s

(i) t=0.45s (j) t=0.50s

(k) t=0.55s (l) t=0.60s

Figure 2.17: Guided SH waves in a surface layer model.

knowledge about this problem.

In the subsurface model shown in Figure 2.18, a thin layer is presented in surrounding rocks. The thickness of the thin layer is $41m$. The overburden rock has a thickness of $460m$. The S-wave velocities of the thin layer and the surrounding rock are, respectively, $1443.38m/s$ and $2020.73m/s$. The densities are $2188.82kg/m^3$ and $2380.90kg/m^3$. The grid spatial step is $1m$, and the time step is $0.0002s$.

Two seismic experiments are done with the seismic sources being put on the surface centre. The only difference is the peak frequencies of the seismic sources: one is of $12Hz$, while the other is of $40Hz$. Note that since the relation between wavelength, velocity and frequency $\lambda = \frac{v}{f}$, a $12Hz$ signal in a medium of S-wave velocity being $2020.73m/s$ has a wavelength of approximately $163m$, which is as four times long as the thickness of the thin layer. While a signal of $40Hz$ has a wavelength of approximately $50.5m$, which is close to $\frac{5}{4}$ times of the thickness of the thin layer.

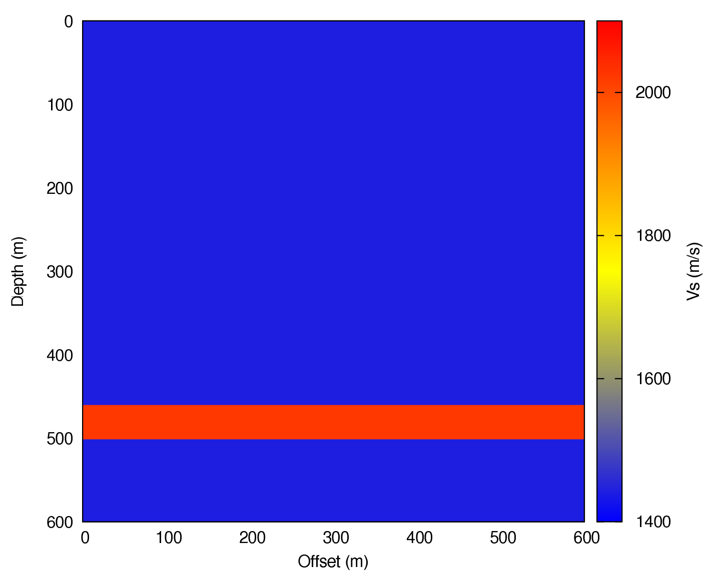

Figure 2.18: A thin layer model.

Figure 2.19 shows surface records from the two seismic experiments. Direct arrivals appears as linear events on the upper parts of the records, and reflection events appears as hyperbolas on the lower parts. On the surface record of low frequency seismic source (Figure 2.19a), one can only identify one reflection event. However, on the record of high frequency source (Figure 2.19b), the two reflection events are completely separated into two hyperbolas.

How thin is a thin layer? The answer is that it depends on the wavelength of a seismic signal, which in turn, depends on the wave velocities in media and seismic frequencies. The higher the peak frequency of the seismic source and the lower the wave velocity in media, the better one can distinguish thin media layers. For a certain medium, we cannot change the wave velocity, but we can utilize seismic sources of higher frequencies to gain higher resolution survey results.

2.5 2D P-SV wave modelling

This section describes the algorithm of 2D P-SV wave modelling, followed by a few modelling examples, which are used in the experiment of reverse-time migration later in the dissertation.

Sometimes the SV wave is called S wave in this section.

2.5.1 Algorithm

Elastodynamic system

Consider a wave travelling in the plane of $x_1 - x_3$, with the particle vibrations parallel to the plane. In this case, only the displacements parallel to the plane $x_1 - x_3$ exist,

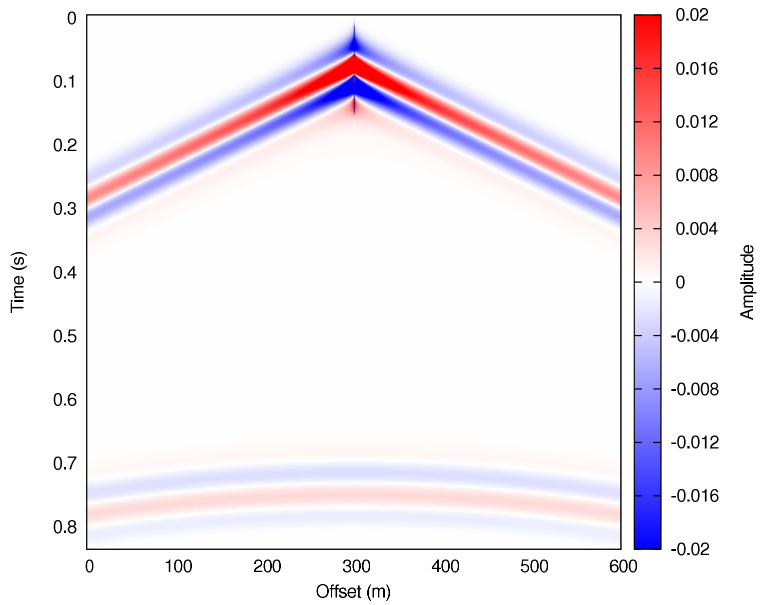

(a) f=12Hz

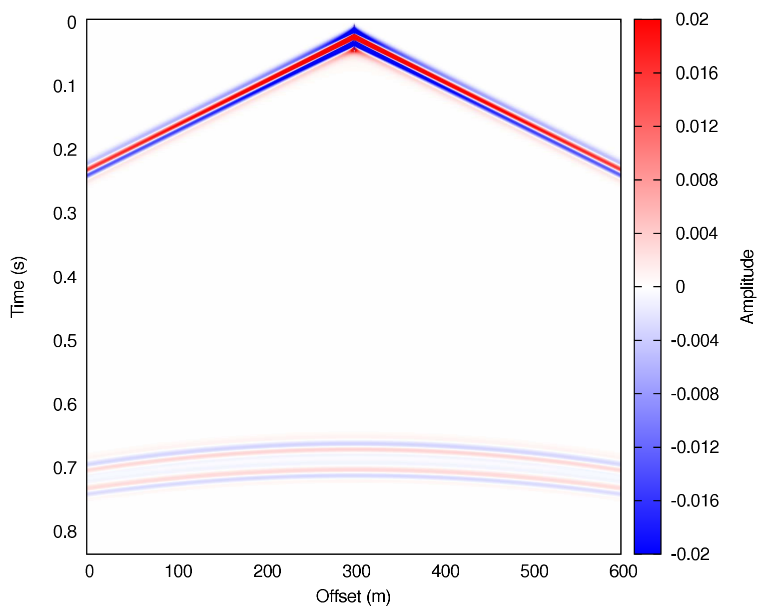

(b) f=40Hz

Figure 2.19: Surface records generated from different source peak frequencies using the thin layer model shown in Figure 2.18.

and only stresses and strains connected to these displacements exist, i.e.,

$$u_2 \equiv 0, \tag{2.44a}$$

$$\sigma_{2j} = \sigma_{j2} \equiv 0, \quad j = 1, 2, 3, \tag{2.44b}$$

$$e_{2j} = e_{j2} \equiv 0, \quad j = 1, 2, 3. \tag{2.44c}$$

Substituting the above equations into the 3D displacement-stress-strain relations (2.8), one obtains elastodynamic equations for the 2D SH-wave case as

$$\rho \frac{\partial^2 u_1}{\partial t^2} = \frac{\partial \sigma_{11}}{\partial x_1} + \frac{\partial \sigma_{13}}{\partial x_3}, \tag{2.45a}$$
$$\rho \frac{\partial^2 u_3}{\partial t^2} = \frac{\partial \sigma_{13}}{\partial x_1} + \frac{\partial \sigma_{33}}{\partial x_3}, \tag{2.45b}$$
$$\sigma_{11} = (\lambda + 2\mu)\frac{\partial u_1}{\partial x_1} + \lambda \frac{\partial u_3}{\partial x_3}, \tag{2.45c}$$
$$\sigma_{33} = (\lambda + 2\mu)\frac{\partial u_3}{\partial x_3} + \lambda \frac{\partial u_1}{\partial x_1}, \tag{2.45d}$$
$$\sigma_{13} = \mu(\frac{\partial u_3}{\partial x_1} + \frac{\partial u_1}{\partial x_3}). \tag{2.45e}$$

Velocity-stress system

Similar to the conversion from the 1D elastodynamic system (2.18) to the 1D velocity-stress wave system (2.22), a 2D velocity-stress P-SV wave system can be derived from system (2.45) as

$$\rho \frac{\partial v_1}{\partial t} = \frac{\partial \sigma_{11}}{\partial x_1} + \frac{\partial \sigma_{13}}{\partial x_3}, \tag{2.46a}$$
$$\rho \frac{\partial v_3}{\partial t} = \frac{\partial \sigma_{13}}{\partial x_1} + \frac{\partial \sigma_{33}}{\partial x_3}, \tag{2.46b}$$

$$\frac{\partial \sigma_{11}}{\partial t} = (\lambda + 2\mu)\frac{\partial v_1}{\partial x_1} + \lambda \frac{\partial v_3}{\partial x_3}, \tag{2.46c}$$

$$\frac{\partial \sigma_{33}}{\partial t} = (\lambda + 2\mu)\frac{\partial v_3}{\partial x_3} + \lambda \frac{\partial v_1}{\partial x_1}, \tag{2.46d}$$

$$\frac{\partial \sigma_{13}}{\partial t} = \mu(\frac{\partial v_3}{\partial x_1} + \frac{\partial v_1}{\partial x_3}), \tag{2.46e}$$

where v_1 and v_3 are, respectively, the horizontal and vertical components of particle vibration velocities.

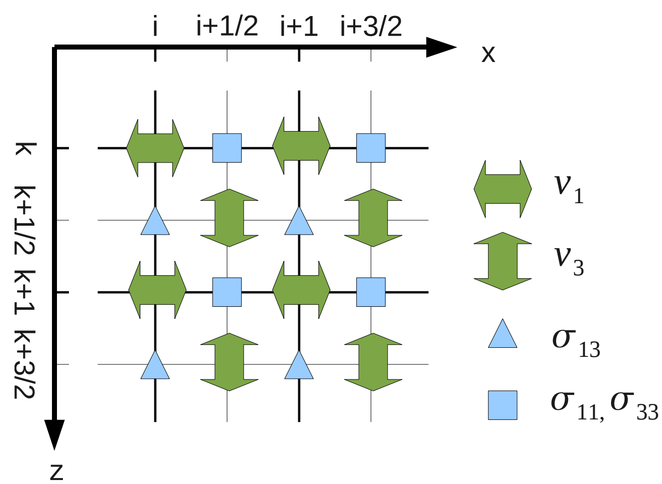

Figure 2.20: A staggered grid for 2D P-SV wave modelling.

Finite-difference approximation

If a grid step h is used for both x_1 and x_3 axes and Δt is used for the time step, using the staggered-grid schemes introduced by Virieux (1986), one can approximate the 2D velocity-stress system of P-SV waves as

$$\begin{aligned} {v_1}_{i,k}^{n+1/2} = {v_1}_{i,k}^{n-1/2} + \frac{\Delta t}{h\rho_{i,k}}(&{\sigma_{11}}_{i+1/2,k}^{n} - {\sigma_{11}}_{i-1/2,k}^{n} \\ &+ {\sigma_{13}}_{i,k+1/2}^{n} - {\sigma_{13}}_{i,k-1/2}^{n}), \end{aligned} \tag{2.47a}$$

$$v_{3}{}^{n+1/2}_{i+1/2,k+1/2} = v_{3}{}^{n-1/2}_{i+1/2,k+1/2} + \frac{\Delta t}{h\rho_{i+1/2,k+1/2}}(\sigma_{13}{}^{n}_{i+1,k+1/2} - \sigma_{13}{}^{n}_{i,k+1/2}$$
$$+ \sigma_{33}{}^{n}_{i+1/2,k+1} - \sigma_{33}{}^{n}_{i+1/2,k}), \tag{2.47b}$$
$$\sigma_{11}{}^{n+1}_{i+1/2,k} = \sigma_{11}{}^{n}_{i+1/2,k} + \frac{(\lambda+2\mu)_{i+1/2,k}\Delta t}{h}(v_{1}{}^{n+1/2}_{i+1,k} - v_{1}{}^{n+1/2}_{i,k})$$
$$+ \frac{\lambda_{i+1/2,k}\Delta t}{h}(v_{3}{}^{n+1/2}_{i+1/2,k+1/2} - v_{3}{}^{n+1/2}_{i+1/2,k-1/2}), \tag{2.47c}$$
$$\sigma_{33}{}^{n+1}_{i+1/2,k} = \sigma_{33}{}^{n}_{i+1/2,k} + \frac{(\lambda+2\mu)_{i+1/2,k}\Delta t}{h}(v_{3}{}^{n+1/2}_{i+1/2,k+1/2} - v_{3}{}^{n+1/2}_{i+1/2,k-1/2})$$
$$+ \frac{\lambda_{i+1/2,k}\Delta t}{h}(v_{1}{}^{n+1/2}_{i+1,k} - v_{1}{}^{n+1/2}_{i,k}), \tag{2.47d}$$
$$\sigma_{13}{}^{n+1}_{i,k+1/2} = \sigma_{13}{}^{n}_{i,k+1/2} + \frac{\mu_{i,k+1/2}\Delta t}{h}$$
$$(v_{3}{}^{n+1/2}_{i+1/2,k+1/2} - v_{3}{}^{n+1/2}_{i-1/2,k+1/2} + v_{1}{}^{n+1/2}_{i+1,k} - v_{1}{}^{n+1/2}_{i,k}), \tag{2.47e}$$

where i is the index for x_1 discretization, k is the index for x_3 discretization, and n is the index for time discretization. A schematic diagram of the staggered-grid is shown in Figure 2.20.

The stability condition is

$$V_p \frac{\Delta t}{h} < \frac{1}{\sqrt{2}}, \tag{2.48}$$

where V_p is the P-wave velocity.

Seismic source scheme

An explosive source, shown in Figure 2.21, is used. Four zero-phase Ricker wavelets were introduced into a staggered-grid model, with displacement directed uniformly about a centre. Manning (2008) has successfully used this source scheme in his dissertation.

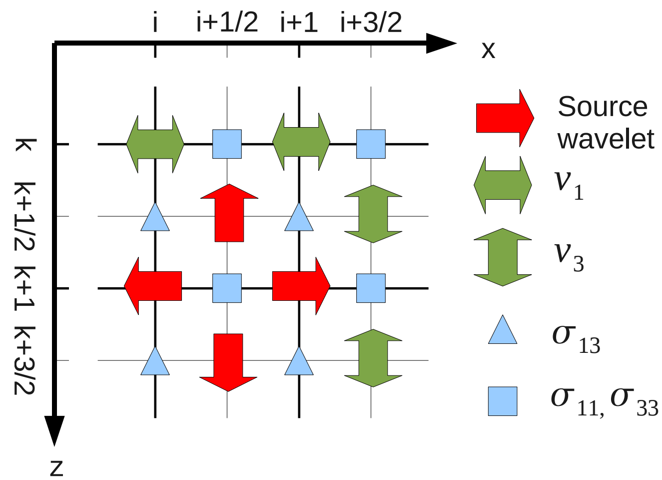

Figure 2.21: Seismic energy source scheme for 2D P-SV wave modelling.

Free-surface boundary conditions

In the 2D P-SV wave case, free-surface boundary conditions can be denoted as

$$\sigma_{33}\Big|_{x_3=0} \equiv 0, \tag{2.49a}$$

$$\sigma_{13}\Big|_{x_3=0} \equiv 0, \tag{2.49b}$$

where σ_{13} is the stress connected to the horizontal component of wave displacement, and σ_{33} is the one connected to the vertical component.

In a discretization scheme shown in Figure 2.20, one uses Equation (2.49a) directly, while he or she needs to use a central difference to approximate Equation (2.49b), since the quantities σ_{13} are not on the discretization nodes. Thus, Equations (2.49) are rewritten as

$$\sigma_{33}\Big|_{k=0} = 0, \tag{2.50a}$$

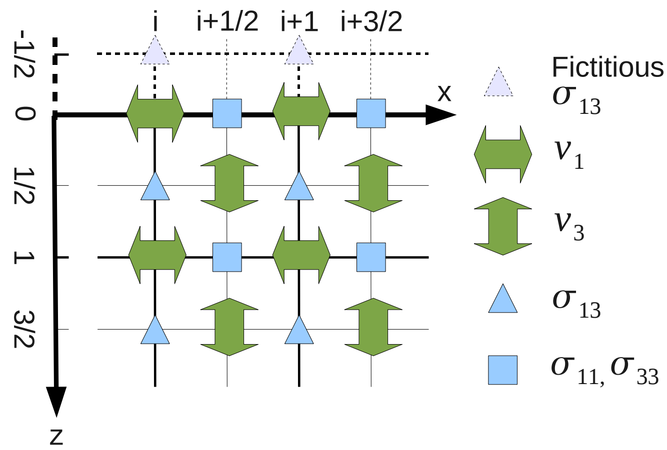

Figure 2.22: A free-surface boundary for 2D P-SV wave modelling.

$$\sigma_{13}\Big|_{k=-1/2} = -\sigma_{13}\Big|_{k=1/2}, \tag{2.50b}$$

where subscript $-1/2$ denotes a fictitious stress node about the surface. Since these boundary conditions are true any time any place on the surface, the indices for both time and offset are ignored. The schematic diagram is shown in Figure 2.22.

Computational boundary conditions

The details will be discussed in the Chapter 3.

2.5.2 Modelling examples

2.5.2.1 A point reflector subsurface model

A 2D subsurface model contains a point reflector in a homogeneous medium in x_1-x_3 plane is built. The P-wave velocity is shown in Figure 2.23.

The parameters used in P-SV modelling are Lamé parameters, λ and μ, and density, ρ. These parameters are derived from the P-wave velocities. The procedures are:

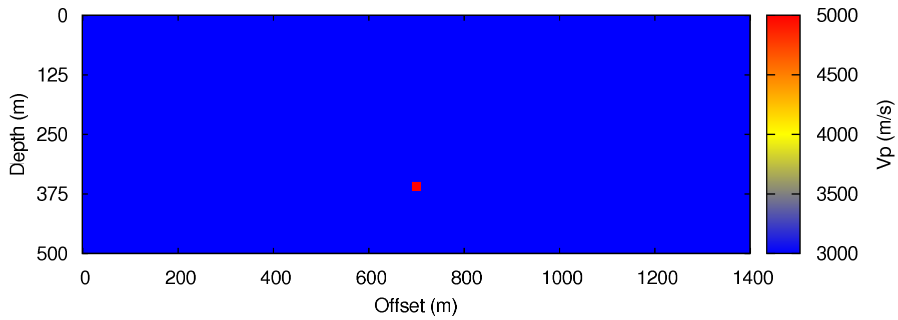

Figure 2.23: A point reflector model.

1. Densities are calculated from P-wave velocities by Gardner's relationship, which expresses density, ρ, in terms of P-wave velocities, v_p, as

$$\rho = \beta v_p^{\alpha}, \tag{2.51}$$

where α and β are constant coefficients for certain medium. According to Lines and Newrick (2004), reasonable values for these coefficients are $\alpha = 0.25$ and $\beta = 0.23$ for velocity in ft/s and density in gm/cm^3. Thus, using SI derived units, one can denote Gardner's relationship as

$$\rho = 2300(3.2808399 v_p)^{0.25}. \tag{2.52}$$

2. Assuming the Poisson's ratios of the medium to be 0.25, S-wave velocities are calculated from P-wave velocities by the following relationship.

$$v_s = v_p \sqrt{\frac{\frac{1}{2} - \sigma}{1 - \sigma}}. \tag{2.53}$$

3. Lamé parameters, λ and μ, are calculated by

$$\mu = \rho v_s^2, \tag{2.54a}$$

$$\lambda = \rho v_p^2 - 2\mu. \tag{2.54b}$$

The parameters of the point reflector model are shown in Table 2.4.

As shown in Figure 2.23, the subsurface is $1400m$ wide and $500m$ high. With a spatial step of $1m$, there are 1400 nodes in offset and 500 nodes in depth. The point reflector is a square with side length of $18m$, positioned at offset from $691m$ to $709m$, and at depth from $350m$ to $368m$.

This subsurface model is used for both P-SV modelling and reverse-time migration. There are two reasons why this model is of interest. First, this is a relatively simple model compared to other models. There are only two physical reflectors. One is the point reflector, and the other one is the free surface. Although it turns out that the wave propagation accompanying with the model is not simple at all, the model is simpler than any other models except a homogeneous model. Second, according to Huygens' principle, without loss of generality, any modelling and migration algorithms which work properly on this point reflector subsurface model should work properly for any other models.

2.5.2.2 Modelling with a buried P-wave source

A modelling experiment is done using the point reflector subsurface model shown in Figure 2.23. A time step of $0.0001s$ is set for wave modelling. Put a seismic energy source illustrated in Figure 2.21 at offset of $350m$ and depth of $250m$, a wave is

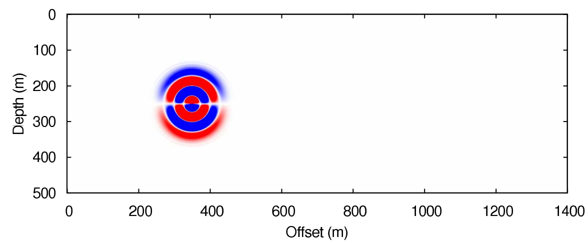

(a) Vertical component, 0.04s

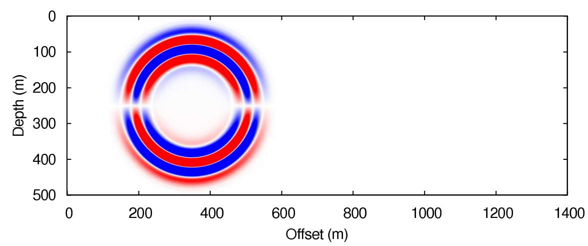

(b) Vertical component, 0.08s

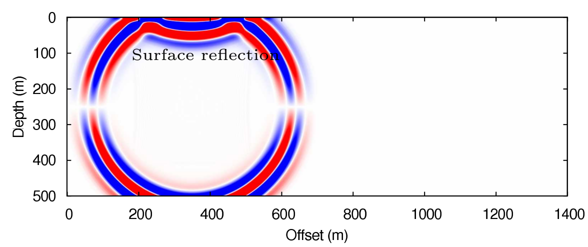

(c) Vertical component, 0.12s

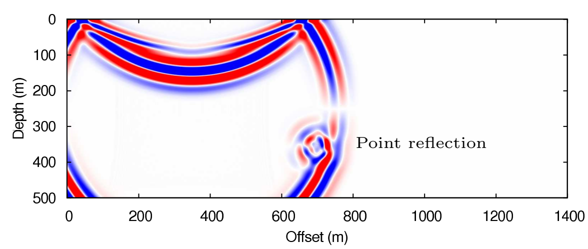

(d) Vertical component, 0.16s

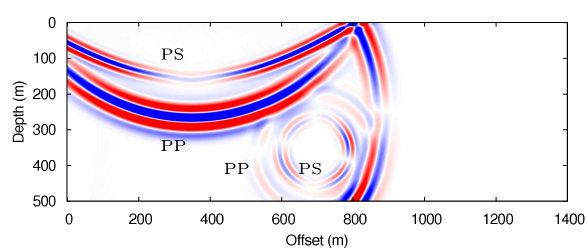

(e) Vertical component, 0.20s

Figure 2.24: P-SV wave generated from a buried source [to be continued].

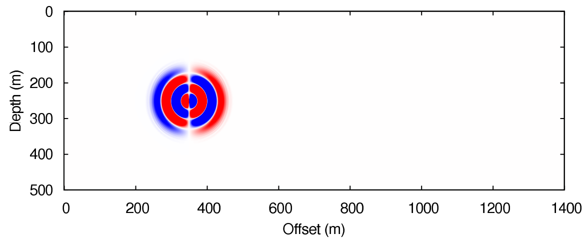

(f) Horizontal component, 0.04s

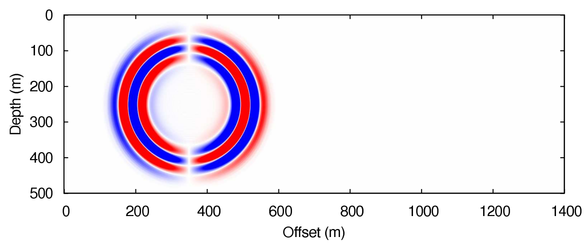

(g) Horizontal component, 0.08s

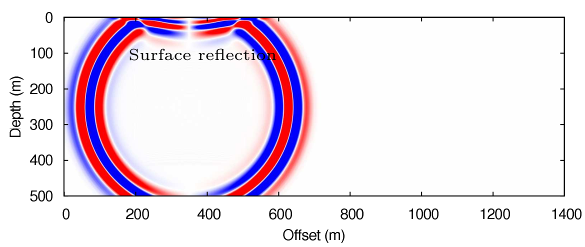

(h) Horizontal component, 0.12s

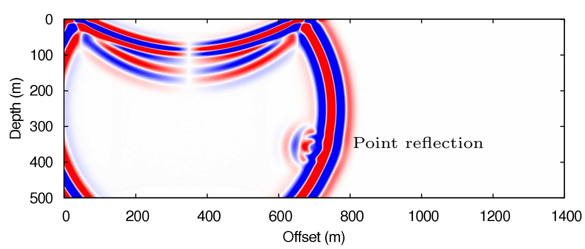

(i) Horizontal component, 0.16s

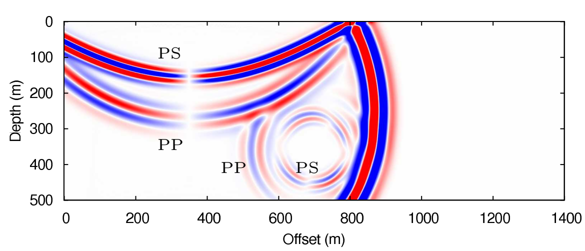

(j) Horizontal component, 0.20s

Figure 2.24: [Continued]

Table 2.4: Parameters of a point reflector model.

Rock	$v_p(m/s)$	$v_s(m/s)$	$\rho(kg/m^3)$	$\lambda(GPa)$	$\mu(GPa)$
Point reflector	5000.00	2886.75	2602.95	21.69	21.69
Surrounding rock	3000.00	1732.05	2290.89	6.87	6.87

generated and it starts to propagate outwards.

Figure 2.24 shows the wave propagation snapshots from time $0.04s$ to $0.20s$. The first five snapshots are the vertical component of the wave and the next five are the corresponding horizontal component. The vertical component snapshots show opposite polarities upon the horizontal line crossing the source point, while the horizontal component snapshots show opposite polarities upon the vertical line crossing the source point. The wave first propagates as a pure P-wave, since it is in a homogeneous medium, as shown in snapshots of times $0.04s$ and $0.08s$. Then the wave hits the free surface from the bottom and surface reflections are generated. Snapshots of time $0.12s$ show the surface reflections. At time $0.16s$, the wave has already reached the point reflector and more reflections can be observed. The P- and S-wave reflections from both the surface and the point can be clearly distinguished from each other in the $0.20s$ snapshots.

The point reflections are centred by the point reflector and it looks like the reflected energy is generated by the point. That can be explained by Huygens's principle: every point on a wave front can be regarded as a new source of waves.

2.5.2.3 Modelling with a surface source above the point reflector

A surface source modelling is accomplished with the same point reflector subsurface model. A time step of $0.0001s$ is set for wave modelling.

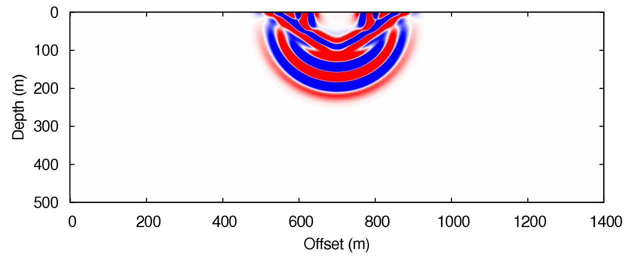

(a) Vertical component, 0.08s

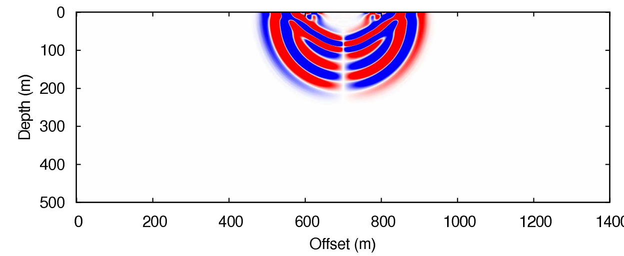

(b) Horizontal component, 0.08s

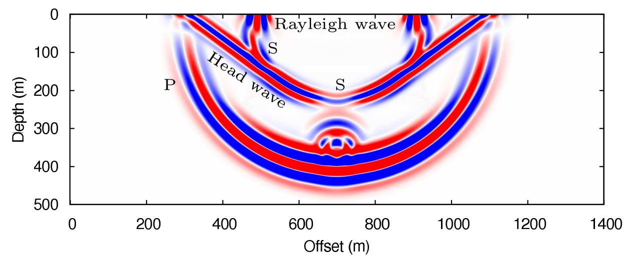

(c) Vertical component, 0.16s

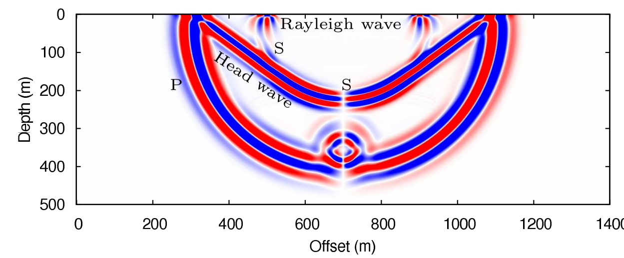

(d) Horizontal component, 0.16s

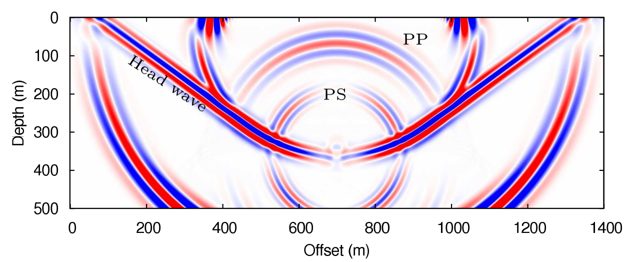

(e) Vertical component, 0.24s

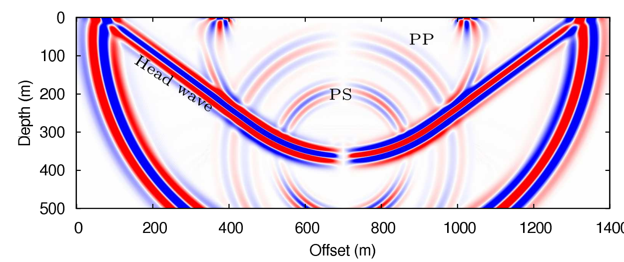

(f) Horizontal component, 0.24s

Figure 2.25: P-SV wave propagation with a centre surface source [to be continued].

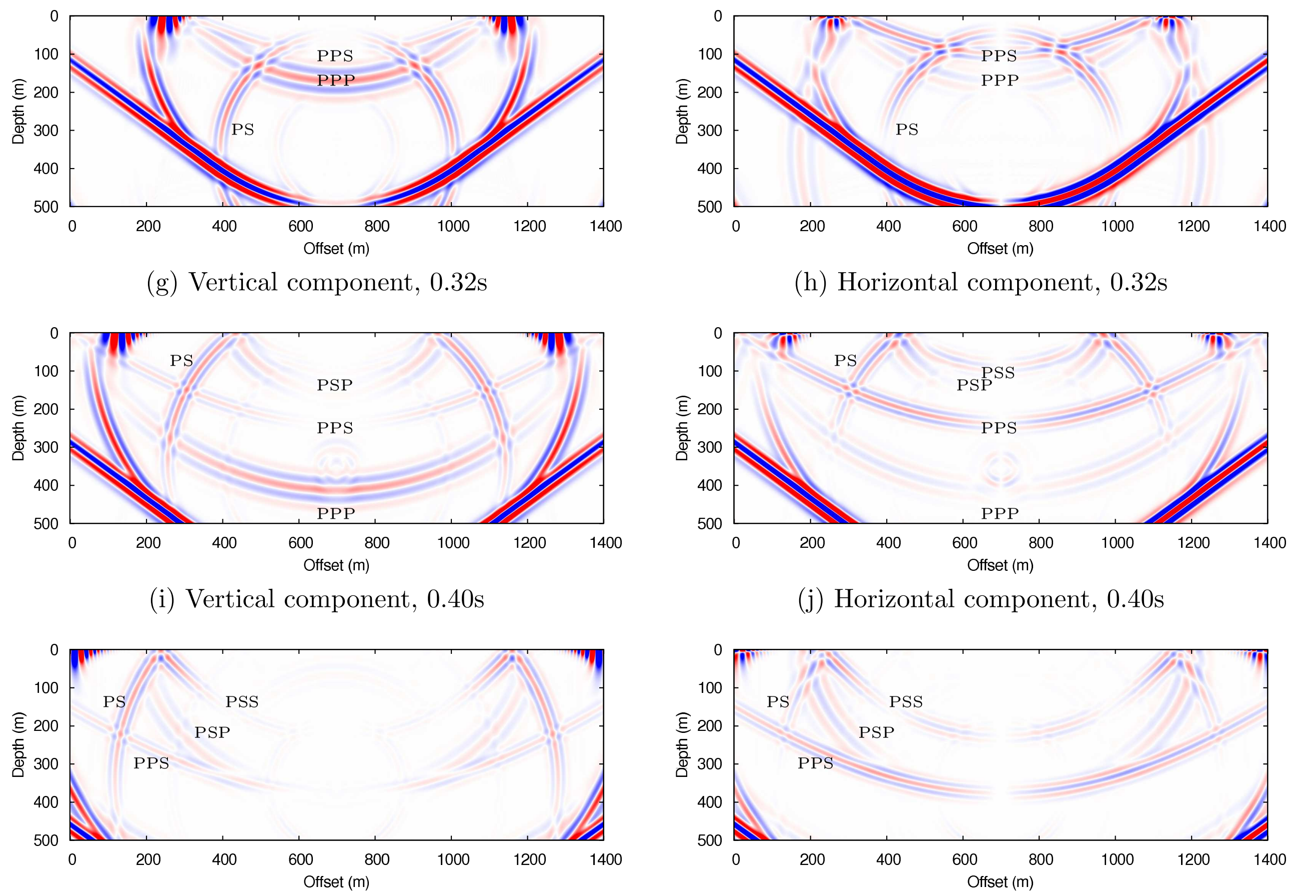

(g) Vertical component, 0.32s

(h) Horizontal component, 0.32s

(i) Vertical component, 0.40s

(j) Horizontal component, 0.40s

(k) Vertical component, 0.48s

(l) Vertical component, 0.48s

Figure 2.25: [Continued]

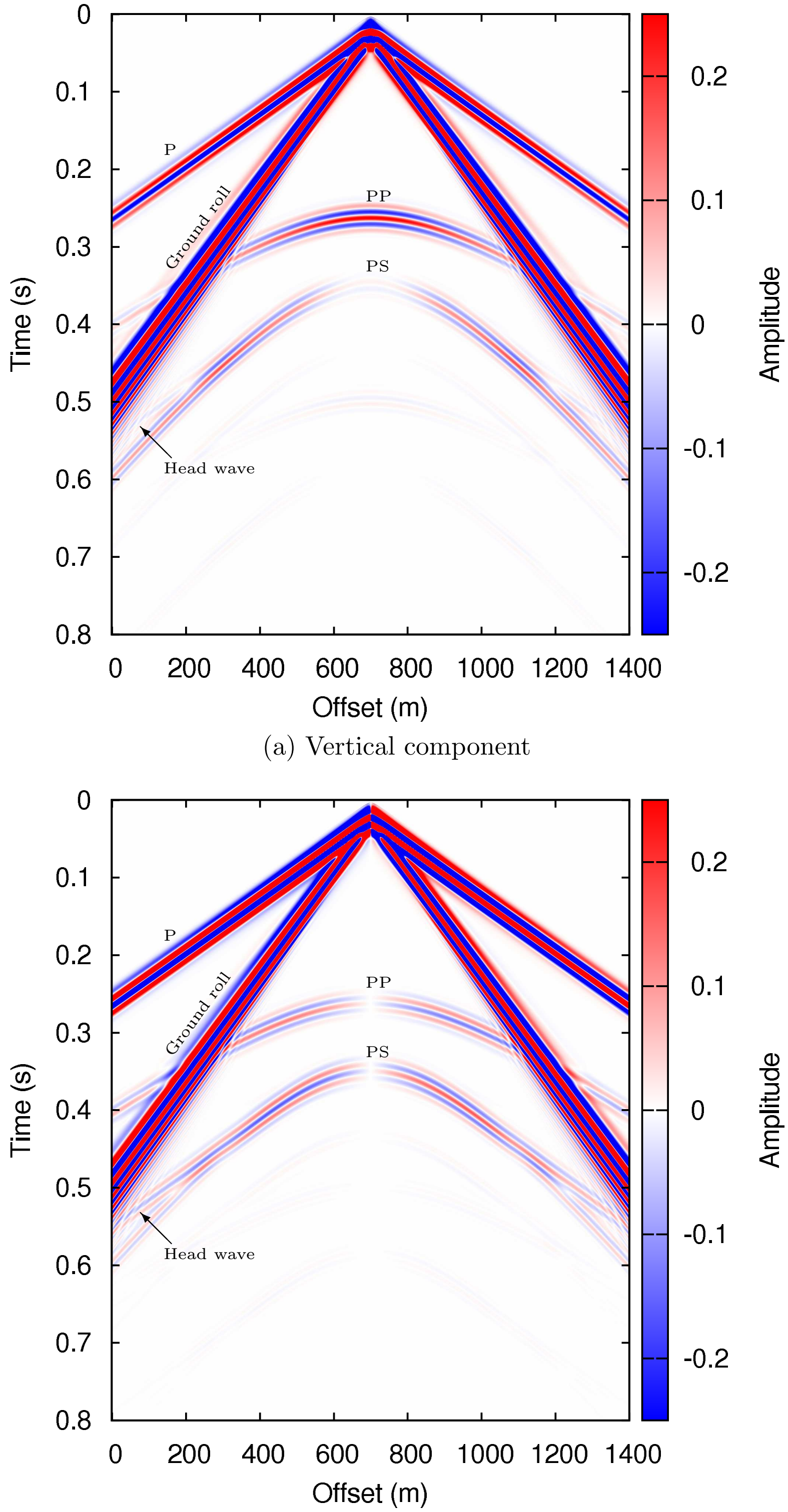

(a) Vertical component

(b) Horizontal component

Figure 2.26: P-SV surface record with a centre surface source.

A P-wave seismic source, illustrated in Figure 2.21, is put at a $10m$ below the centre of the surface. That it, the source is vertically above the point reflector. Dynamite charges for land surveys are commonly buried in shot holes, with a wide range of depths from 1 meter to 35 meters. However, compared to the depth range of seismic wave surveys, the seismic energy source is still very close to the earth surface.

Figure 2.25 shows the wave propagation snapshots from time $0.08s$ to $0.40s$. Both vertical and horizontal components are included.

Although a pure P-wave source, same as in the buried-source modelling experiment, is used, waves generated close to the source point include P waves, S waves, downgoing head waves, and Rayleigh waves, as shown in Figure 2.25c, 2.25d, 2.25e, and 2.25f.

Why both P and S waves are generated from a pure P-wave source? One can imagine that at first, there is only a P-wave circle front generated from the source point, and then the upper part hits the free surface and both reflected P waves and S waves are generated. Since the reflected P waves are very close to the lower part of the source P-wave circle, they mix and propagate down as one P-wave front. On the other hand, the reflected S wave propagates down as another wave front. Since the time difference between the source wave generation and the S wave resulted from surface reflection is very small, the reflected S wave propagates downwards as if it is generated from the source point.

The downgoing head waves that connect the P and S wavefronts are plane S waves in the 2D P-SV modelling experiments. The head waves are generated when the faster P wavefront breaks away from the slower S wavefront. This can be explained by Huygens' principle (see Krebes, 2006, chap. 4).

Rayleigh waves are also generated. In Chapter 3 and 4 of the course notes by Krebes (2006), there is detailed mathematical analysis about Rayleigh wave. Here one may be interested in observing some of the Rayleigh wave properties stated in the mentioned course notes. First, the Rayleigh wave is considered as one kind of evanescent wave, which travels along the surface and its amplitude decreases with depth. Second, Rayleigh wave velocity c is approximated as

$$c \approx \frac{0.862 + 1.14\sigma}{1+\sigma}\beta, \tag{2.55}$$

where σ is Poisson′s ratio and β is shear wave velocity. Since $\sigma = 0.25$ in the point reflector subsurface model, Rayleigh wave velocity is expected to be modelled as $c \approx 0.918\beta$ theoretically. Modelling results confirm the theoretical prediction. In fact, when the surface wave is removed from modelled surface records for reverse-time migration later in the dissertation, this velocity is used in the muting operation. Third, Rayleigh waves decay more slowly than body waves. In the real 3D world, the body waves decay as $\frac{1}{r}$, where r is distance, and Rayleigh waves decay as $\frac{1}{\sqrt{r}}$. In the 2D P-SV modelling, body waves decay as $\frac{1}{\sqrt{r}}$, while Rayleigh waves do not decay at all.

In addition to the above P waves, S waves, downgoing head waves, and Rayleigh waves, there are also reflections upon the point reflector. As shown in Figure 2.25c and 2.25d, before time 0.16s, P wave has striked the point reflector and wave reflections have already shown up. At snapshots of time 0.24s, as shown in Figure 2.25e and 2.25f, one can identify the reflections including both P- and S-wave reflections, which are annotated, respectively, as PP and PS in the figure. At time 0.24s, S wave has already reached the point reflection, but there is almost no reflections, since the S-wave amplitudes at the centre part are very weak.

The point reflections, PP and PS, propagate outwards. When their upper parts hit the free surface, they are reflected back down again.

PP-wave reflections upon the surface is annotated as PPP and PPS in Figure 2.25. Wave PPP is the P-wave reflection of wave PP, and wave PPS is the S-wave reflection. In this case, particle vibrations of Wave PPP is mainly vertical. Therefore PPP is more significant in the vertical component plots, as shown in Figure 2.25g and 2.25i, than in the horizontal component plots, as shown in Figure 2.25h and 2.25j. On the other hand, particle vibrations of wave PPS is mainly horizontal. Therefore PPS is more significant in horizontal plots than in vertical ones.

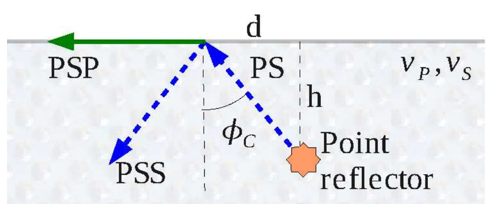

Figure 2.27: A PS wave strikes a free surface from its bottom, with the incident angle equals to the critical angle.

An interesting phenomenon is head waves generated by the PS wave striking the free surface from the bottom. The PS wave is the shear wave reflection resulted from the incident P wave striking the point reflector. According to Huygens' principle, the point reflector can be regarded as a point source and the PS wave is generated from it with a circular wavefront. When the PS wave strikes the free surface from the bottom, at first the incident angle is 0, and only reflected shear wave is generated.

Then the PS wave generates both P- and S-wave reflections upon earth surface, called, respectively, PSP and PSS waves (Figure 2.25i and 2.25j), when the incident angles are greater than 0. Denote the incident angle of the PS wave as ϕ, the reflection angle of the PSP wave as θ, and the P- and S-wave velocities as v_P and v_S, according to Snell's law,

$$\frac{sin\phi}{v_S} = \frac{sin\theta}{v_P}. \tag{2.56}$$

Hence, there is a critical angle ϕ_C of ϕ at which $\theta = 90°$.

When the incident angle ϕ is smaller than the critical angle ϕ_C, the PSP and PSS waves share the same wavefront position on the surface, although they have separated wavefronts inside the subsurface.

When the incident angle ϕ reaches and then is beyond the critical angle ϕ_C, the PSP wavefront breaks away from the PSS wavefront (Figure 2.27). For the given subsurface model with $v_P = 3000.00km/s$ and $v_S = 1732.05km/s$, as shown in Table 2.4, the critical angle for the incident PS wave is calculated as

$$\begin{aligned} \phi_C &= \sin^{-1}(\frac{v_S}{v_P}) \\ &= \sin^{-1}(\frac{1732.05}{3000.00}) \\ &= 35.26°. \end{aligned} \tag{2.57}$$

From the geometry shown in Figure 2.27, the horizontal distance d that the PS wave have travelled when the PSP and PSS wavefronts break away from each other is calculated as

$$
\begin{aligned}
d &= h \tan \phi_C \\
&= 359 \tan 35.26^\circ \\
&= 253.8m.
\end{aligned}
\tag{2.58}
$$

where $h = 359m$ is the depth of the point reflector. Since the offset of the point reflector is $700m$, one can expect the PSP-PSS breakaway happens at the offset of $700 - 253.8 = 446.2m$. At time $0.40s$, the left PS-wave peak has already reached around offset $420m$. Thus, the PSP-PSS breakaway should have already happened (Figure 2.25i and 2.25i), although it is difficult to observe because of the wavelength. At time $0.48s$, however, it is very clear that PSP and PSS waves have separated from each other (Figure 2.25k and 2.25l). Note that, since the shallow PSP-wave causes mainly horizontal particle vibrations, the breaking-away effect is more evident on the horizontal component snapshot (Figure 2.25l) than on the vertical one (Figure 2.25k).

The same phenomenon can be observed on the right side of the seismic source as well.

On the surface records, as shown in Figure 2.26, the strong events are direct P waves, Rayleigh waves, PP and PS waves. Among them, amplitudes of Rayleigh waves and direct waves are much stronger than the reflections. The effect of the PSP-wave front breaking away from the PSS wave can be clearly observed from time $0.47s$ to $0.6s$ on the PS reflection event. As in the snapshots, the effect is also more evident on the horizontal component (Figure 2.26b) than on the vertical one (Figure 2.26a).

2.5.2.4 Modelling with a surface source horizontally far away

Another modelling experiment is done by putting a surface seismic energy source at an offset of $400m$ from the top-left corner of the subsurface. In this case,the source is about horizontally $300m$ away from the point reflector.

The snapshots are shown in Figure 2.28.

At first, as in the modelling experiment in the last subsection, P- and S-waves, Rayleigh waves, and downgoing head waves are generated close to the source and propagate outwards.

Then reflections upon the point reflector are generated. There are two incident waves upon the point reflector. First, a P wavefront strikes it, and is reflected as P and S waves, called PP and PS. Second, an S wavefront reaches the point reflector, and is reflected as P and S waves, called SP and SS. Since the S wave has a strong amplitude this time, the SP and SS reflections are much stronger than those in the modelling experiment show in the last subsection.

Part of the point reflections goes upwards and reaches the surface. The order in which the reflections reach the surface is PP, PS, SP, and SS.

The effect of the PSP breaking away from the PSS is not obviously shown in this case, since the PS, PSP, and PSS waves are relatively weak. However, the effect of the SSP breaking away from the SSS is significant, as shown in the snapshots of time $0.64s$ and $0.72s$ (Figure 2.28o, 2.28p, 2.28q, and 2.28r).

Surface records are different from those of the surface centre source modelling, too. Figure 2.29 shows surface records of this modelling. The strong events are P waves, Rayleigh waves, PP, SP, PS, and SS reflections. The break-away of the SSP from the SSS can be observed from time $0.63s$ to $0.75s$ on the event of SS reflection.

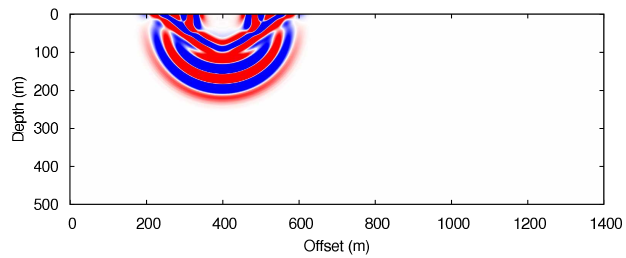

(a) Vertical component, 0.08s

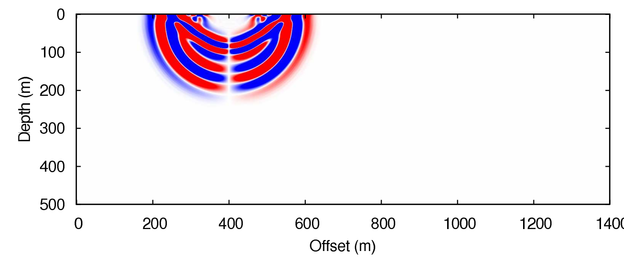

(b) Horizontal component, 0.08s

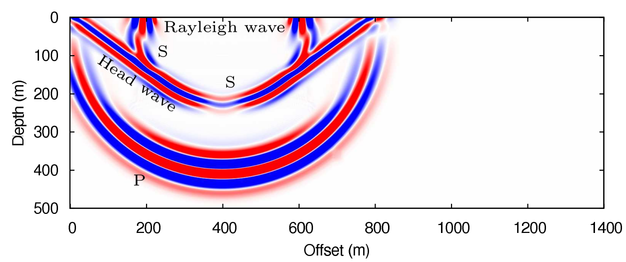

(c) Vertical component, 0.16s

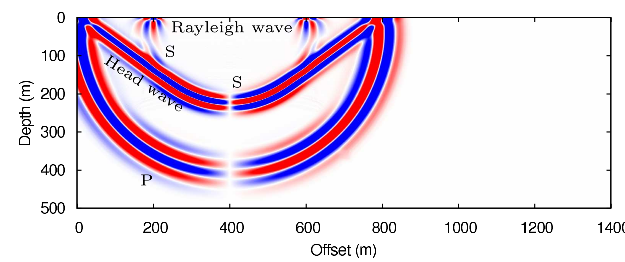

(d) Horizontal component, 0.16s

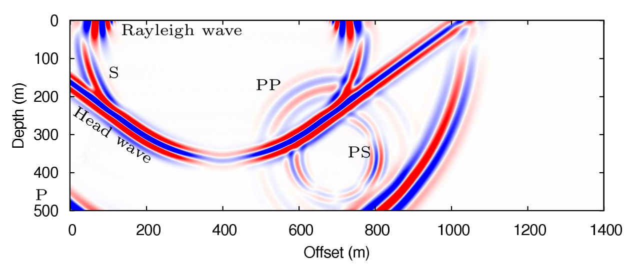

(e) Vertical component, 0.24s

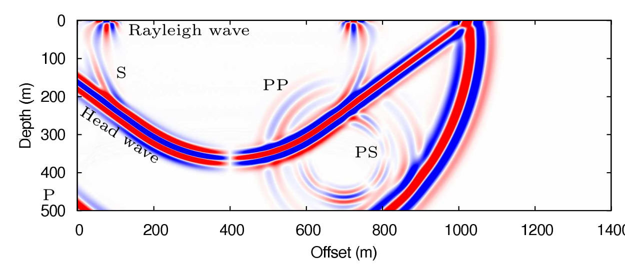

(f) Horizontal component, 0.24s

Figure 2.28: P-SV wave propagation with a horizontally far away surface source [to be continued].

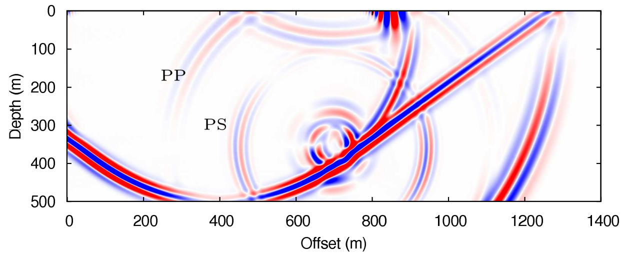

(g) Vertical component, 0.32s

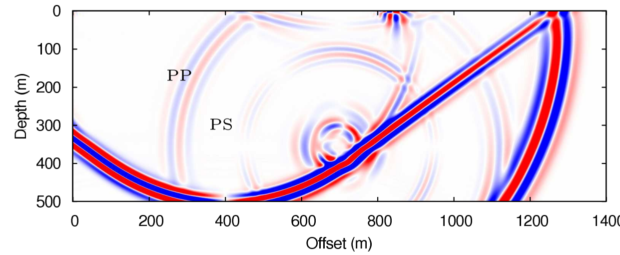

(h) Horizontal component, 0.32s

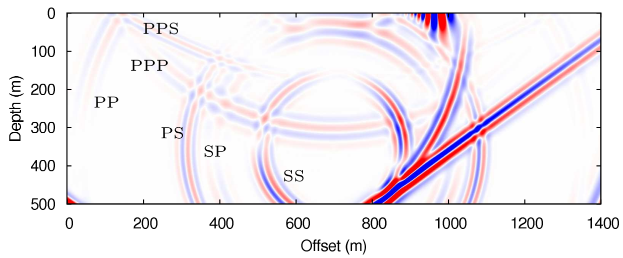

(i) Vertical component, 0.40s

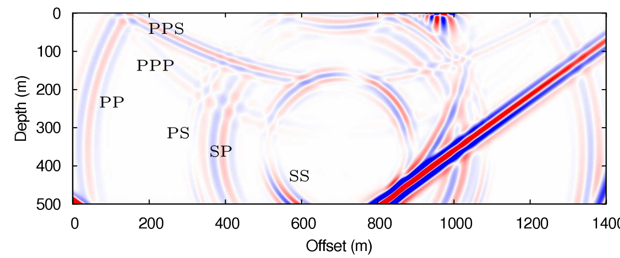

(j) Horizontal component, 0.40s

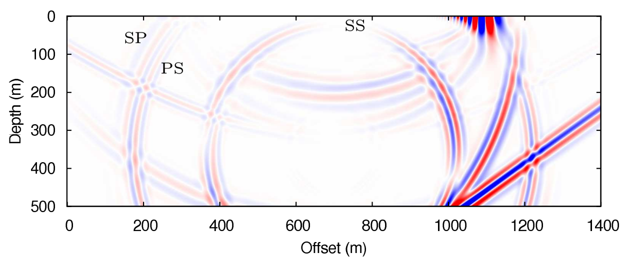

(k) Vertical component, 0.48s

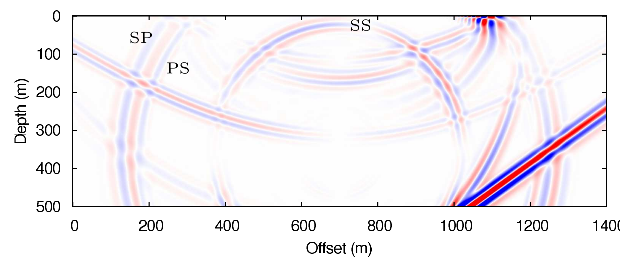

(l) Vertical component, 0.48s

Figure 2.28: [to be continued]

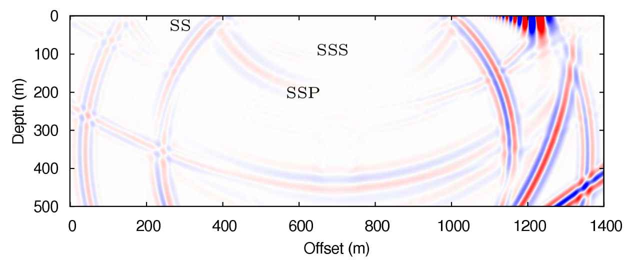

(m) Vertical component, 0.56s

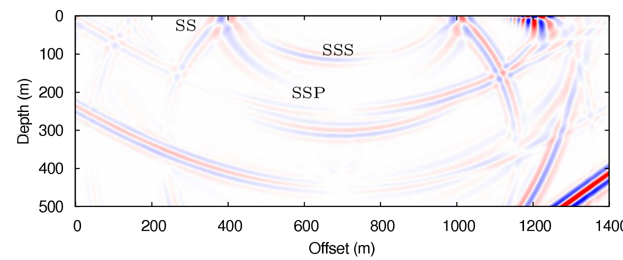

(n) Horizontal component, 0.56s

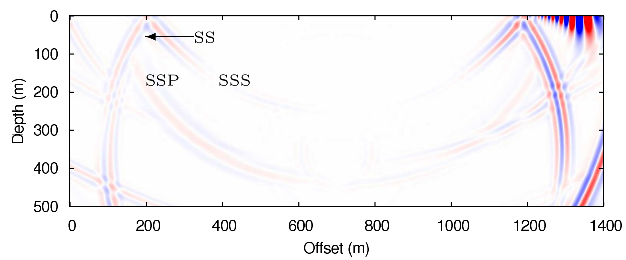

(o) Vertical component, 0.64s

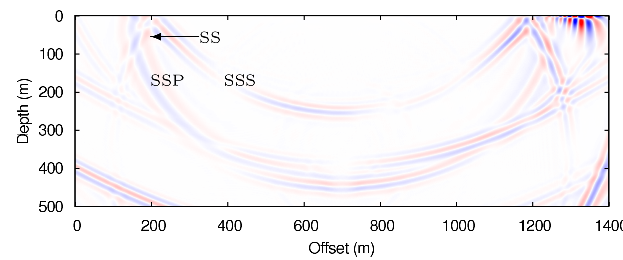

(p) Horizontal component, 0.64s

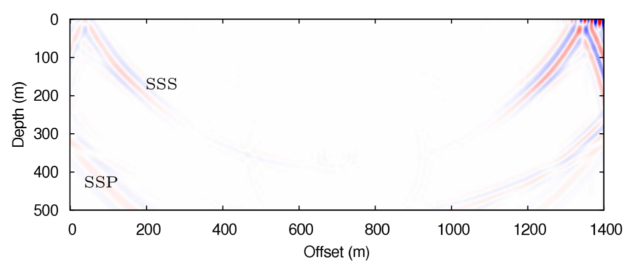

(q) Vertical component, 0.72s

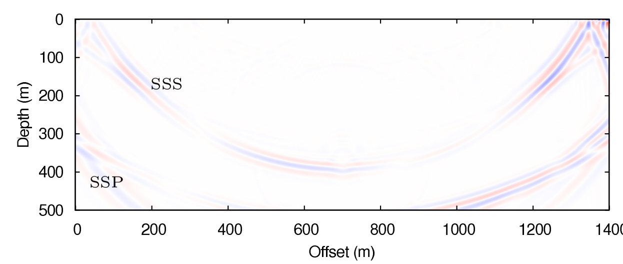

(r) Vertical component, 0.72s

Figure 2.28: [Continued]

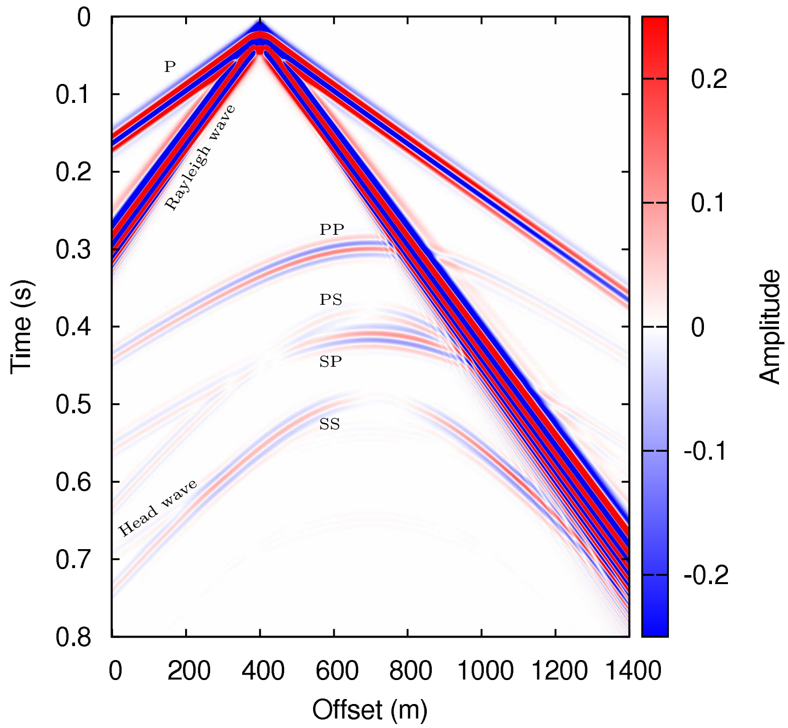

(a) Vertical component

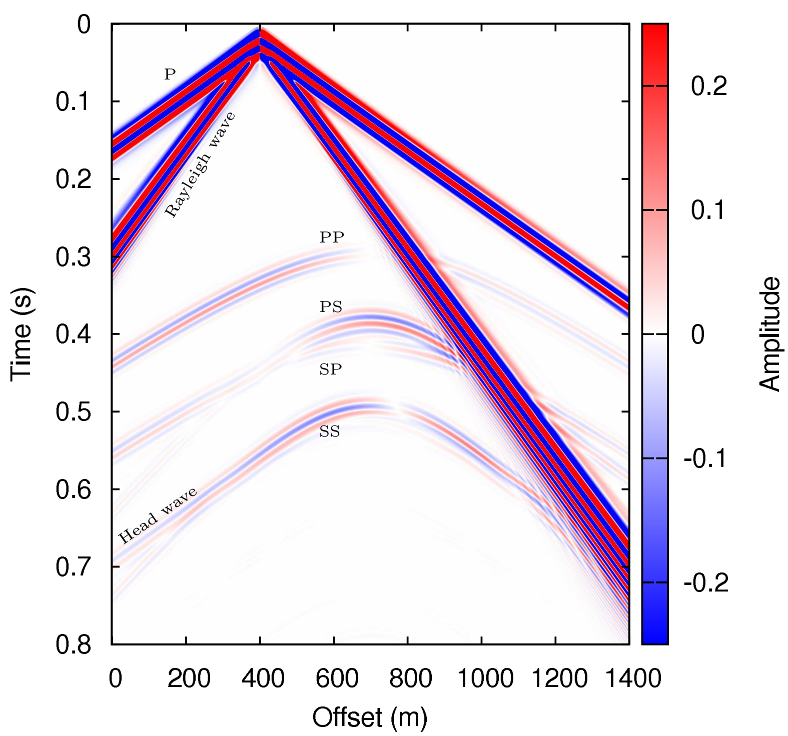

(b) Horizontal component

Figure 2.29: P-SV surface record with a horizontally far away surface source.

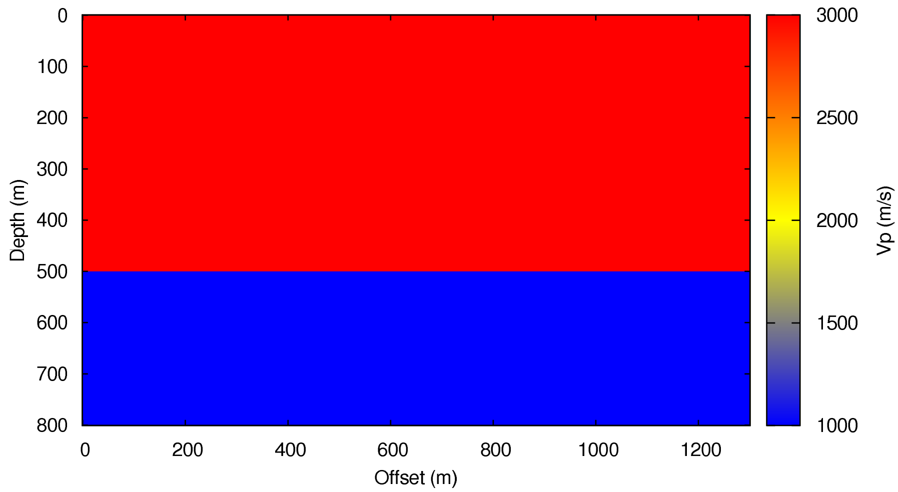

Figure 2.30: A two-layer subsurface model

Table 2.5: Wave velocities and densities in the model shown in Figure 2.30

Layer	P-wave vel.(m/s)	S-wave vel.(m/s)	Density (kg/m^3)
Surface layer	3000	1732.05	2290.89
Deeper layer	1000	577.35	1740.7

2.5.3 Reflection coefficients at non-normal incidence

Reflection and transmission coefficients of modelled 1D P wave are found to be very close to the theoretical values (subsection 2.3.2). This section studies the reflection coefficients of 2D P-SV case. The FD modelled results are compared to analytical results obtained from Zoeppritz equations.

Modelling on a two-layer subsurface model

A two-layer subsurface model was built, as shown in Figure 2.30. The media includes a flat geological interface separating two rock layers. The rock interface is at the depth of $500m$. The finite-difference node spacing in the model is $1m$. The wave velocities and densities are shown in Table 2.5.

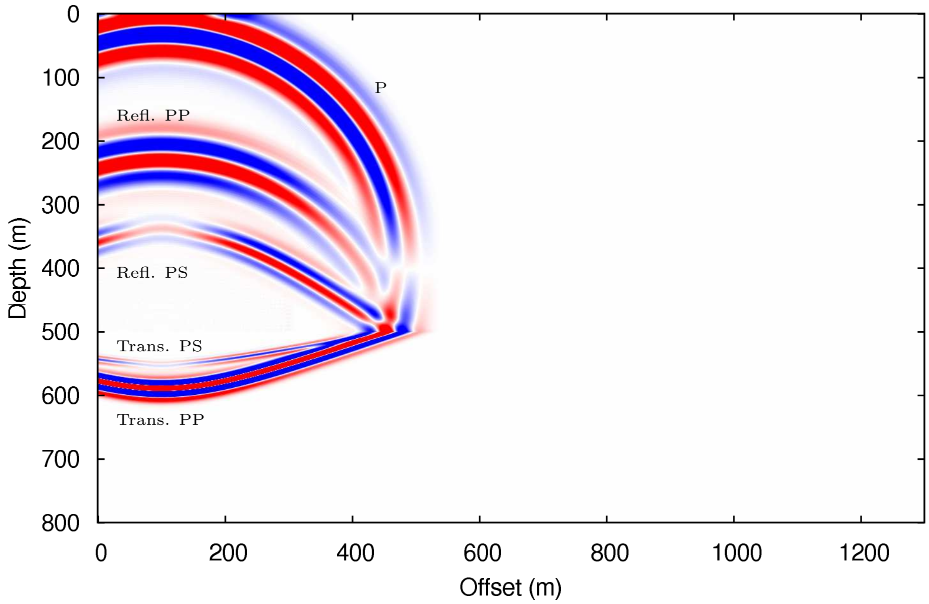

Figure 2.31: A snapshot of vertical component at time 1.5s. The subsurface model is shown in Figure 2.30.

A modelling experiment was done with a time step of $0.0001s$ and with a P-wave source at $(100m, 400m)$ and receivers at $400m$. Wavefields are generated and a vertical component snapshot is shown in Figure 2.31. The five wavefronts are a direct P wave generated from the energy source, a PP reflection and a PS reflection upon the rock interface at $500m$, a PS transmission and a PP transmission under the rock interface.

Seismic data recorded at the depth of $400m$ are shown in Figure 2.32. The recorded events include direct P-wave arrival, PP and PS reflections from the rock interface, and some other events. The studied reflection coefficients R_{PP} is based on the PP event.

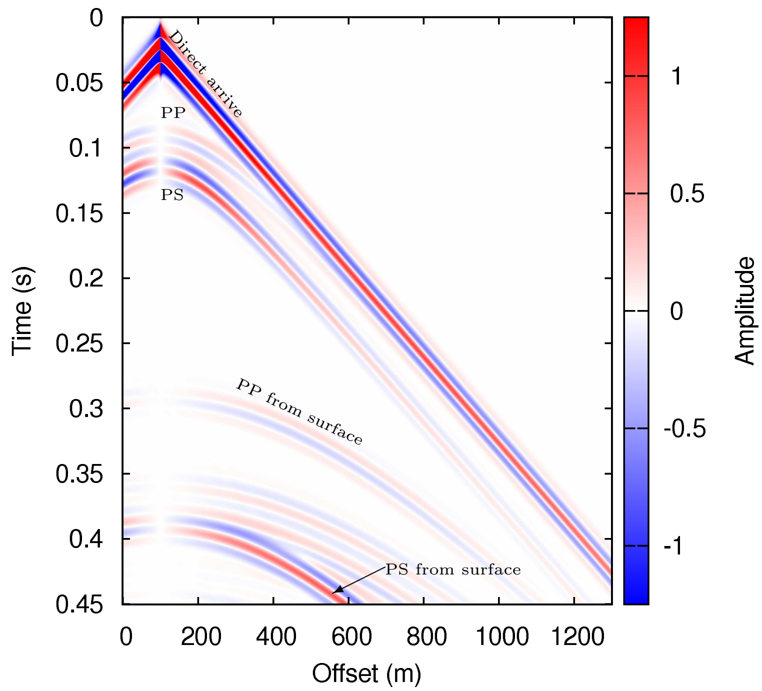

(a) Horizontal component

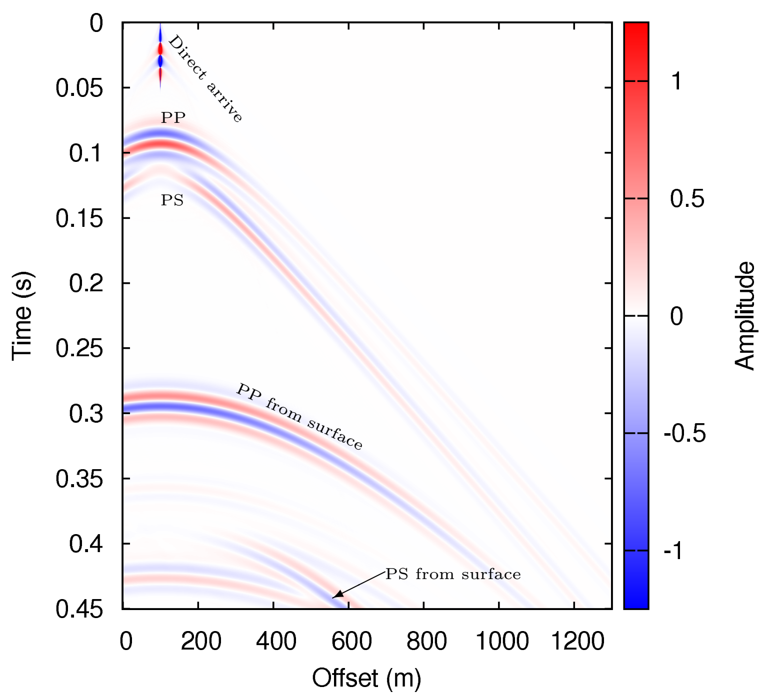

(b) Vertical component

Figure 2.32: Records received at a depth of 400m. The wavefield is generated from the subsurface model shown in Figure 2.30.

Measuring modelled PP reflection coefficients

There are two obstacles for one to study the rock interface PP reflection coefficients (R_{PP}) from the records shown in Figure 2.32. First, the PP event is merged into the direct P-wave arrival with large offsets. Second, from the wave energy source to the receivers, the amplitude attenuation includes both geometrical spreading and transmission losses.

To calculate the reflection coefficients R_{PP}, another subsurface model, referred to as the homegeneous model, was built. The demensions of the model are the same as the two-layer model shown Figure 2.30. However, the new model contains only a homogenerous medium, which has the same rock properties as the surface layer in the two-layer model.

Two wave modelling experiment is done using the homogeneous model.

The first experiment is designed to help remove the direct arrival in records from the two-layer model: a same acquisition geometry is employed, and only direct P wave and its surface reflections are generated. Thus, recorded events are the same P-wave arrival and its surface reflections as those obtained in the two-layer model experiment. Substraction of the homogeneous model records from the two-layer model records removes the direct arrival and its surface reflections in the two-layer-model records. Using this method, the PP event in the two-layer experiment is separated from the direct P-wave arrival. The records after removing the direct P-wave arrival are shown in Figure 2.33.

The second experiment on the homogeneous medium is done with an energy source at ($100m$, $600m$). Recorded data are the P-wave arrival and its surface PP reflection (Figure 2.34). Suppose A is a point on the event on a certain trace, and A$'$ is a

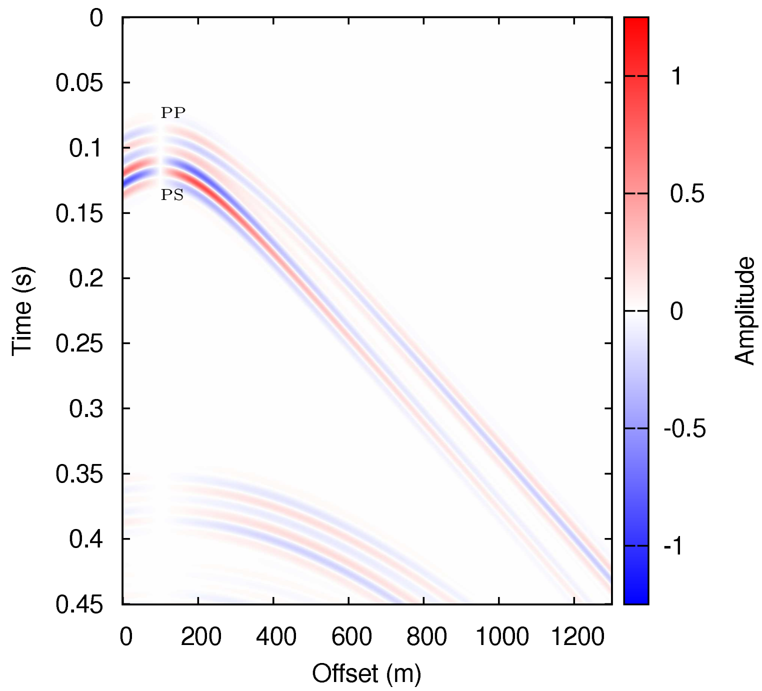

(a) Horizontal component

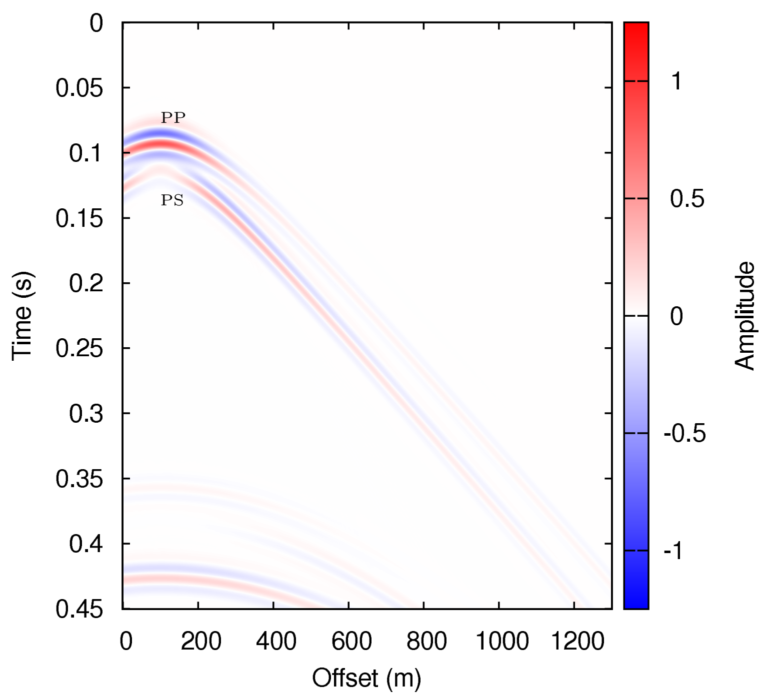

(b) Vertical component

Figure 2.33: Records resulted from removing direct arrival and its surface reflections in Figure 2.32.

corresponding point on the PP event on a corresponding trace from the two-layer model. Because the raypath length of A is the same as that of A′, geometrical spreading of A is the same as A′. Thus, the ratio of the amplitudes between A′ and A should be equal to the reflection coefficient on the raypath of A′.

In the calculation of reflection coefficients, two adjustments have to be done. First, the ratios are negative because of the change of wave propagation direction upon the rock interface. Second, one needs to find A′ as the local maximum in a trace according to the position of A (i.e., the time of A), since there is a slight position difference between A and A′, which is caused by the phase change accompanying with wave reflection. Calculated reflection coefficients are shown in Figure 2.35. The measurement of the amplitudes and the calculation of incident angle are limited to 85° because of the limited width of the subsurface model.

Modelled versus analytical reflection coefficients

Reflection and transmission of plane P-SV waves at non-normal incidence are governed by Zoepprize equations and the analytical solutions are given by Aki and Richards (2002, chap. 5). For the given rock interface shown in Figure 2.30 and Table 2.5, the analytical results are also plotted in Figure 2.35.

There are differences between the modelled and analytical reflection coefficients. There might be three causes of discrepancy: the seismic energy source, inaccuracy of the modelling method, and/or inaccuracy of the reflection coefficient measuring method. However, only the first one is discussed here.

A first guess is that the differences are mainly caused by the seismic energy sources: the modelling results are obtained with a circular source, while the analytical results are based on a plane wave source.

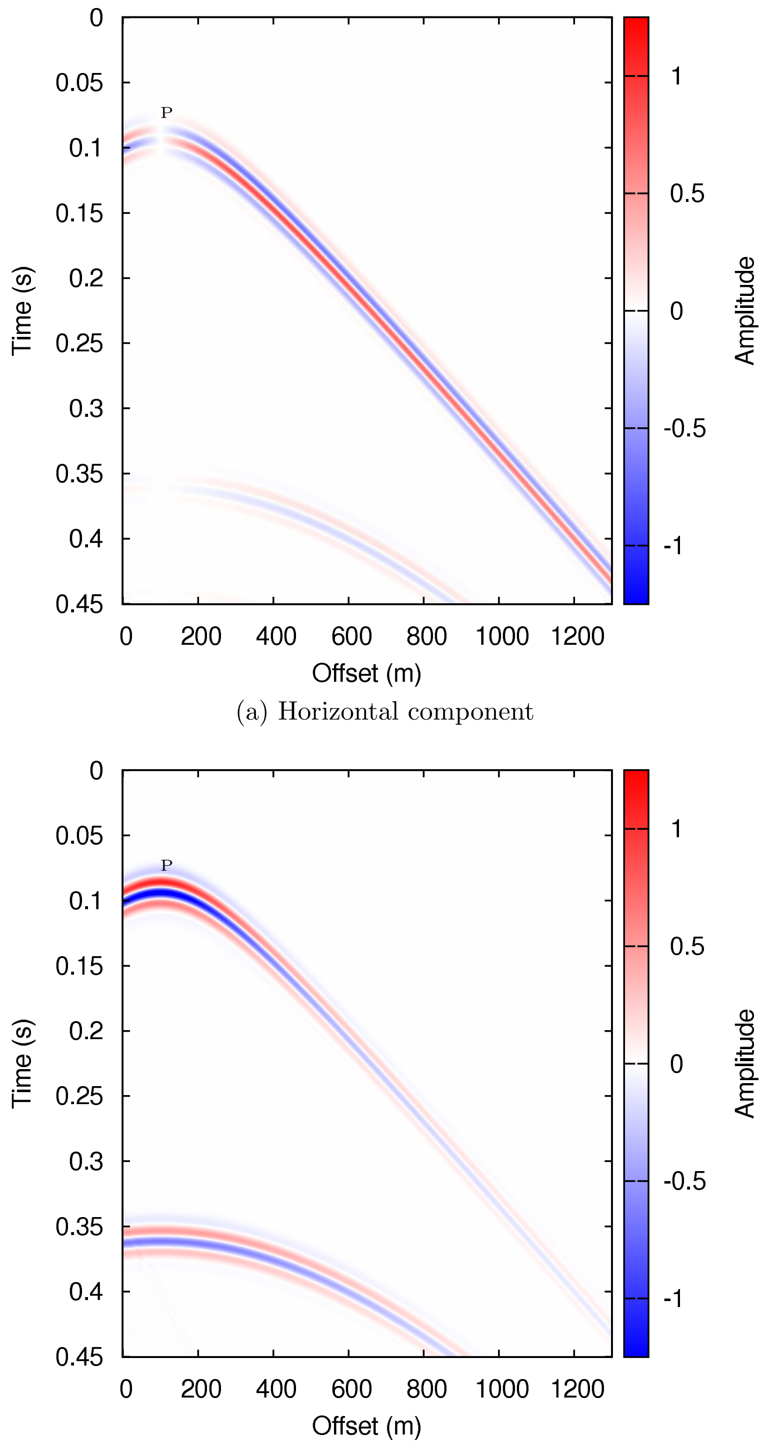

(a) Horizontal component

(b) Vertical component

Figure 2.34: Records at a depth of 400m, with the source at (100m, 600m) and a homogeneous medium subsurface model. The medium has the same rock properties as those of the surface layer in the two-layer model shown in Figure 2.30.

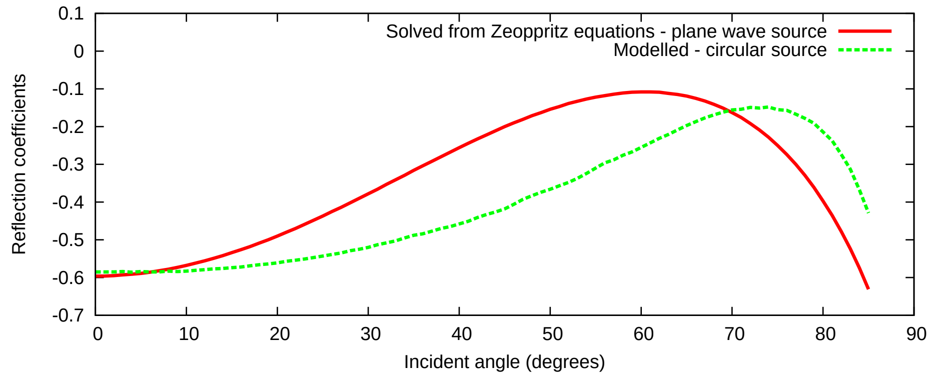

Figure 2.35: Reflection coefficients calculated from Zoeppritz equations versus those measured from modelling results.

If the discrepancy is due to circular waves, then it should become less if one increased the distance between the point envergy source and reflectors. This causes the incident wavefront to have a larger radius of curvature and hence be more locally planar.

In order to verify the guess about the source, another set of experiments are carried out. First, another two-layer subsurface model was built, as shown in Figure 2.36. The rock interface is at the depth of $800m$. The finite-difference node spacing in the model is $1m$. The wave velocities and densities are the same as shown in Table 2.5. Second, modelling and calculation on the larger two-layer model are done similar to those on the smaller model, but the energy source and receivers are put at a depth of $200m$. The result is plotted in Figure 2.37.

It can be found that the distance between the circular energy source and the reflector has very limited affections on the modelling result, although at small angles the large distance modelling agrees with Zoeppritz solution more.

Thus, it seems that the reflection coefficient discrepancy between the Zoeppritz

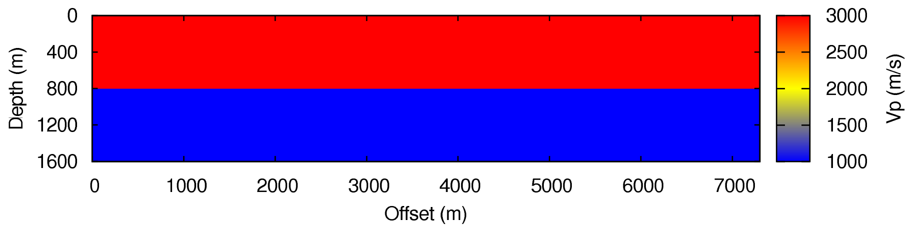

Figure 2.36: A two-layer subsurface model, larger than the one shown in Figure 2.30

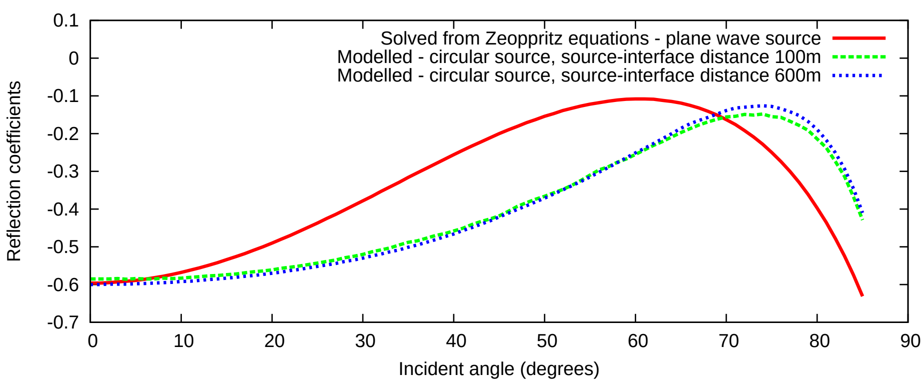

Figure 2.37: Reflection coefficients calculated from Zoeppritz equations versus those measured from modelling results.

solution and the finite-difference modelling result is mainly caused by inaccuracy of the modelling method.

2.6 3D wave modelling

2.6.1 Algorithm

Finite-difference implementation

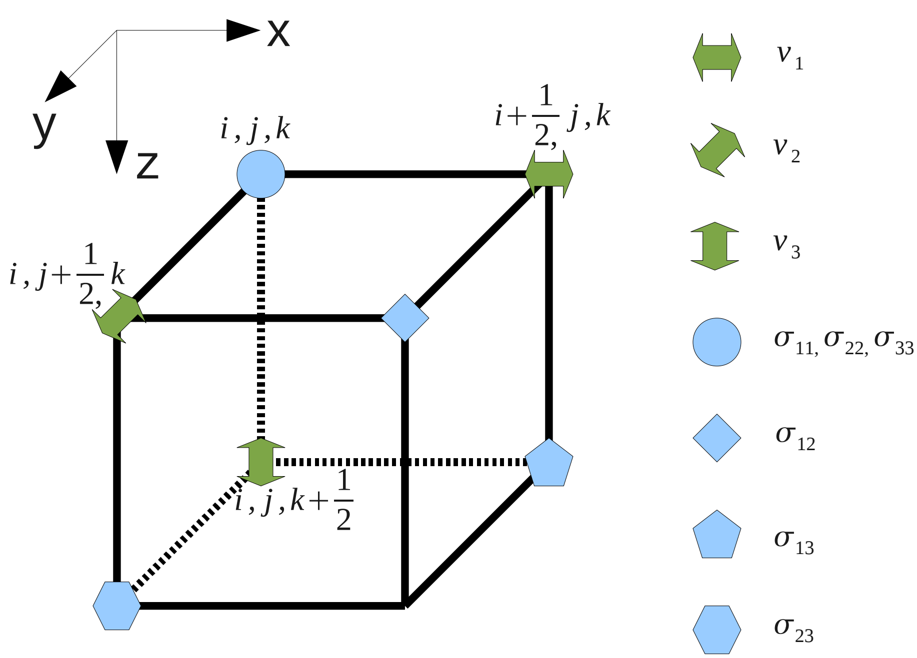

Figure 2.38: A staggered grid for 3D wave modelling.

If a same grid step h is used for x_1, x_2, and x_3 axes and Δt is used for the time step, a discrete form of the velocity-stress system of 3D waves is derived from displacement-stress-strain relations (2.8) as

$$\begin{aligned}
{v_1}_{i+1/2,j,k}^{n+1/2} &= {v_1}_{i+1/2,j,k}^{n-1/2} + \frac{\Delta t}{h\rho_{i+1/2,j,k}}({\sigma_{11}}_{i+1,j,k}^{n} - {\sigma_{11}}_{i,j,k}^{n} + {\sigma_{12}}_{i+1/2,j+1/2,k}^{n} \\
&\quad - {\sigma_{12}}_{i+1/2,j-1/2,k}^{n} + {\sigma_{13}}_{i+1/2,j,k+1/2}^{n} - {\sigma_{13}}_{i+1/2,j,k-1/2}^{n}) \qquad (2.59a) \\
{v_2}_{i,j+1/2,k}^{n+1/2} &= {v_2}_{i,j+1/2,k}^{n-1/2} + \frac{\Delta t}{h\rho_{i,j+1/2,k}}({\sigma_{12}}_{i+1/2,j+1/2,k}^{n} - {\sigma_{12}}_{i-1/2,j+1/2,k}^{n} \\
&\quad + {\sigma_{22}}_{i,j+1,k}^{n} - {\sigma_{22}}_{i,j,k}^{n} + {\sigma_{23}}_{i,j+1/2,k+1/2}^{n} - {\sigma_{23}}_{i,j+1/2,k-1/2}^{n}) \qquad (2.59b) \\
{v_3}_{i,j,k+1/2}^{n+1/2} &= {v_3}_{i,j,k+1/2}^{n-1/2} + \frac{\Delta t}{h\rho_{i,j,k+1/2}}({\sigma_{13}}_{i+1/2,j,k+1/2}^{n} - {\sigma_{13}}_{i-1/2,j,k+1/2}^{n} \\
&\quad + {\sigma_{23}}_{i,j+1/2,k+1/2}^{n} - {\sigma_{23}}_{i,j-1/2,k+1/2}^{n} + {\sigma_{33}}_{i,j,k+1}^{n} - {\sigma_{33}}_{i,j,k}^{n}) \qquad (2.59c) \\
{\sigma_{11}}_{i,j,k}^{n+1} &= {\sigma_{11}}_{i,j,k}^{n} + \frac{(\lambda+2\mu)_{i,j,k}\Delta t}{h}({v_1}_{i+1/2,j,k}^{n+1/2} - {v_1}_{i-1/2,j,k}^{n+1/2}) \\
&\quad + \frac{\lambda_{i,j,k}\Delta t}{h}({v_2}_{i,j+1/2,k}^{n+1/2} - {v_2}_{i,j-1/2,k}^{n+1/2} + {v_3}_{i,j,k+1/2}^{n+1/2} - {v_3}_{i,j,k-1/2}^{n+1/2}) \qquad (2.59d) \\
{\sigma_{22}}_{i,j,k}^{n+1} &= {\sigma_{22}}_{i,j,k}^{n} + \frac{(\lambda+2\mu)_{i,j,k}\Delta t}{h}({v_2}_{i,j+1/2,k}^{n+1/2} - {v_2}_{i,j-1/2,k}^{n+1/2}) \\
&\quad + \frac{\lambda_{i,j,k}\Delta t}{h}({v_1}_{i+1/2,j,k}^{n+1/2} - {v_1}_{i-1/2,j,k}^{n+1/2} + {v_3}_{i,j,k+1/2}^{n+1/2} - {v_3}_{i,j,k-1/2}^{n+1/2}) \qquad (2.59e) \\
{\sigma_{33}}_{i,j,k}^{n+1} &= {\sigma_{33}}_{i,j,k}^{n} + \frac{(\lambda+2\mu)_{i,j,k}\Delta t}{h}({v_3}_{i,j,k+1/2}^{n+1/2} - {v_3}_{i,j,k-1/2}^{n+1/2}) \\
&\quad + \frac{\lambda_{i,j,k}\Delta t}{h}({v_1}_{i+1/2,j,k}^{n+1/2} - {v_1}_{i-1/2,j,k}^{n+1/2} + {v_2}_{i,j+1/2,k}^{n+1/2} - {v_2}_{i,j-1/2,k}^{n+1/2}) \qquad (2.59f) \\
{\sigma_{12}}_{i+1/2,j+1/2,k}^{n+1} &= {\sigma_{12}}_{i+1/2,j+1/2,k}^{n} + \frac{\mu_{i+1/2,j+1/2,k}\Delta t}{h} \\
&\quad ({v_1}_{i+1/2,j+1,k}^{n+1/2} - {v_1}_{i+1/2,j,k}^{n+1/2} + {v_2}_{i+1,j+1/2,k}^{n+1/2} - {v_2}_{i,j+1/2,k}^{n+1/2}) \qquad (2.59g) \\
{\sigma_{13}}_{i+1/2,j,k+1/2}^{n+1} &= {\sigma_{13}}_{i+1/2,j,k+1/2}^{n} + \frac{\mu_{i+1/2,j,k+1/2}\Delta t}{h} \\
&\quad ({v_1}_{i+1/2,j,k+1}^{n+1/2} - {v_1}_{i+1/2,j,k}^{n+1/2} + {v_3}_{i+1,j,k+1/2}^{n+1/2} - {v_3}_{i,j,k+1/2}^{n+1/2}) \qquad (2.59h) \\
{\sigma_{23}}_{i,j+1/2,k+1/2}^{n+1} &= {\sigma_{23}}_{i,j+1/2,k+1/2}^{n} + \frac{\mu_{i,j+1/2,k+1/2}\Delta t}{h} \\
&\quad ({v_2}_{i,j+1/2,k+1}^{n+1/2} - {v_2}_{i,j+1/2,k}^{n+1/2} + {v_3}_{i,j+1,k+1/2}^{n+1/2} - {v_3}_{i,j,k+1/2}^{n+1/2}) \qquad (2.59i)
\end{aligned}$$

where i, j, and k are the indices for x_1, x_2, and x_3 discretization, and n is the index for time discretization. The corresponding staggered-grid mesh is shown in Figure 2.38.

Free-surface boundary

Free-surface boundary conditions defined by equations (2.11) can be rewritten as

$$\sigma_{13}\Big|_{x_3=0} \equiv 0, \tag{2.60a}$$

$$\sigma_{23}\Big|_{x_3=0} \equiv 0, \tag{2.60b}$$

$$\sigma_{33}\Big|_{x_3=0} \equiv 0. \tag{2.60c}$$

However, similar to the 2D P-SV case described in section 2.5.1, the above conditions can not be directly applied to the staggered-grid finite-difference scheme. The reason is that the shear stresses σ_{13} and σ_{23}, are not exactly positioned on the surface. Thus, a scheme, which is similar to the one in section 2.5.1, is developed to model the free surface. The difference is that the scheme is in 3D.

2.6.2 Modelling with a homogeneous medium

A homogeneous model is used to do 3C-3D wave modelling. The model is a $600m \times 600m \times 300m$ cuboid (Figure 2.39). The P- and S-wave velocities of the medium are $3000.00m/s$ and $1732.05m/s$, and the density is $2290.89kg/m^3$.

A P-wave seismic energy source is buried at a depth of $10m$ below the surface centre. The source is modelled by six zero-phase Ricker wavelets (Figure 2.40). A cross-section annotated by 'A' spans the surface centre and the source point.

If the P-wave seismic energy source is buried deep inside the model, pure P wave

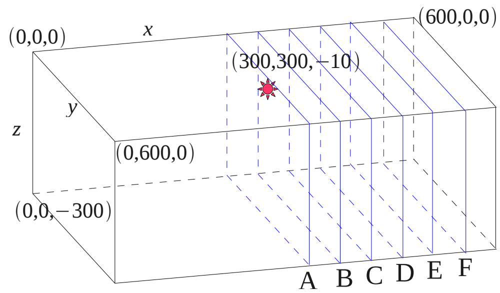

Figure 2.39: A 3D subsurface model geometry. A seismic energy source is 10 meters below the surface centre. The coordinate unit is meter. Snapshots of cross-section 'A' at different times are shown in Figure 2.41, and 3C-3D snapshots on cross-section 'A'-'E' at time 0.105s are shown in Figure 2.42.

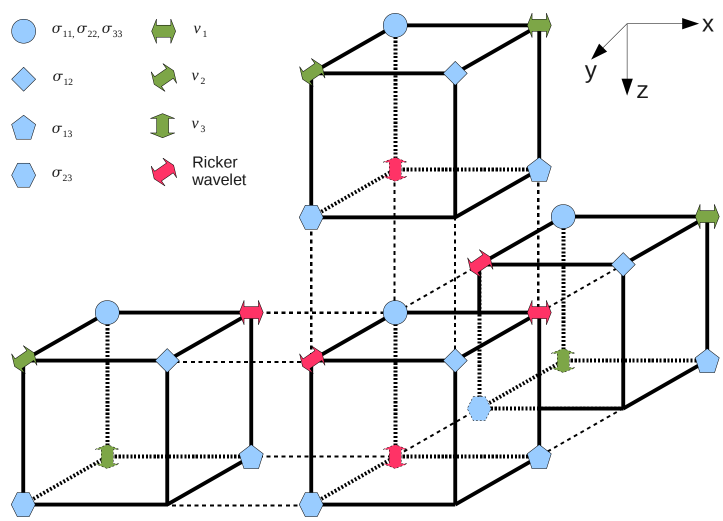

Figure 2.40: A seismic energy source scheme for 3D wave modelling.

is generated. This is similar to the 2D P-SV case described in earlier sections, except that in 3D modelling the wave front is a sphere, instead of a circle of 2D case. In fact, the seismic source for 2D P-SV modelling is regarded as a line source, with the line perpendicular to the model plane, while here the source is a point in 3D.

With the source buried at a shallow depth, both P and S waves are generated near the source, because of the free surface above the source. When the wave propagates away from the source point, head waves connecting the P and S waves are generated. Also, Rayleigh waves propagate on the 3D surface, with a circular ring wave front. Figure 2.41 and Figure 2.42 show the wave propagation in the 3D volume.

Figure 2.41 shows vertical component snapshots of generated waves in cross-section 'A' at three different times. All the waves, including P and S waves, downgoing head waves, and Rayleigh waves, appear as expected.

Amplitude of the waves decay when the waves propagate away. However, they decay at different rates: body waves, i.e., P and S waves and downgoing head waves, decay faster than the surface waves. In fact, theoretically, the body waves decay in the rate of distance, while the surface waves decay in the rate of square root of distance.

Waves travel at different velocities. P wave is the fastest. S waves and downgoing head waves travel at the same velocity, since the downgoing head waves are also S waves. Rayleigh waves are the slowest.

To interpret 3C-3D wave snapshots at time $0.105s$, as shown in Figure 2.42, one starts with the whole 3D picture of the wavefield. As mentioned before, there are P and S waves, downgoing head waves, and Rayleigh waves generated from the seismic energy source. P, S, and the downgoing head waves are body waves. The P wavefront

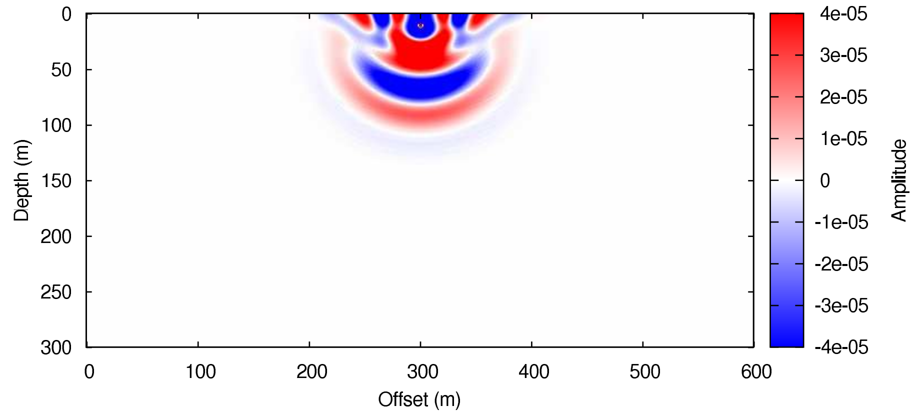

(a) Time 0.045s

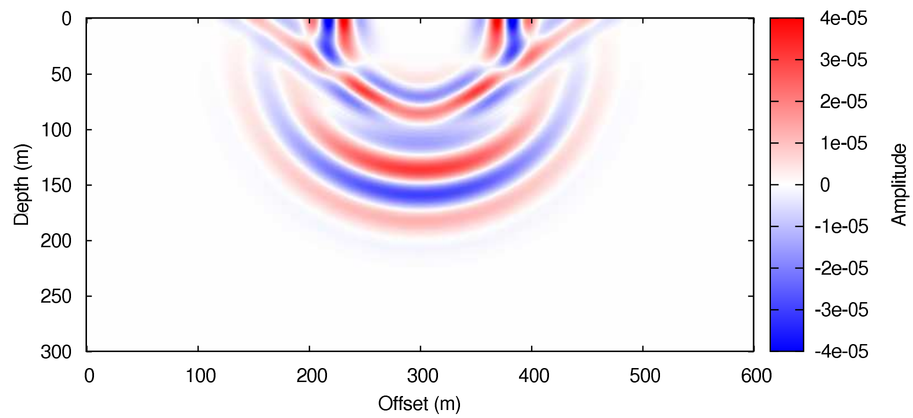

(b) Time 0.075s

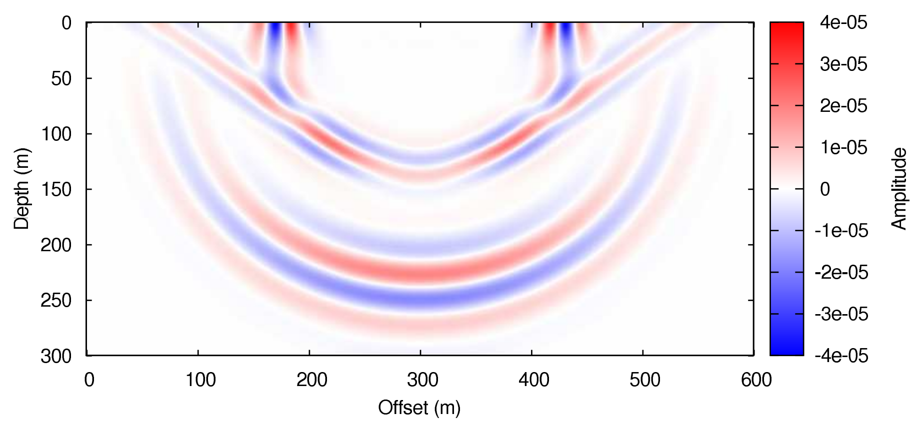

(c) Time 0.105s

Figure 2.41: Vertical component snapshots of the centre cross-section 'A' shown in Figure 2.39.

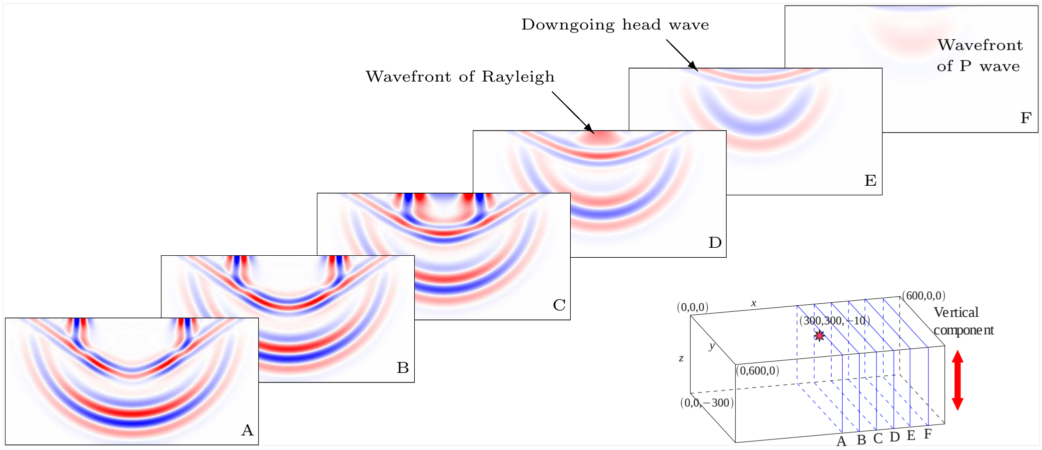

(a) Vertical component

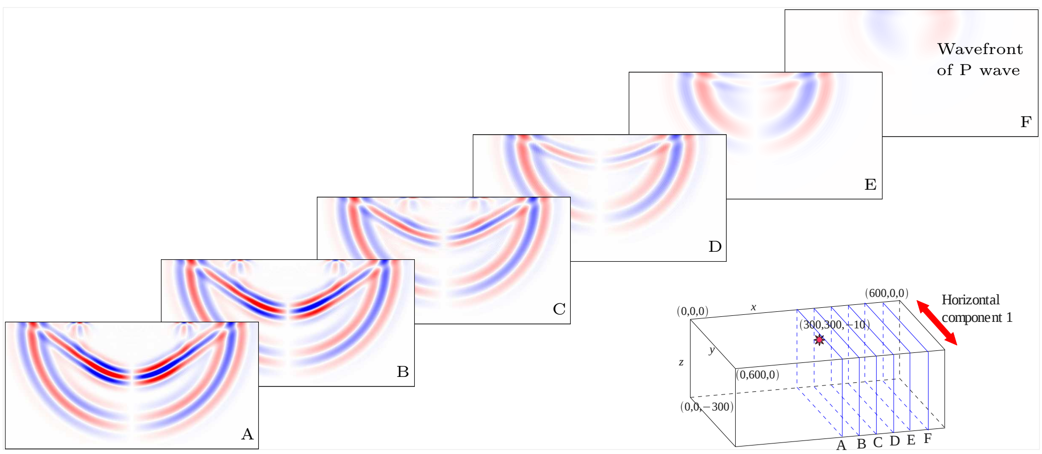

(b) Horizontal component 1

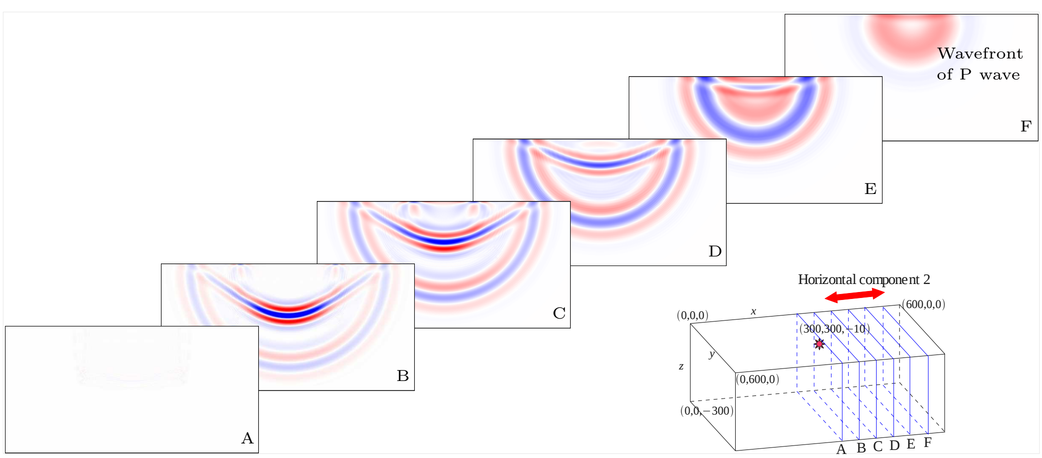

(c) Horizontal component 2

Figure 2.42: 3C-3D wave snapshots at time 0.105s.

is a hemisphere at the most outside of the wavefield, because it travels faster than any other waves. The S wavefront is another hemisphere, which stays inside. The downgoing head wave shapes as a funnel, connecting P and S waves. The head wave is an S wave, travelling at the S-wave velocity in the subsurface, showing an apparent velocity of the P wave on the surface. The Rayleigh wave is a circular ring, spreading on the surface at a velocity slower than the S-wave velocity. With the 3D picture in mind, it is easy to recognize them in Figure 2.42 even though sometimes they seem strange, such as the places annotated with 'wavefront of Rayleigh wave', 'downgoing head wave', and 'wavefront of P wave' in the figure.

A 'strange' phenomenon in the wavefield is cross-section 'A' of the horizontal component 2 (Figure 2.42c). There is no wave energy on this plot, i.e., there is no particle vibration perpendicular to this plane. However, this must be true in the physical world since it can be proven that there should be no particle vibrations perpendicular to this plane when the P-wave source wavefield is symmetric and the medium is isotropic.

It is proven as follows that there should be no particle vibrations perpendicular to the plane 'A'. Suppose a point P_0 is on cross-section 'A'. Another two points P_{-1} and P_1 are on the opposite side of P_0 adjacent to it, and they are on a line perpendicular to the plane 'A'. Cross-section 'A' is the plane of a point seismic source, and it becomes a plane of wavefield symmetry since the medium is isotropic homogeneous. If one uses $u_{P_{-1}}$, u_{P_0}, and u_{P_1} to denote the vibration component perpendicular to the plane 'A' at a time t, $u_{P_{-1}}$ and u_{P_1} must have the same amplitudes but with opposite directions. Since the displacement should be continuous at the three points, u_{P_0} must be zero.

2.7 Chapter summary

This chapter has discussed elastic wave modelling. Modelling algorithms are presented in details, and Modelling results are analyzed.

Modelling algorithms

Modelling methods for 1D, 2D, and 3D are discussed in great detail: equations about waves, finite-difference formulae based on staggered-grid schemes, seismic energy sources, free-surface boundary conditions, and subsurface model building. However, one important aspect of wave modelling, computational boundary problem, is left for the next chapter.

Modelling Results

Modelled results are analyzed to ensure the correctness of the modelling algorithms: modelled waves, such as surface waves, head waves, and body waves, are consistent with seismic theories.

Surface waves show up in the modelling of both SH-wave case and P-SV wave case, and in both 2D and 3D. It is confirmed that for the SH-wave case, surface waves do not exist in a homogeneous half-space, while they appear in a heterogeneous half-space. Rayleigh waves emerge in both homogeneous and heterogeneous half-spaces, and they travel at a slower velocity than body waves. Surface waves do not decay in 2D wave case, but they do in 3D case.

Body waves in the modelling results are more intensively interpreted. Modelled wave velocities and wave lengths are confirmed to be as designed. Wave amplitudes and phases are checked to study reflection and transmission coefficients. Geometrical spreading effects are checked in 1D, 2D, and 3D. The tuning effect is studied in the

SH-wave case.

Two head-wave cases are analyzed in the 2D P-SV wave modelling. The first case is the downgoing head waves that connecting the P and SV waves. They are actually plane SV waves. This case is commonly seen in the wave modelling literature. The second case is connected to the surface reflections of a upgoing S wave. This case is not seen in the literature, so it is analyzed in more details: the critical angle is calculated, the 'critical distance' is predicted and confirmed in the modelling results, and their appearances on surface records are pointed out.

2D P-SV case is discussed mostly using a point reflector model. The modelling is a preparation for Chapter 4.

Modelling of 3D waves is briefly presented for a 3D homogeneous half-space. However, the experiment reveals wave phenomena more rightfully than both 2D and 1D modelling.

In conclusion, the wave modelling results are faithful to elastic seismic theory. On one hand, this indicates the correctness of the modelling algorithms and their software implementation. On the other hand, conducting modelling and analyzing modelling results lead to better understanding of wave phenomena and seismic theories.

Chapter 3

Computational boundary

This chapter focuses on computational boundaries. First, rigid boundaries are mathematically analyzed and numerically modelled. Then, two most popular solutions to the computational boundary problem, absorbing boundary conditions proposed by Clayton and Engquist (1977) and a nonreflecting boundary condition proposed by Cerjan et al. (1985), are examined. Finally, a method of combining absorbing and nonreflecting boundary conditions is proposed.

3.1 Rigid boundary condition

A rigid boundary is "an idealized immovable interface" (Krebes, 2006). Waves striking it produce no motion of the boundary at all. A rigid boundary is convenient to implement in wave modelling by setting boundary displacements or particle velocities to be zeros. However, it results in very strong reflections. In fact, all the seismic energy will be reflected upon a rigid boundary. The reflections from such a boundary is artificial, and they mask the physical reflections inside the subsurface model. Thus, usually they are not wanted.

Modelling of rigid boundaries is useful, though. First, it exists in theory and represents a logical end point within the physical world. Second, it is important for comparison to the various computational boundary condition methods.

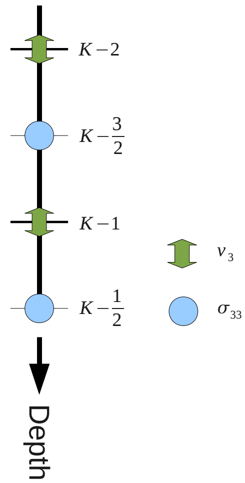

Figure 3.1: Bottom-most nodes in a staggered grid for 1D wave modelling.

3.1.1 1D P wave on a rigid boundary

For 1D P-wave modelling, the computational boundary is usually on the bottom. The bottom-most nodes of a 1D subsurface model are shown in Figure 3.1.

The rigid boundary condition for a 1D staggered-grid modelling is:

$$v_3\Big|_{K-1} = 0. \tag{3.1}$$

where the subscript $K-1$ indicates the bottom-most particle velocity node, since the index starts from 0.

With the above rigid boundary condition, stresses on the node $K-\frac{1}{2}$ is not calculated for all the time steps of the finite-difference approximation.

Theoretically, waves striking a rigid boundary will be completely reflected back with the same amplitudes and phases. 1D P wave numerical modelling results are consistent with the theory.

3.1.2 2D P-SV wave on a rigid boundary

After a mathematical analysis of a rigid boundary for 2D P-SV waves, a numerical implementation is designed. Numerical modelling results are shown to be consistent with the theoretical predictions.

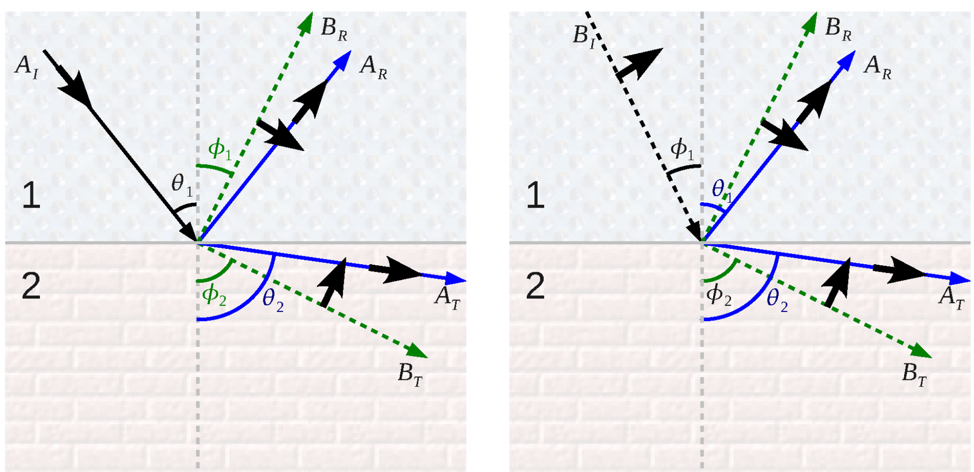

(a) P wave incident (b) SV wave incident

Figure 3.2: Reflection and transmission of incident P and SV waves. A and B, respectively, represent amplitudes of P and SV waves; Subscripts I, R, and T, respectively, represent incident, reflected, and transmitted waves; The boldface arrows define the virtual positive directions of particle motion (adapted from (Krebes, 2006)).

Rigid boundary in theory

Theoretically, what are the reflections off a rigid boundary ?

Consider the P-SV case shown in Figure 3.2. An incident P wave striking a boundary of media 1 and 2 produces reflected and transmitted P and SV waves. The boundary conditions are governed by the four Zoeppritz equations, which contain the following two equations for the horizontal and tangential components of displacement:

$$(A_I + A_R)sin\theta_1 + (B_I + B_R)cos\phi_1 = A_T sin\theta_2 + B_T cos\phi_2, \tag{3.2a}$$

$$(A_I - A_R)cos\theta_1 - (B_I - B_R)sin\phi_1 = A_T cos\theta_2 - B_T sin\phi_2. \tag{3.2b}$$

where A and B, respectively, represent the amplitudes of the P and SV waves; I, R, and T, the incident, reflected, and transmitted waves; and θ and ϕ, P and SV wave angles.

Waves striking a rigid boundary produce no motion on the boundary. Thus, the boundary conditions for the rigid boundary are: the normal and tangential components of displacement must be zero.

Consider a special case that there is only an incident P wave, i.e., there is no incident SV wave. There are no transmitted waves beyond the rigid boundary, so the boundary conditions in equation 3.2 can be re-written as

$$(A_I + A_R)sin\theta + B_R cos\phi = 0, \tag{3.3a}$$

$$(A_I - A_R)cos\theta - B_R sin\phi = 0. \tag{3.3b}$$

where media subscripts are dropped, since only medium 1 is involved.

Solving for the reflected P and SV waves yields

$$A_R = \frac{cos\theta cos\phi - sin\theta sin\phi}{cos\theta cos\phi + sin\theta sin\phi} A_I, \tag{3.4a}$$

$$B_R = -\frac{2sin\theta cos\theta}{cos\theta cos\phi + sin\theta sin\phi} A_I. \tag{3.4b}$$

Using the trigonometric addition formulas, one gets

$$A_R = \frac{cos(\theta + \phi)}{cos(\theta - \phi)} A_I, \tag{3.5a}$$

$$B_R = -\frac{sin2\theta}{cos(\theta - \phi)} A_I. \tag{3.5b}$$

These equations tell us that

1. The incident P wave energy is all reflected as P wave energy, i.e., there is no reflected SV wave, when an incident P wave travelling inside a solid medium strikes a rigid boundary with an incident angle equal to zero. There are both P and SV wave reflections when the incident angle is greater than zero.
2. For the vertical displacement, there is a polarity reversal for the P wave reflections compared to the incident P wave when the incident angle is such that $\theta + \phi$ is less than 90°. This is determined by not only the reflection coefficient $R_{PP} = A_R/A_I$ given by equation (3.5a), but also by the polarity vector (the boldface arrow in Figure 3.2). The amplitude of the reflected P wave becomes weaker when the incident angle becomes greater, until the reflected P wave disappears when the incident angle is such that $\theta + \phi$ is equal to 90°. Denoting the unique P-wave incident angle and S-wave reflection angle as θ_{UN} and ϕ_{UN}, by applying Snells law, these angles can be decided as

$$\theta_{UN} = \arctan(\frac{v_P}{v_S}), \tag{3.6a}$$

$$\phi_{UN} = \arctan(\frac{v_S}{v_P}). \tag{3.6b}$$

When the incident angle is even greater such that $\theta + \phi$ is greater than 90°, the reflected P wave appears again, but there is no polarity reversal compared to the incident P wave.

3. For the horizontal component of the reflected P wave, similar conclusions can be drawn, but the polarities are different. When the incident angle of the incident P wave is small enough, there will be no polarity reversal for the reflected P wave, compared to the incident P wave. Then there will be a polarity change in the reflected P wave when the incident angle reaches θ_{UN}.

4. There is no reflected SV wave when the incident P wave is vertically incident upon a rigid boundary. The reflected SV wave appears when the incident angle is greater than zero.

The interpretations above can be used to clarify the validity of an algorithm of rigid boundary conditions in the numerical wave modelling.

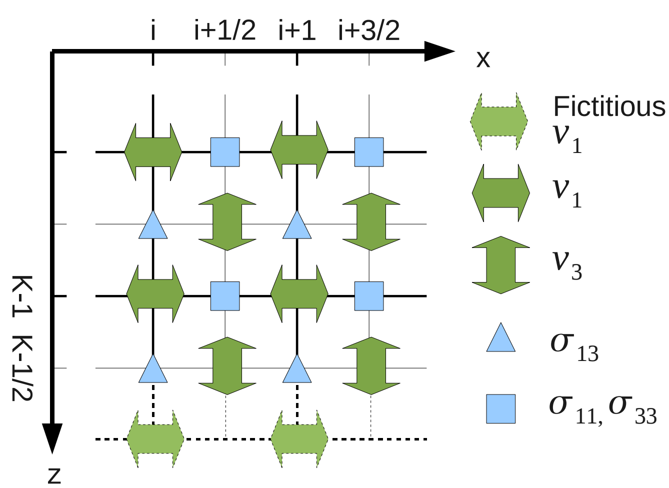

Figure 3.3: Rigid boundary conditions for a 2D P-SV staggered grid.

Rigid boundary in a staggered grid

For a staggered-grid scheme with velocity / stress and time splitting, shown in 2.20, the indices of the lines of horizontal particle velocity nodes are from 0 to $K-1$ for the horizontal particle velocities, and from 1/2 to $K-1/2$ for the vertical particle velocity nodes.

The natural assumption for the rigid boundary conditions is to set the boundary particle velocities to zero, i.e., set the values on the nodes on line $K-1$ and $K-1/2$ in Figure 3.3 to zero, but this turns out to be false. This conclusion is drawn from the fact that there are only P wave reflections off the boundary resulting in the numerical modelling experiment. Why does this implementation of rigid boundary conditions fail? The reason is that this method does not guarantee the horizontal particle velocities on the boundary (line $K-1/2$) to be zero.

Taking the line $K-1/2$ as the rigid boundary, in addition to the values of vertical particle velocities on this line being set to zero, one should also make sure that the horizontal particle velocities on this line equal to zero although there are no real numerical nodes on this line. If a virtual line of nodes is put on the line K, and the values on the virtual line are set anti-symmetric to those on the line $K-1$, i.e.,

$$v_1\Big|_K = -v_1\Big|_{K-1}, \tag{3.7a}$$

$$v_3\Big|_{K-1/2} = 0, \tag{3.7b}$$

then, the values of v_1 on the boundary line $K-1/2$ would be guaranteed to be zero by the central finite difference:

$$v_1\Big|_{K-1/2} = \frac{1}{2}(v_1\Big|_K + v_1\Big|_{K-1}) = 0. \tag{3.8}$$

Numerical modelling experiment

A 2D subsurface model is built to check the algorithm. The subsurface is 5000 meters in length and 1000 meters in depth. It is a homogeneous medium. The space steps on both horizontal and vertical directions are the same: $1.25m$. The P wave velocity is $3000m/s$ and the density is estimated by Gardner$'$s relationship. Then the S wave velocity is calculated to be $1732m/s$ by assuming the Poisson$'$s ratio to be 0.25. After the velocity and density parameters are decided, the Lamé coefficients are calculated and then used with the density data in the numerical modelling.

An explosive source is placed at the centre of the surface. The source consists of four zero phase Ricker wavelets with peak frequency equal to $40Hz$.

The time step of modelling is $0.00016s$. The number of total time steps is 5500, which makes the total time of modelling to be $0.88s$.

Modelling snapshots of the centre shot are shown in Figure 3.4 and 3.5. The first group of snapshots show the vertical component and the second ones show the horizontal component.They are shown in the time order.

In the snapshots of time $0.288s$, a P wave, an SV wave, and down-going header waves are traveling outwards from the seismic source, which is at the surface centre. On the surface, Rayleigh waves, which are slower than the SV wave, are also observed.

In the snapshots of time $0.4s$, the P wave strikes the bottom boundary, and reflections are produced although the reflections are not clearly distinguishable.

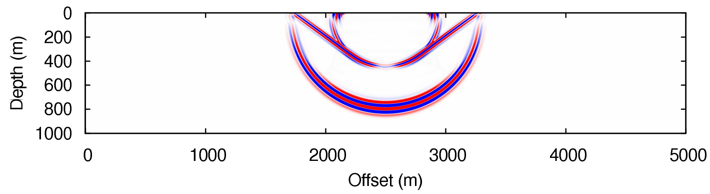

(a) 0.288s

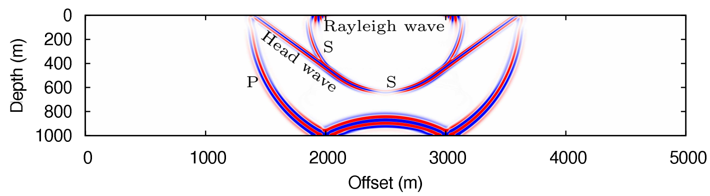

(b) 0.400s

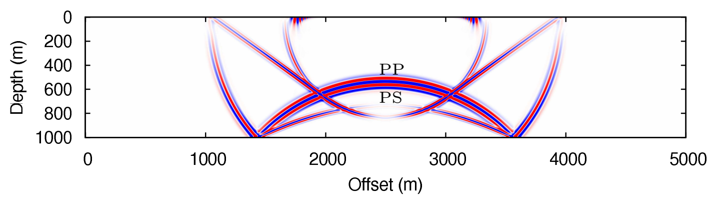

(c) 0.512s

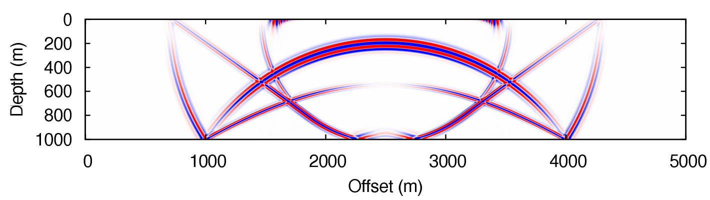

(d) 0.624s

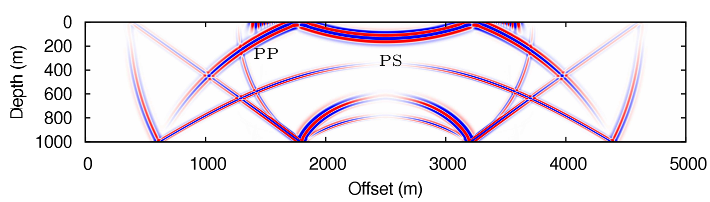

(e) 0.736s

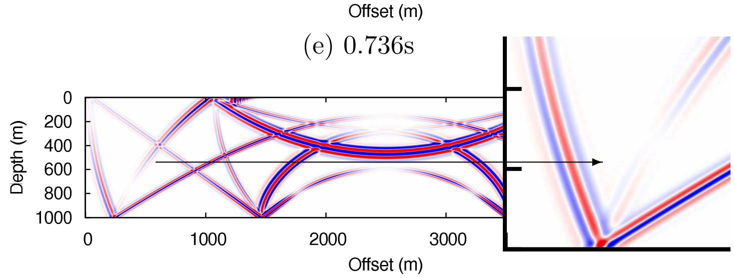

(f) 0.848s

Figure 3.4: P-SV wave upon a rigid boundary - vertical component.

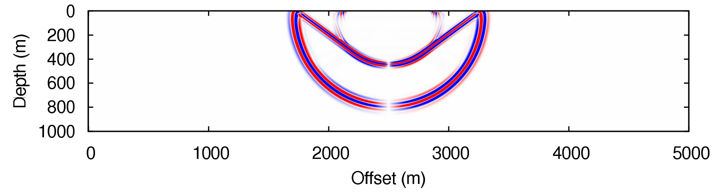

(a) 0.288s

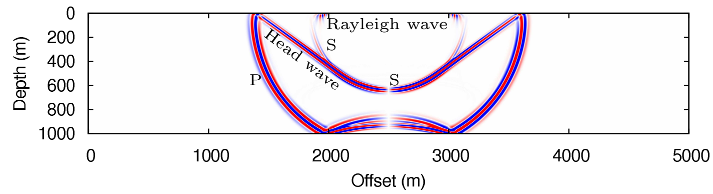

(b) 0.400s

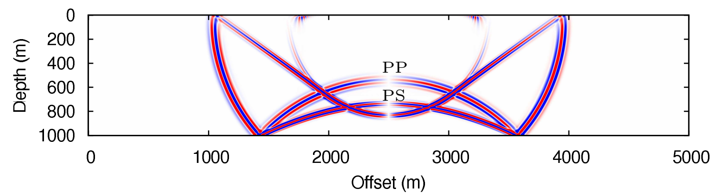

(c) 0.512s

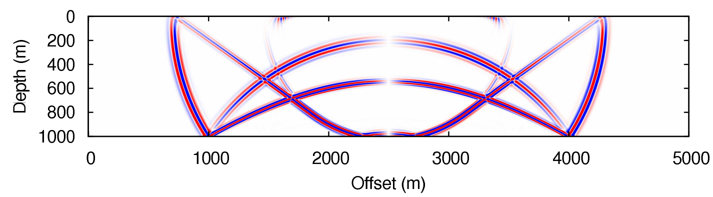

(d) 0.624s

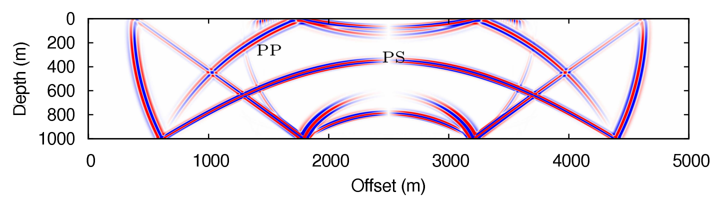

(e) 0.734s

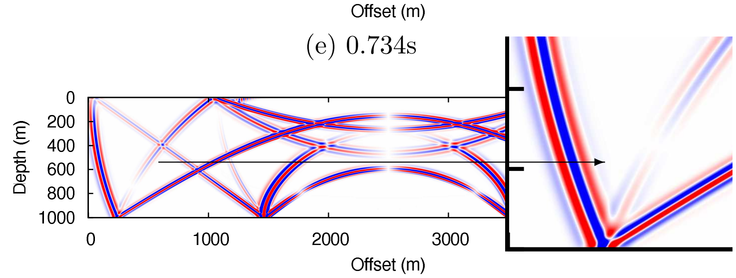

(f) 0.848s

Figure 3.5: P-SV wave upon a rigid boundary - horizontal component.

At times $0.512s$ and $0.624s$ the reflected P and SV waves are clearly distinguishable. The polarity reversal of the vertical component of the reflected P wave, compared to the incident P wave, can be observed. With the incident angles of the P wave on the bottom boundary becoming greater and greater, the P wave reflection becomes weaker and weaker. Spherical spreading is one cause of the amplitude attenuation, but the main cause is the incident angle change.

At time $0.736s$, the P wave reflected off the bottom boundary becomes very weak and seems to have disappeared. In fact, om this specific medium P- and S- wave velocities are, respectively, $3000m/s$ and $1732m/s$. According to equations 3.6, when the incident angle θ is equal to $60°$, the PS reflection angle ϕ is $30°$. In turn, $(\theta + \phi)$ is equal to $90°$. Thus, the amplitude of the reflected P wave is zero when the incident angle θ is equal to $60°$ in this specific medium.

At time $0.848s$, the P wave reflection has reappeared with a reversed polarity. Thus, two different polarities are observable on the same wave front of the P wave reflection.

Hence, one can conclude that the above observations accurately match the mathematical derivations and qualitative interpretations.

3.2 Absorbing boundary conditions

Absorbing boundary conditions proposed by Clayton and Engquist (1977) are examined in both 1D and 2D.

3.2.1 1D P-wave absorbing boundary conditions

Similar to the 2D absorbing boundary condition for a non-staggered grid finite-difference scheme (Clayton and Engquist, 1977), one can derive 1D absorbing boundary condition for a staggered-grid finite-difference system.

One-dimensional P-wave wave equation is

$$\frac{\partial^2 v_3}{\partial t^2} = v_P^2 \frac{\partial^2 v_3}{\partial x_3^2}, \tag{3.9}$$

where v_3 is the vertical displacement, and v_P is P-wave velocity in an isotropic homogeneous medium. Using complex exponential to describe harmonic waves, one gets the solution of the 1D wave equation

$$v_3 = Ae^{i[\kappa_3(x_3 - v_P t)]} = Ae^{i(\kappa_3 x_3 - \omega t)}, \tag{3.10}$$

where A is the amplitude, κ_3 is the circular wavenumber in the direction of x_3, ω is the circular frequency.

The first and the second partial derivatives of displacement with respect to time and space could be derived as

$$\frac{\partial v_3}{\partial t} = -i\omega A e^{i(\kappa_3 x_3 - \omega t)} = -i\omega u_3, \tag{3.11a}$$
$$\frac{\partial^2 v_3}{\partial t^2} = -\omega^2 u_3, \tag{3.11b}$$
$$\frac{\partial v_3}{\partial x_3} = i\kappa_3 u_3, \tag{3.11c}$$
$$\frac{\partial^2 v_3}{\partial x_3^2} = -\kappa_3^2 u_3. \tag{3.11d}$$

Substituting the second derivatives into the wave equation, one obtains the dispersion relation

$$\frac{\omega^2}{v_P^2} = \kappa_3^2. \tag{3.12}$$

Thus,

$$\kappa_3 = \pm\frac{\omega}{v_P}, \tag{3.13}$$

where the plus sign equation describes a plane wave travelling in the $+z$ direction, while the minus sign equation describes a plane wave travelling in the $-z$ direction.

From the first partial derivatives, one gets the following equations

$$\omega = -\frac{\frac{\partial v_3}{\partial t}}{i v_3}, \tag{3.14a}$$

$$\kappa_3 = \frac{\frac{\partial v_3}{\partial x_3}}{i v_3}. \tag{3.14b}$$

Submitting these two equations into $\kappa_3 = \frac{\omega}{v_P}$, one obtains the absorbing boundary condition for the bottom boundary as

$$\frac{\partial v_3}{\partial x_3} = -\frac{1}{v_P}\frac{\partial v_3}{\partial t}. \tag{3.15}$$

Suppose the 1D model has totally K spatial nodes, coded from 0 to $K-1$, for particle displacement. Using one-sided differences to approximate the absorbing boundary condition on this node, one gets:

$$\frac{v3_{K-1}^{n+1} - v3_{K-1}^{n}}{\Delta t} = -v_{PK-3/2}\frac{v3_{K-1}^{n} - v3_{K-2}^{n}}{h}. \tag{3.16}$$

That is,

$$v3_{K-1}^{n+1} = v3_{K-1}^{n} - \frac{v_{PK-3/2}\Delta t}{h\Delta t}(v3_{K-1}^{n} - v3_{K-2}^{n}) \tag{3.17a}$$

$$= (1 - \frac{v_{PK-3/2}\Delta t}{h\Delta t})v3_{K-1}^{n} + \frac{v_{PK-3/2}\Delta t}{h}v3_{K-2}^{n}. \tag{3.17b}$$

Modelled absorbing boundary

By checking the snapshots at time $0.2625s$ (Figure 2.6k) and at time $0.2875s$ (Figure 2.6l), it can be observed that the absorbing boundary works very well: there are almost no reflections.

In fact, the modelled data show that the boundary reflections are very weak comparing to the incident wave. The peak amplitude of the boundary reflections at time $0.2875s$ is -1.32825 at depth $911m$. This is about $\frac{1}{122}$ of the incident peak amplitude shown in Table 2.1, i.e., the reflection coefficient upon the absorbing boundary is about $\frac{1}{122}$. This is observed in Figure 3.6, which contains both an enlarged color plot of Figure 2.6l and its wiggle plot.

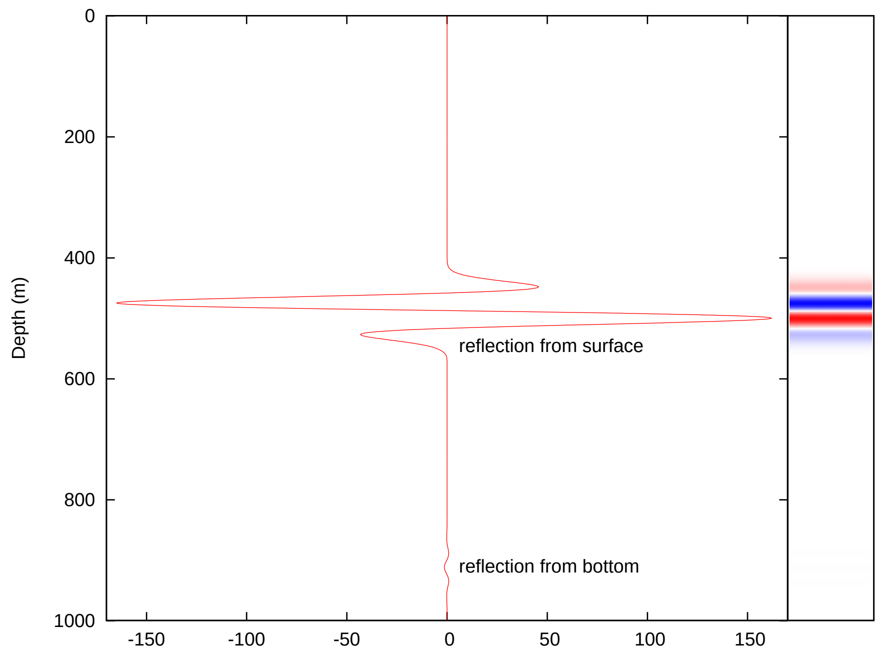

Figure 3.6: Reflection from an absorbing bottom boundary - enlarged Figure 2.6l and its wiggle plot.

3.2.2 P-SV wave absorbing boundary conditions

Numerical implementations

The absorbing boundary conditions A1 (Clayton and Engquist, 1977) for the bottom boundary of a 2D elastic subsurface model can be written as

$$\frac{\partial v_1}{\partial x_3} + \frac{1}{\beta}\frac{\partial v_1}{\partial t} = 0, \tag{3.18a}$$
$$\frac{\partial v_3}{\partial x_3} + \frac{1}{\alpha}\frac{\partial v_1}{\partial t} = 0, \tag{3.18b}$$

where v_1 and v_3 are, respectively, the horizontal and vertical particle velocity; α and β are, respectively, P-wave and S-wave velocity.

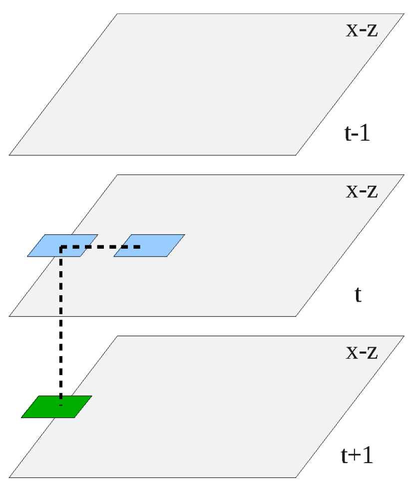

Figure 3.7: Absorbing boundary conditions: a solution to the problem shown in Figure 1.4b.

Using backward difference operator with respect to x_3 and forward difference operator with respect to time t, one can write system 3.2.2 in the staggered-grid scheme as

$$\frac{{v_1}_{i,K-1}^{n-1/2} - {v_1}_{i,K-2}^{n-1/2}}{h} + \frac{1}{\beta}\frac{{v_1}_{i,K-1}^{n+1/2} - {v_1}_{i,K-1}^{n-1/2}}{\Delta t} = 0, \tag{3.19a}$$

$$\frac{{v_3}_{i+1/2,K-1/2}^{n-1/2} - {v_3}_{i+1/2,K-3/2}^{n-1/2}}{h} + \frac{1}{\alpha}\frac{{v_3}_{i+1/2,K-1/2}^{n+1/2} - {v_1}_{i+1/2,K-1/2}^{n-1/2}}{\Delta t} = 0, \tag{3.19b}$$

where (i, k) is the space node index, n is the time node index. From the formulae, particle velocities on the boundary ${v_1}_{i,K-1}^{n+1/2}$ and ${v_3}_{i+1/2,K-1/2}^{n+1/2}$ are calculated from the data at time $n-1/2$. The data used at time $n-1/2$ are on the last two lines of nodes. Figure 3.7 sketches the approximation. This is a solution to the problem shown in Figure 1.4b.

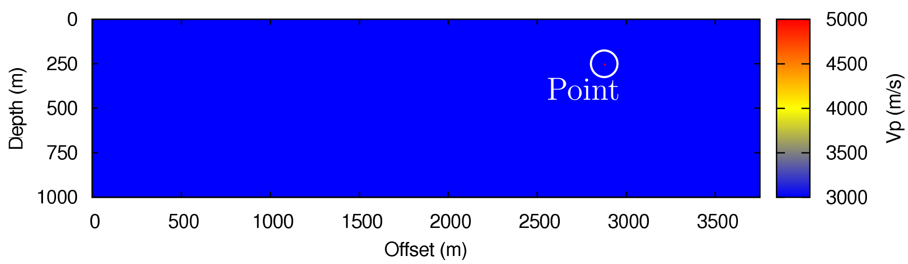

Figure 3.8: A point reflector subsurface model for boundary condition modelling. The dimension of the point reflector is 10m by 10m.

A point reflector subsurface model

In order to check different boundary conditions, another 2D subsurface model is built. The model contains a point reflector in a homogeneous medium in x_1-x_3 plane. Figure 3.8 shows its geometry with P-wave velocities. The subsurface is 3750m wide and 1000m high. With a spatial step of 1.25m, there are 3000 nodes in offset and 800 nodes in depth. The point reflector is a square with side length of 10m, positioned at offset from 2300m to 2310m, and at depth from 250m to 260m. The point reflector will generate physical reflections in wave modelling, and the reflections are compared to computational boundary reflections.

The rock properties of the point reflector and its surrounding rock are the same as in Table 2.4.

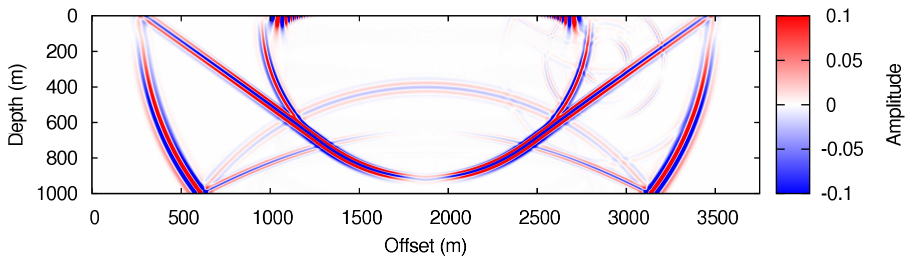

(a) Vertical component

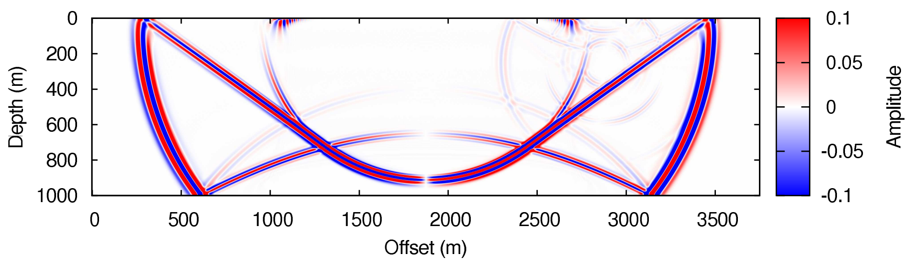

(b) Horizontal component

Figure 3.9: Modelling results using absorbing boundary conditions.

Modelling results using absorbing boundary conditions

Modelling is done by using a time step of 0.00016s and a total steps of 3500. Thus, the total modelling time is 0.56s.

Figure 3.9 shows the resulting wavefield, with two components. In addition to the source waves, P and S waves and Rayleigh waves, there are two sets of reflections. One is physical reflections from the point reflector and the free surface, and the other one is artificial reflections from the bottom boundary. The physical reflections include PP and PS reflections generated by the incident P wave, SP reflection generated by the down-going head wave, and surface reflections of PP and PS waves. The artificial reflections PP and PS are generated from the incident P wave. Both are much weaker than the incident P wave. This indicates that the absorbing boundary conditions do work. However the artificial reflections are still much stronger than the physical reflections, which is not desirable.

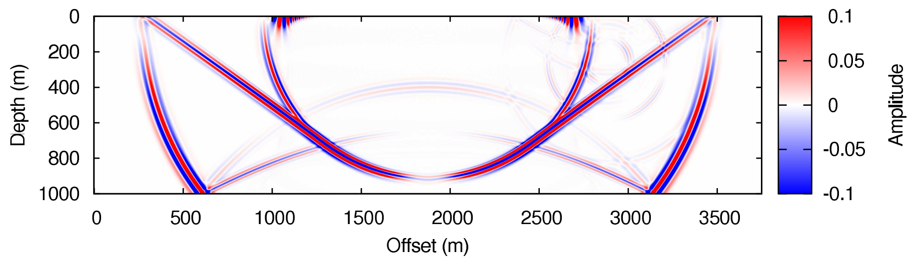

(a) Vertical component

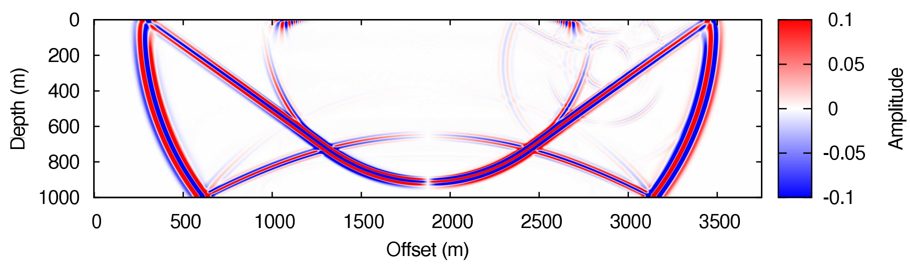

(b) Horizontal component

Figure 3.10: Modelling results using three-point absorbing boundary conditions.

Approximate with three-point difference

First order derivatives can be approximated by a two-point forward or backward difference approximation. The two-point backward approximation can be written as

$$f'(x_i) = \frac{f(x_i) - f(x_{i-1})}{h}. \tag{3.20}$$

The two-point forward and backward difference approximations have truncation errors of the order of $O(h)$.

First order derivatives can also be approximated by a three-point forward or backward difference approximation. The three-point backward approximation can be written as

$$f'(x_i) = \frac{3f(x_i) - 4f(x_{i-1}) + f(x_{i-2})}{2h}. \tag{3.21}$$

The three-point forward and backward difference approximations have truncation errors of the order of $O(h^2)$.

Thus, using three-point backward difference operators with respect to x_3 and two-point difference with respect to t, system 3.2.2, one can write absorbing boundary conditions for the bottom boundary in the staggered-grid scheme, as

$$\frac{3{v_1}_{i,K-1}^{n-1/2} - 4{v_1}_{i,K-2}^{n-1/2} + {v_1}_{i,K-3}^{n-1/2}}{2h} + \frac{{v_1}_{i,K-1}^{n+1/2} - {v_1}_{i,K-1}^{n-1/2}}{\beta \Delta t} = 0, \tag{3.22a}$$

$$\frac{3{v_3}_{i+1/2,K-1/2}^{n-1/2} - 4{v_3}_{i+1/2,K-3/2}^{n-1/2} + {v_3}_{i+1/2,K-5/2}^{n-1/2}}{2h} + \frac{{v_3}_{i+1/2,K-1/2}^{n+1/2} - {v_1}_{i+1/2,K-1/2}^{n-1/2}}{\alpha \Delta t} = 0, \tag{3.22b}$$

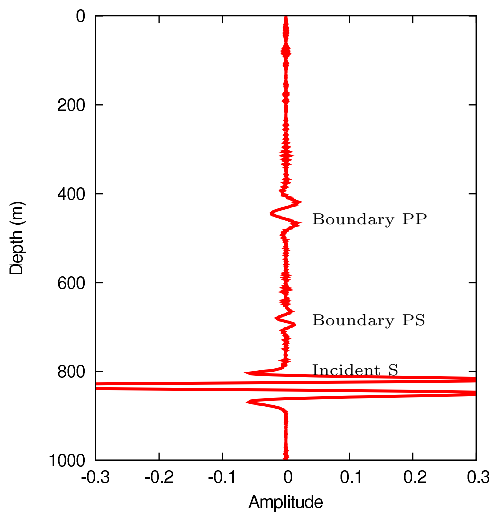

(a) Vertical component, 2-point approximation

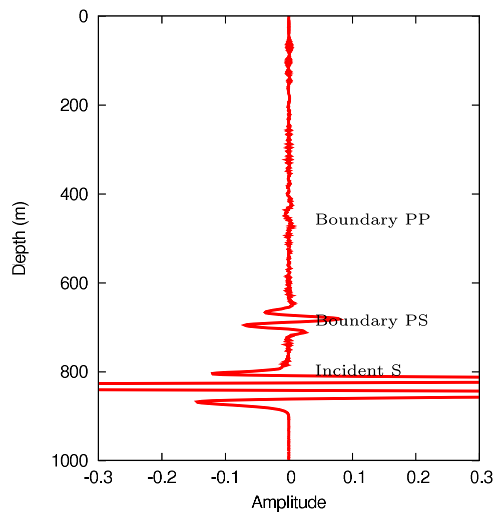

(b) Horizontal component, 2-point approximation

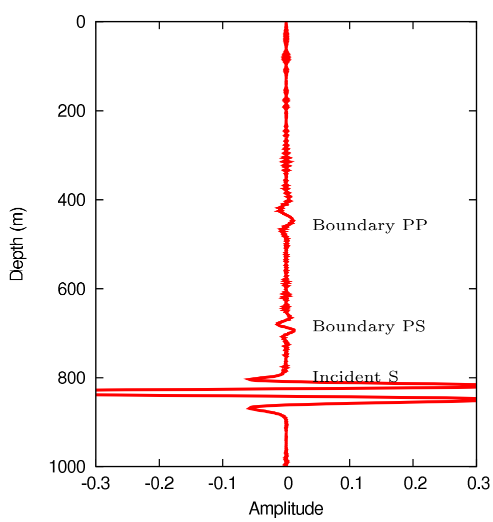

(c) Vertical component, 3-point approximation

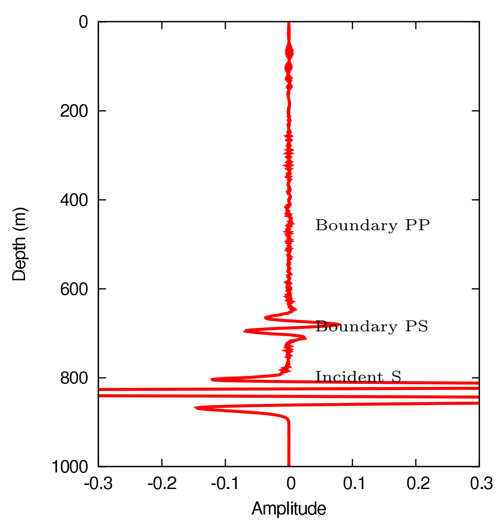

(d) Horizontal component, 3-point approximation

Figure 3.11: Wiggle plots of traces at offset 1500m from Figure 3.9 and 3.10.

Figure 3.10 shows the resulting wavefield and Figure 3.11 displays four traces from Figure 3.9 and 3.10. The boundary reflections resulted from the three-point approximation are slightly weaker. This shows that three-point approximation works better than two-point approximation.

However, the artificial reflections are still much stronger than the physical reflections. This is more evident on the PS reflections in the horizontal component plots 3.9b and 3.10b.

3.3 Nonreflecting boundary condition

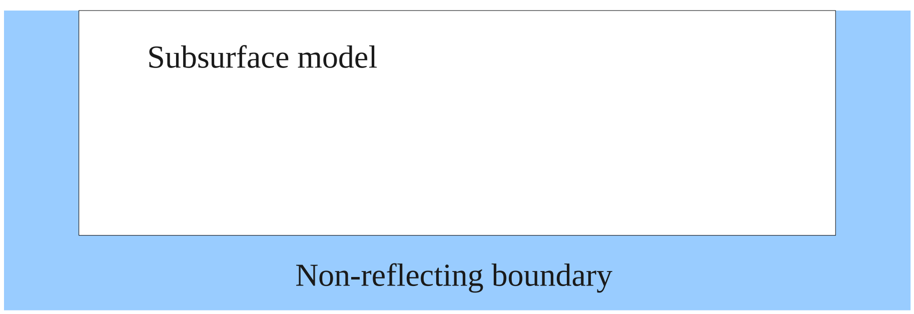

Figure 3.12: Non-reflecting boundary strips on the left, right and bottom of a subsurface model.

A nonreflecting boundary condition (Cerjan et al., 1985) employs a strip of nodes on the boundary to attenuate wave amplitudes, as shown in Figure 3.12. For a strip width of n nodes, the amplitude values are multiplied by a factor

$$G = e^{[-\epsilon(N-i)]^2}, \tag{3.23}$$

where ϵ is a constant; i denotes the grid distance between the node and the outside boundary.

Attenuating wave amplitude by the factors has two effects. First, the wave is weakened towards the outside boundary, which means the reflection from the outside boundary will be attenuated. The other effect is that, when the wave goes through the energy absorbing strip, it 'sees' the changes in impedance of the medium because of the attenuated amplitudes and then part of the wave energy will be reflected back. Thus, for a strip width of N, there seems to exist N fictitious reflectors.

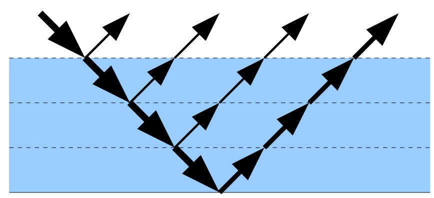

Figure 3.13: Reflections from a non-reflecting boundary.

Hence, there are two kinds of reflections generated from the nonreflecting boundary, as shown in Figure 3.13. One is from the fictitious reflectors; the other one is from the outside rigid boundary. The constant ϵ affects both reflections. The greater the constant ϵ is, the stronger the fictitious reflector reflections will be, but the weaker the outside rigid boundary reflection will be. The width N has little influence on the fictitious reflector reflections, while large N certainly results in weaker outside boundary reflections.

Figure 3.14 shows the reflections from the bottom non-reflecting boundary with parameters $\epsilon = 0.004$ and $N = 50$. A smaller ϵ and a greater N could have been used to reduce reflections to the least extent, but these parameters are chosen so that one

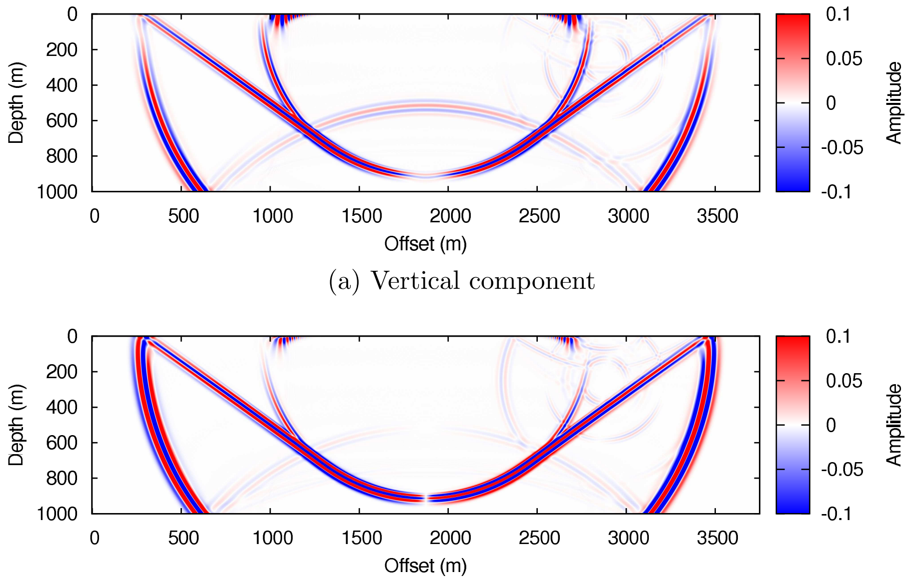

(a) Vertical component

(b) Horizontal component

Figure 3.14: Modelling results using non-reflecting boundary conditions.

can observe the reflections and compare the result to that of other methods.

3.4 Combining absorbing and nonreflecting boundary conditions

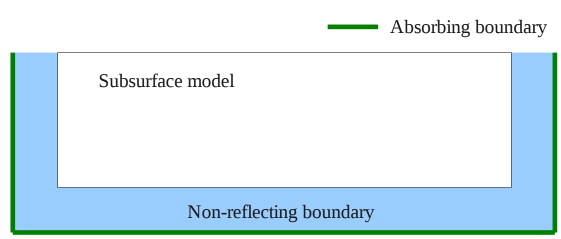

Figure 3.15: Applying absorbing boundary conditions outside of a non-reflecting boundary.

By combining absorbing boundary conditions at the outside boundary of the non-

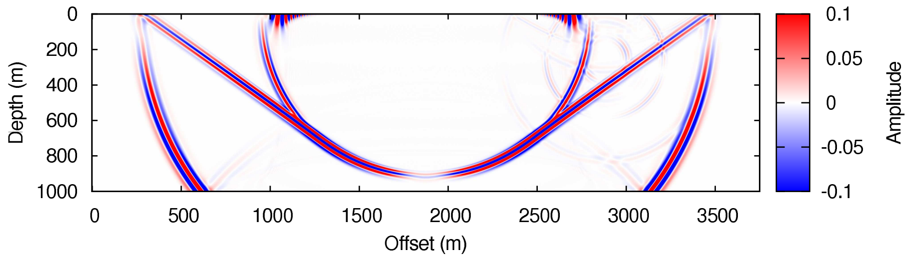

(a) Vertical component

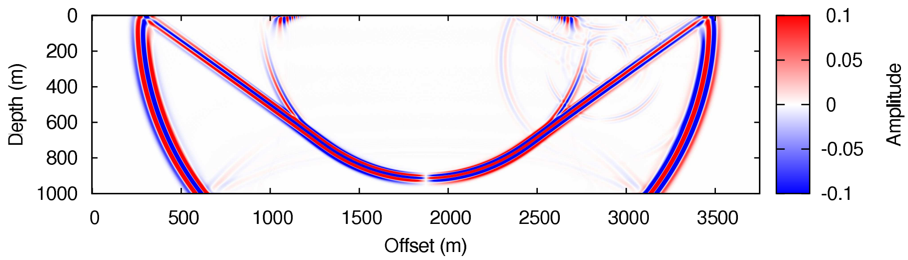

(b) Horizontal component

Figure 3.16: Modelling results using combined boundary conditions.

reflecting boundary strip (Figure 3.15), with the same strip width N and the same constant ϵ for the non-reflecting boundary, the boundary reflections can be further reduced.

Figure 3.16 shows a snapshot of the combined boundary, with parameters $\epsilon = 0.004$ and $N = 50$ for the non-reflecting strip. Compared to either the result of absorbing boundary conditions (Figure 3.9) or that of a non-reflecting boundary condition (Figure 3.14), the reflections are much weaker. The same as mentioned with non-reflecting boundary, these parameters are chosen for the sake of algorithm demonstration. It is possible to choose smaller ϵ and greater N to reduce the resident reflections to the least extent.

3.5 Computational costs of boundaries

In addition to the wavefield computing within the subsurface model, there are more computational resources involved if a nonreflecting boundary condition is employed.

First, more memory is required for non-reflecting boundary condition, since finite-difference nodes are padded to the subsurface model. In the cases of above non-reflecting boundary and combined boundary experiments, the number of nodes in the subsurface model are $3000 \times 800 = 2400000$, and the additional number of non-reflecting boundary nodes is 235000, so the memory requirement is increased by 10.2%.

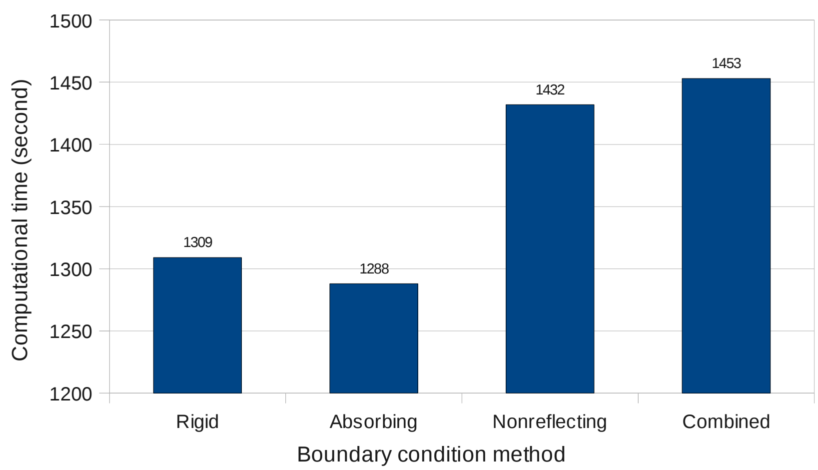

Figure 3.17: Computational times of different boundary conditions.

Second, more computational time is required for nonreflecting boundary condition and combined boundary conditions. Figure 3.17 lists the total computational times when rigid, absorbing, non-reflecting, or combined boundary condition is applied to the same subsurface model as shown in Figure 3.8. The computational times of non-reflecting and combined boundary conditions are approximately 10% longer than those of rigid and absorbing boundary conditions. The increase rate is consistent with that of memory.

The computational time of the rigid boundary is longer than that of the absorbing boundary. This is a surprise at the first look since a rigid boundary seems less computational intensive than an absorbing boundary. However, a closer check on the rigid boundary (see section 3.1) reveals that a rigid boundary is actually more computational intensive than an absorbing boundary.

3.6 Chapter summary

This chapter has focused on one of the most important issues in wave modelling: computational boundary problem.

Results from numerically modelling of rigid boundaries are consistent with theoretical predictions. On one hand, this confirms the problem of the computational boundaries. On the other hand, it also verifies the correctness of the modelling algorithms.

The method of absorbing boundary conditions (Clayton and Engquist, 1977) works well for 1D wave case. However, reflections resulted from an absorbing boundary in 2D can be stronger than those from physical reflectors.

The method of the nonreflecting boundary condition (Cerjan et al., 1985) can reduce artifacts to any extent if the nonreflecting stripes are thick enough. However, thick nonreflecting stripes lead to extra computational costs.

The proposed method, which combines the absorbing boundary and the nonreflecting boundary, works better, in terms of reducing artificial reflections and computational costs.

Chapter 4

Reverse-time migration

After introduction to the principles of reverse-time migration, this chapter examines some popular imaging conditions for reverse-time migration and demonstrates an improved method of imaging conditions for multi-component processing. The analysis is done using the point reflector subsurface model used in Chapter 2.

A prestack reverse-time migration workflow is sketched and tested with a shrunk Marmousi2 model and a dipping layer model. The processing workflow is very different from the traditional seismic data processing workflow. For example, it is not necessary to remove ground roll from surface records.

4.1 Principles of reverse-time migration

4.1.1 Time reversed waves

A brief yet clear explanation of the principle behind reverse-time migration can be found in Lines and Newrick (2004, chap. 6). For 1D homogeneous wave equation,

$$\frac{\partial^2 u}{\partial x^2} = \frac{1}{v^2}\frac{\partial^2 u}{\partial t^2}, \tag{4.1}$$

a general solution is of the form

$$u = f(x + vt) + g(x - vt), \tag{4.2}$$

where f and g are arbitrary functions that are twice differentiable. It can be shown that the solutions to the wave equation remains valid if one changes the sign of t. In other words, mathematically, a time reversed wave will still obey the wave equation, although with time in the physical world, we can progress in only one direction.

Thus, the numerical forward modelling and reverse-time extrapolation should and can be done with the rules of the same wave equation. Take the above 1D homogeneous case for example, the numerical implementation of the above principle is as follows. Approximated with central difference, the above wave equation can be written as

$$\frac{u(t + \Delta t) - 2u(t) + u(t - \Delta t)}{\Delta t^2} = \frac{1}{v^2} \frac{u(x + h) - 2u(x) + u(x - h)}{h^2}, \tag{4.3}$$

where Δt and h are, respectively, time step and space step of finite difference. On one hand, the forward modelling of wave is

$$u(t + \Delta t) = 2u(t) - u(t - \Delta t) + \frac{\Delta t^2}{v^2} \left(\frac{u(x + h) - 2u(x) + u(x - h)}{h^2} \right), \tag{4.4}$$

where wavefield at a next time step is approximated from the previous times. On the other hand, the reverse-time extrapolation of wave is

$$u(t - \Delta t) = 2u(t) - u(t + \Delta t) + \frac{\Delta t^2}{v^2} \left(\frac{u(x + h) - 2u(x) + u(x - h)}{h^2} \right), \tag{4.5}$$

where wavefield at a previous time step is extrapolated from the next times.

The above description is for the acoustic case. In the thesis, elastic waves are stepped backwards in time.

4.1.2 Imaging principle

The imaging principle (Claerbout, 1971) states “Reflectors exist at points in the ground where the first arrival of downgoing wave is time coincide with an upgoing wave”.

Imaging conditions are implementations of the imaging principle. People have practiced various imaging conditions. Most of the imaging conditions are for acoustic case, but recently elastic imaging conditions have also appeared.

Some popular acoustic (scalar) imaging conditons are: ratio of upgoing over downgoing wavefield amplitudes (Claerbout, 1971; Chattopadhyay and McMechan, 2008), cross-correlation (Claerbout, 1971; Biondi and Shan, 2002), source normalized cross-correlation (Whitmore and Lines, 1986), ray tracing (Chang and McMechan, 1987), minimum time (Loewenthal and Hu, 1991; Chattopadhyay and McMechan, 2008), maximum amplitude (Loewenthal and Hu, 1991), and receiver normalized cross-correlation (Kaelin and Guitton, 2006),

Two categories of elastic imaging conditions have emerged. The first one is based on wavefield decomposition or wave-mode separation. Multicomponent wavefields are separated into P and S waves based on Helmholtz decomposition (Yan and Sava, 2007). The second category is based on the elastic wavefields without decomposition. For example, Du et al. (2012) presented source normalized cross-correlation imaging conditions with polarity reversal correction. The imaging conditions discussed in the dissertation fall into the second category.

Note that ‘source wavefield’, ‘downgoing wavefield’, and ‘incident wavefield’ are used as synonyms in this chapter, and so are ‘receiver wavefield’, ‘upgoing wavefield’, and ‘reflected wavefield’.

4.2 Reverse-time extrapolation: a point reflector

The same point reflector subsurface model used in modelling, whose P-wave velocities are shown in Figure 2.23, is used here.

Two modelling experiments analyzed in subsection 2.5.2.3 and 2.5.2.4 are used here in the reverse-time migration experiments. The first experiment is done with a centre surface source, and the second with a horizontally far-away surface source.

4.2.1 Reverse-time extrapolation: centre shot

Figure 4.1 shows snapshots from a centre source experiment. Three columns in the figure are, respectively, the forward modelling, the reverse-time extrapolation, and their cross-correlation term. Vertically, the snapshots are in time order.

Forward modelling and downgoing waves

Forward modelling creates the “downgoing” waves, so-called by Claerbout (1971).

The forward modelling snapshots are created from the same forward modelling experiment as shown in Figure 2.25.

The left column of Figure 4.1 shows forward modelling snapshots in time order. In the experiment, the P and S downgoing waves each strikes the point reflector once, which happen at times of around 0.135s and 0.235s. At first, at time 0.135s, as shown

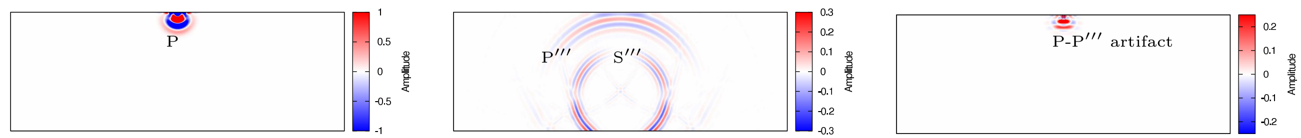

(a) Forward modelling, 0.035s

(b) Reverse-time extrapolation, 0.035s

(c) Cross-correlation term, 0.035s

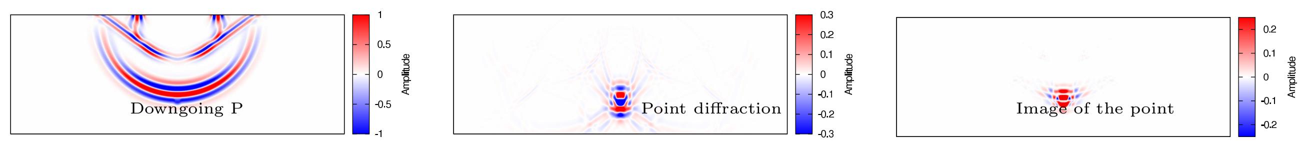

(d) Forward modelling, 0.135s

(e) Reverse-time extrapolation, 0.135s

(f) Cross-correlation term, 0.135s

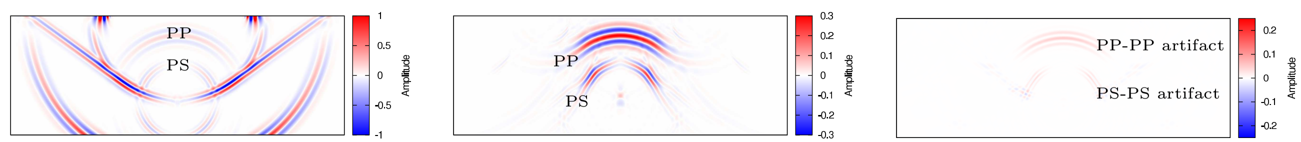

(g) Forward modelling, 0.235s

(h) Reverse-time extrapolation, 0.235s

(i) Cross-correlation term, 0.235s

Figure 4.1: Forward modelling, reverse-time extrapolation of P-SV waves, and their point by point multiplication. The multiplication shows as a cross-correlation term in Equation 4.7. The wave modelling is done with a centre surface source. This is the vertical component [to be continued].

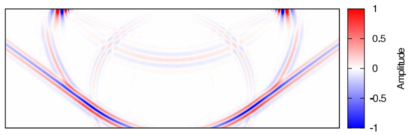

(j) Forward modelling, 0.335s

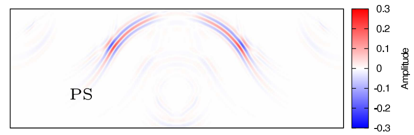

(k) Reverse-time extrapolation, 0.335s

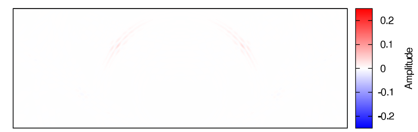

(l) Cross-correlation term, 0.335s

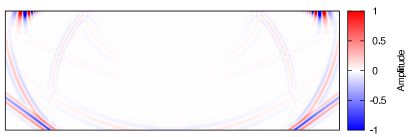

(m) Forward modelling, 0.435s

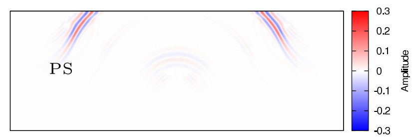

(n) Reverse-time extrapolation, 0.435s

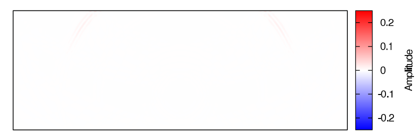

(o) Cross-correlation term, 0.435s

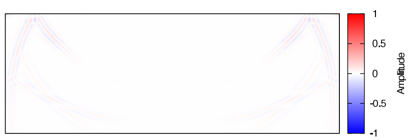

(p) Forward modelling, 0.535s

(q) Reverse-time extrapolation, 0.535s

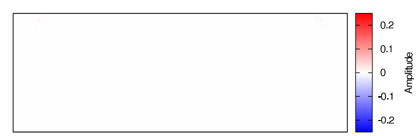

(r) Cross-correlation term, 0.535s

Figure 4.1: [Continued]

in Figure 4.1d, an incident P wave strikes the point reflector and diffraction starts to appear on the snapshot, and the reflected PP and PS waves are shown in Figure 4.1g. Then, at time 0.235s, as shown in Figure 4.1g, an incident S wave strikes the point reflector and another diffraction shows up. However, the incident S wave upon the point reflector is very weak and the second diffraction is also weak. Thus the main reflections recorded, PP and PS, are caused by the 0.135s P-wave strike. Figure 2.26 shows the surface records.

Reverse-time extrapolation and upgoing waves

Reverse-time extrapolation of surface records creates the "upgoing" waves, so-called by Claerbout (1971). That is, the upgoing (reflected) wavefield in the subsurface is reconstructed from the surface records.

Reverse-time extrapolation is mostly the same processing as forward modelling: the same finite-difference formulas and boundary conditions are used to do reverse-time extrapolation. Nevertheless, during this processing the surface record acts as numerous sources, and the process is reversed in time.

It is assumed that the medium is in equilibrium at the beginning of reverse-time extrapolation, i.e., initially stresses and particle velocities are set to zero everywhere in the medium. The assumption is usually not true because the time the extrapolation starts is the time that one stops the forward modelling of the incident wave, or the time that one stops recording in a real acquisition experiment, while at this time the subsurface wavefield usually exists. However, it is chosen to follow the false assumption of zero initial condition. For one thing, one wants to reconstruct upgoing wavefield without the downgoing wavefield. For another, the subsurface wavefield is unknown in a real seismic experiment. The false assumption of zero initial condition

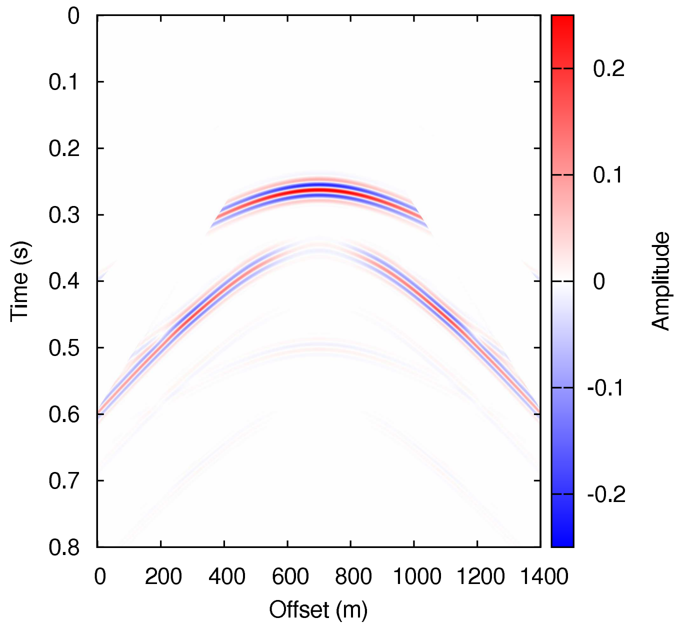

(a) Vertical component

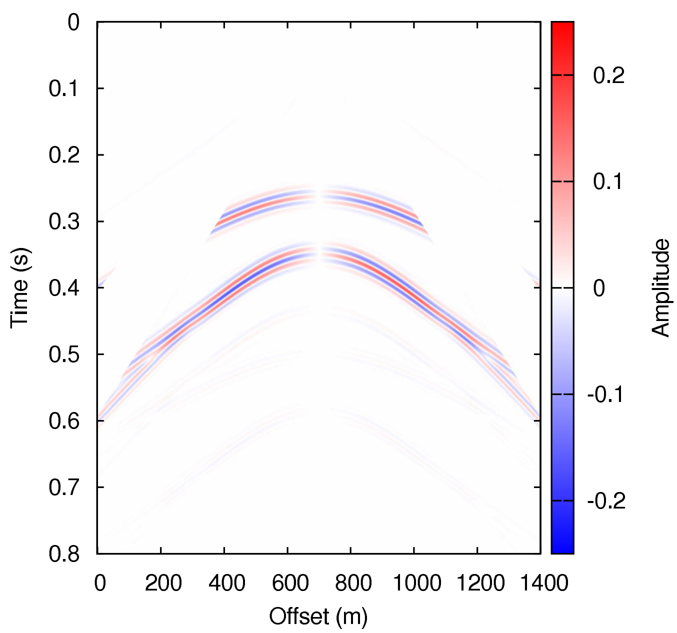

(b) Horizontal component

Figure 4.2: Muted surface records from a centre surface source. The corresponding records without muting are shown in Figure 2.26.

causes artifacts during the extrapolation, though. This was found by comparing two experimental results: in one experiment the modelled wavefield was used as the initial values, while in another experiment, zeros were used instead.

It is necessary to preprocess the surface record before it is used to do reverse-time extrapolation.

First, direct P-wave arrivals in surface records are connected to the source generated P wavefronts in the subsurface, so it is necessary to remove direct P-wave arrivals from surface records. This is done by muting.

Second, head waves arriving as first breaks are muted from surface records.

Third, consideration is given to ground roll, the Rayleigh waves in seismic records. In traditional seismic data processing based on Kirchhoff migration, ground roll has to be removed, which usually turns out to be a challenging task if one wants to keep the reflected energy intact. However, in my point of view, for reverse-time migration, it is not critical to remove ground roll in surface records, since the extrapolated energy in the subsurface will be surface waves, which only affect very shallow subsurface imaging. Based on this judgment, the ground roll in the migration of the shrunk Marmousi2 data later in this chapter, which are difficult to remove, are not removed. However, in the point reflector experiments in this section (Section 4.2), the ground roll is simply muted from surface records. Figure 4.2 shows muted surface records of the centre shot, which are in Figure 2.26.

The central column of Figure 4.1 shows snapshots resulted from reverse-time extrapolation. Reverse-time extrapolation starts from the end of the forward modelling time. Fed from the surface with preprocessed surface records, PS waves propagate downwards from time 0.535s (Figure 4.1q), to 0.435s (Figure 4.1n), and then to 0.335s

(Figure 4.1k). At 0.235s, as shown in Figure 4.1h, PS waves keep going down, and a PP wave also propagates down. The PP wave travels at a higher velocity and eventually merged together with the PS waves at time 0.135s at the position of the point reflector, as shown in Figure 4.1e. After striking the point reflector, the wave energy reverse-time extrapolated as reflections, annotated as P''' and S''' in Figure 4.1b.

Cross-correlation and time coincidence of waves

Projecting the upgoing wavefield to a downgoing wavefield is a means of measuring how much of the upgoing wavefield is coincident with the downgoing wavefield. This projecting is done by multiplying the upgoing wavefield at a certain time to the corresponding downgoing wavefield point by point. This is equivalent to a zero-lag cross-correlation term.

The right column of Figure 4.1 shows the cross-correlation snapshots.

At time 0.135s (Figure 4.1f), the cross-correlation results in strong energy. This is the product of the incident P wave shown in Figure 4.1d and the reflected PP wave shown in Figure 4.1e. Thus, this energy is a real image of the point reflector.

However, some cross-correlation energy exists at times 0.035s (Figure 4.1c) and 0.235s (Figure 4.1i). There are no corresponding reflectors in the subsurface model, and that cross-correlation energy is regarded as imaging noise. In fact, the imaging artifact shown in Figure 4.1c is caused by the incident P wave shown in Figure 4.1a and the reverse-time extrapolated P''' wave shown in Figure 4.1b. Since the incident P wave and the reverse-time extrapolated P''' wave travel in different directions, they appear at the same space only for a short time. Thus this kind of imaging artifact, annotated as 'P-P''' artifact', distributes in limited space. However, the imaging artifact shown in Figure 4.1i is caused by the reflected PP wave shown in Figure 4.1g and the reverse-time extrapolated PP wave shown in Figure 4.1h. Since the reflected PP wave and the reverse-time extrapolated PP wave always travel at the same time and in the same space, this kind of imaging artifact, annotated as ‘PP-PP artifact’, spreads everywhere between the seismic energy source and the reflector.

Horizontal component

Figure 4.1 shows only the vertical component. The horizontal component is used in reverse-time migration for subsurface imaging as well. For example, Figure 4.3 shows horizontal component snapshots of forward modelling and reverse-time extrapolation, and snapshots of horizontal component involved cross-correlation at time 0.135s.

The cross-correlation of horizontal component of downgoing waves with upgoing waves (Figure 4.3d and 4.3e) does not provide much subsurface imaging information. This is not surprising, since the incident P wave upon the point reflector does not cause much horizontal vibrations at all.

However, the cross-correlation of vertical component of downgoing waves with horizontal component of upgoing waves, as shown in Figure 4.3c, shows strong subsurface imaging energy. In fact, this valuable information is comparable to the cross-correlation of vertical component of downgoing waves with vertical component of upgoing waves, as shown in Figure 4.1f.

4.2.2 Reverse-time extrapolation: far-away surface source

Figure 4.4 shows snapshots generated with a surface source located far away from the point reflector.

The left column of Figure 4.4 shows forward modelling snapshots. In the experiment, the downgoing waves strike the point reflector twice, at times of 0.17s and

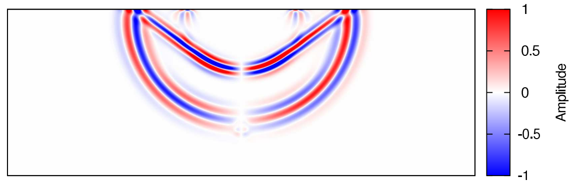

(a) Forward modelling, horizontal component

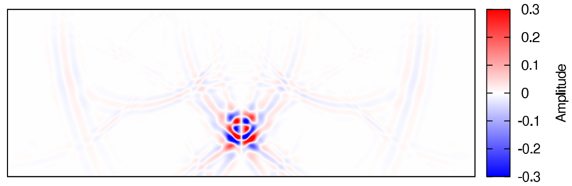

(b) Reverse-time extrapolation, horizontal component

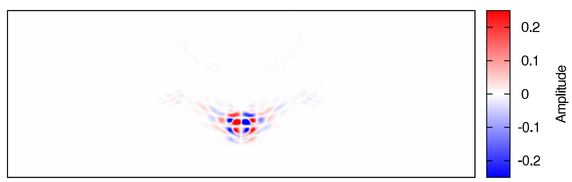

(c) Cross-correlation term, vertical component in Figure 4.1d versus horizontal component in Figure 4.3b

(d) Cross-correlation term, horizontal component in Figure 4.3a versus vertical component in Figure 4.1e

(e) Cross-correlation term, horizontal component in Figure 4.3a versus horizontal component in Figure 4.3b

Figure 4.3: Horizontal component snapshots which are involved in forward modelling, reverse-time extrapolation, and cross-correlation at time 0.135s. For comparison, amplitude clips are the same as corresponding plots in Figure 4.1.

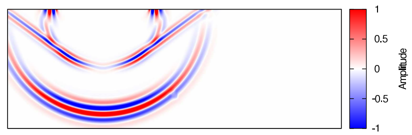

(a) Forward modelling, 0.17s

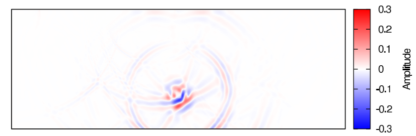

(b) Reverse-time extrapolation, 0.17s

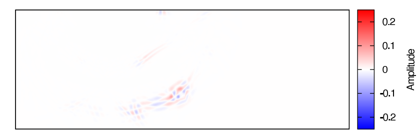

(c) Cross-correlation term, 0.17s

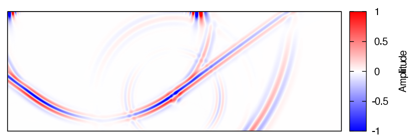

(d) Forward modelling, 0.29s

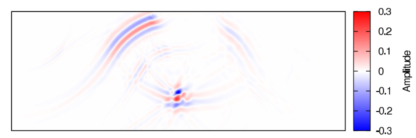

(e) Reverse-time extrapolation, 0.29s

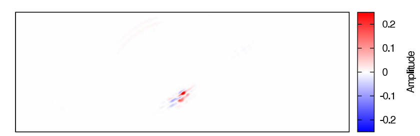

(f) Cross-correlation term, 0.29s

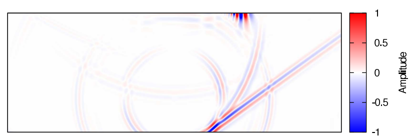

(g) Forward modelling, 0.41s

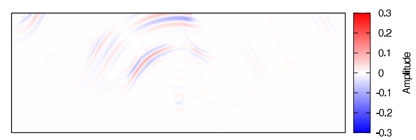

(h) Reverse-time extrapolation, 0.41s

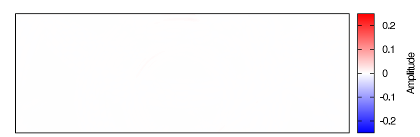

(i) Cross-correlation term, 0.28s

Figure 4.4: Forward modelling and reverse-time extrapolation of P-SV waves, and their cross-correlation. The modelling is done with a surface source which is horizontally far away from the surface centre. This is the vertical component.

0.29s, respectively. At first, at time 0.17s, as shown in Figure 4.4a, an incident P wave strikes the point reflector and diffraction starts to appear on the snapshot. Then, at time 0.29s, as shown in Figure 4.4d, an incident S wave strikes the point reflector and another diffraction starts to appear. Different from the centre source shot, the incident S wave here is strong and the reflected SP and SS waves are also strong. Thus the main reflections recorded, PP, PS, SP, and SS, are caused by the 0.17s P-wave strike and 0.29s S-wave strike. Figure 2.29 shows the surface records.

The central column of Figure 4.4 shows reverse-time extrapolation snapshots. Reverse-time extrapolation starts from the end of the forward modelling time. Fed on the surface with preprocessed surface records, SS waves propagate downwards, and at time 0.41s (Figure 4.4h) SS and SP wave energy has already completely extrapolated from the surface record to the subsurface. At time 0.29s (Figure 4.4e), the SP wave merges to the SS wave at the point reflector, while PS and PP waves are still on their way towards the point reflector. Eventually PS and PP waves merge at the point reflector at the time about 0.17s (Figure 4.4b).

The right column of Figure 4.4 shows the cross-correlation snapshots. Two snapshots, Figure 4.4c and 4.4f, show strong imaging energy. The image energy in Figure 4.4c is caused by the downgoing P wave and its reflections restored in reverse-time extrapolation, and the imaging energy in Figure 4.4f is caused by the downgoing S wave and its reflections restored in reverse-time extrapolation. These parts of imaging energy are desirable.

4.3 Imaging conditions

4.3.1 Cross-correlation imaging condition without normalization

An imaging condition for a shot gather in prestack reverse-time migration is a zero-lag cross-correlation of source waves and receiver wavefields (Claerbout, 1971; Biondi and Shan, 2002)

$$Image(x_1, x_3) = \sum_t S(x_1, x_3, t) R(x_1, x_3, t), \tag{4.6}$$

where $S(x_1, x_3, t)$ and $R(x_1, x_3, t)$ are, respectively, the source and receiver wavefields. The cross-correlation term $S(x_1, x_3, t)R(x_1, x_3, t)$ at a certain time looks like a snapshot shown on the right column of Figure 4.1. Thus the imaging condition for a shot gather in equation 4.6 is implemented by stacking all the cross-correlation snapshots.

For a multi-component algorithm, there are both horizontal and vertical components for both source and receiver wavefields. Thus, one can actually have four cross-correlation imaging conditions:

$$I_{VV}(x_1, x_3) = \sum_t S_V(x_1, x_3, t) R_V(x_1, x_3, t), \tag{4.7a}$$

$$I_{VH}(x_1, x_3) = \sum_t S_V(x_1, x_3, t) R_H(x_1, x_3, t), \tag{4.7b}$$

$$I_{HV}(x_1, x_3) = \sum_t S_H(x_1, x_3, t) R_V(x_1, x_3, t), \tag{4.7c}$$

$$I_{HH}(x_1, x_3) = \sum_t S_H(x_1, x_3, t) R_H(x_1, x_3, t), \tag{4.7d}$$

where subscripts V and H denotes, respectively, vertical and horizontal components. Hereafter the imaging conditions will be referred to as VV, VH, HV, and HH imaging conditions.

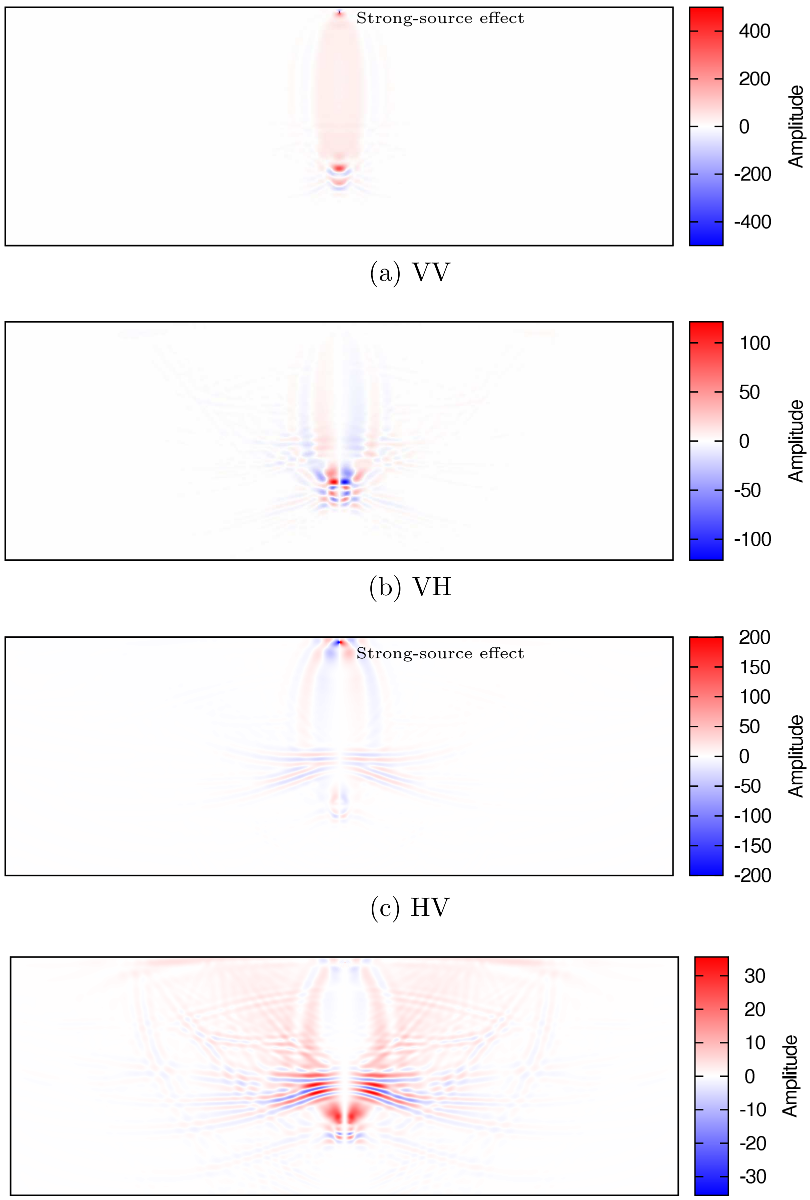

(a) VV

(b) VH

(c) HV

(d) HH

Figure 4.5: Centre shot imaging result of cross-correlation without normalization.

Figure 4.5 shows imaging results from the centre source shot, and Figure 4.6 shows

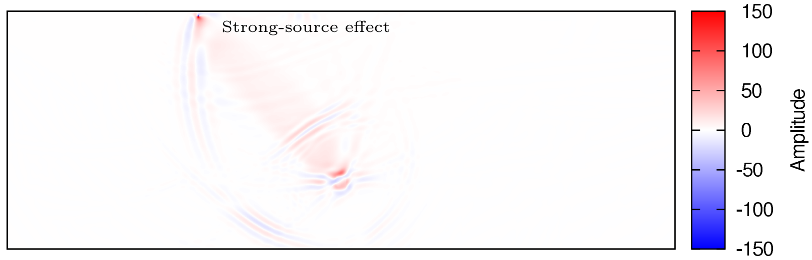

(a) VV

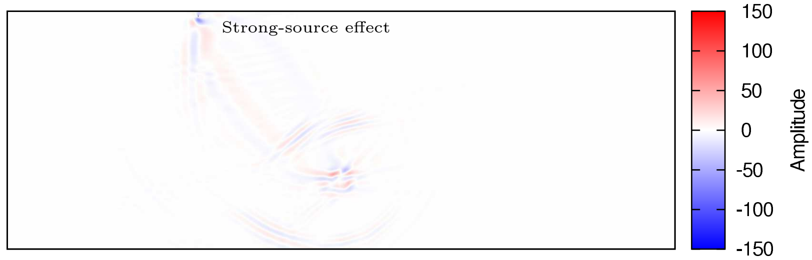

(b) VH

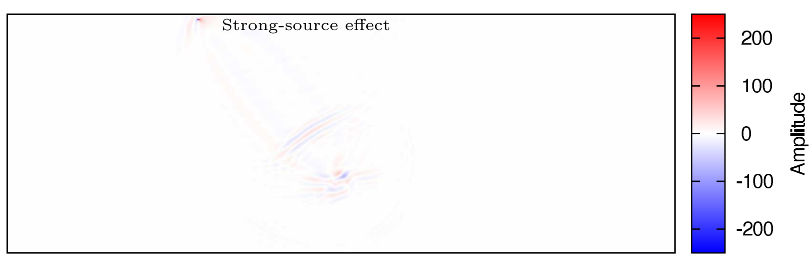

(c) HV

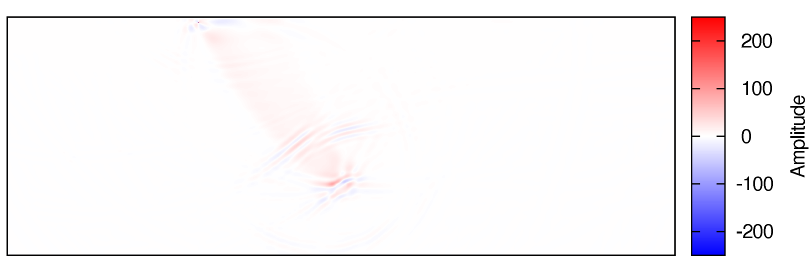

(d) HH

Figure 4.6: Far-away source shot imaging result of cross-correlation without normalization.

images from the far-away source shot. As stated in the paper by Claerbout (1971), the imaging energy "drops off rapidly in any region where either the downgoing wave is weak or the upgoing wave is weak". This is a desirable property. First, for regions where the downgoing wave is coincident with the upgoing wave, there is imaging energy; second, for stronger coincidence, there is stronger imaging energy. However, for the regions close to the seismic energy source point, where the downgoing wave, or source wavefield, is very strong, the imaging energy becomes very high. This source effect of imaging is not a desirable property. This is referred in this dissertation as 'strong-source effect' of cross-correlation imaging conditions, in order to distinguish this kind of source effect from another kind of source effect described in the next subsection. Strong-source effect can be observed in Figure 4.5a, 4.5c, 4.6a, 4.6b, and 4.6c.

4.3.2 Source normalized cross-correlation imaging conditions

Source normalized cross-correlation imaging condition for an acoustic shot gather is given as (Whitmore and Lines, 1986; Kaelin and Guitton, 2006; Chattopadhyay and McMechan, 2008)

$$Image(x_1, x_3) = \frac{\sum_t S(x_1, x_3, t) R(x_1, x_3, t)}{\sum_t S^2(x_1, x_3, t)}. \tag{4.8}$$

Obviously, when implement the imaging condition, one needs to employ one of the techniques to avoid the problem of division by zero. One technique is to use an additive constant in the denominator. Some other methods are based on a threshold: if the denominator or the numerator is less than a certain threshold, the imaging result is set to zero. In the thesis, the auther used a threshold for the denominator.

Because the source wavefield auto-correlation term is used as the denominator on the right, for regions close to the shot point, the imaging energy will be brought down. Hence, the strong-source effect is suppressed.

For a multi-component algorithm, Du et al. (2012) re-wrote the above imaging condition to four equations as follows.

$$I_{VV}(x_1,x_3) = \frac{\sum_t S_V(x_1,x_3,t)R_V(x_1,x_3,t)}{\sum_t S_V^2(x_1,x_3,t)}, \tag{4.9a}$$

$$I_{VH}(x_1,x_3) = \frac{\sum_t S_V(x_1,x_3,t)R_H(x_1,x_3,t)}{\sum_t S_V^2(x_1,x_3,t)}, \tag{4.9b}$$

$$I_{HV}(x_1,x_3) = \frac{\sum_t S_H(x_1,x_3,t)R_V(x_1,x_3,t)}{\sum_t S_H^2(x_1,x_3,t)}, \tag{4.9c}$$

$$I_{HH}(x_1,x_3) = \frac{\sum_t S_H(x_1,x_3,t)R_H(x_1,x_3,t)}{\sum_t S_H^2(x_1,x_3,t)}, \tag{4.9d}$$

where a denominator uses the same component of source wavefield in the numerator.

Figure 4.7 shows the resulting centre shot images. Comparing Figure 4.7a to Figure 4.5a, and Figure 4.7c to Figure 4.5c, one can observe that the imaging energy close to the shot point has gone, i.e., strong-source effect is suppressed.

However, there is another kind of source effect. Figure 4.7c and 4.7d show high imaging energy right below the seismic energy source position. This is caused by the fact that the horizontal component of the downgoing wave is very weak: the incident P wavefront right under the source causes no or very weak horizontal vibrations of rock particles, and the incident S wave front right under the source causes no or very weak vibrations (horizontal or vertical) either. I call this ‘weak-source effect’ of source normalized imaging conditions.

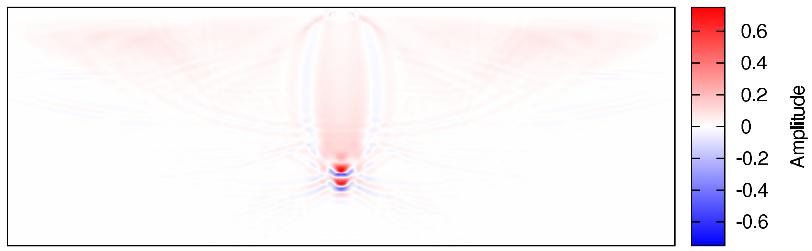

(a) VV

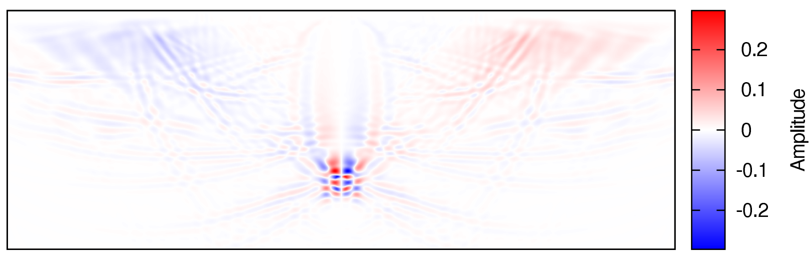

(b) VH

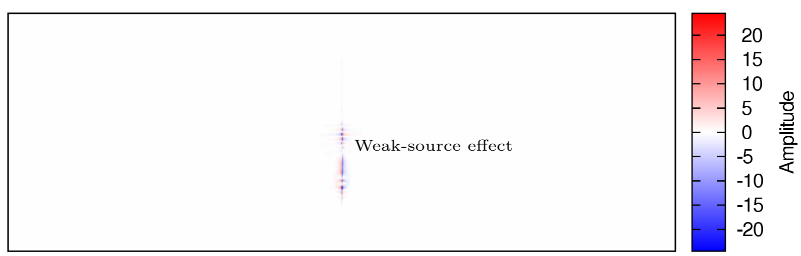

(c) HV

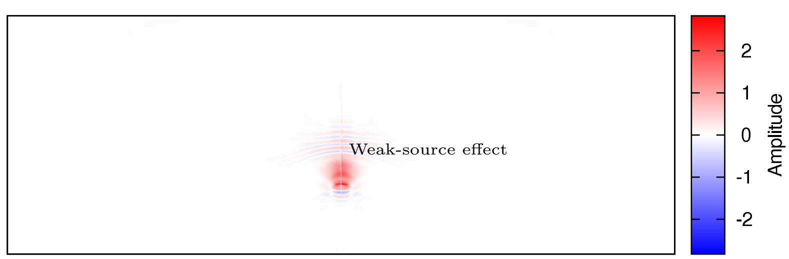

(d) HH

Figure 4.7: Centre shot imaging result of cross-correlation with source normalization.

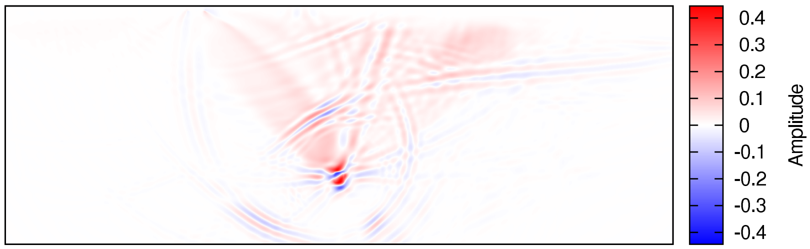

(a) VV

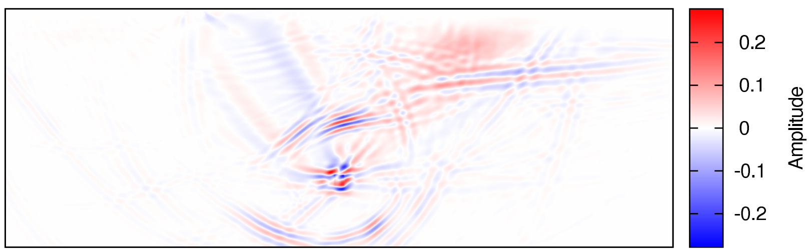

(b) VH

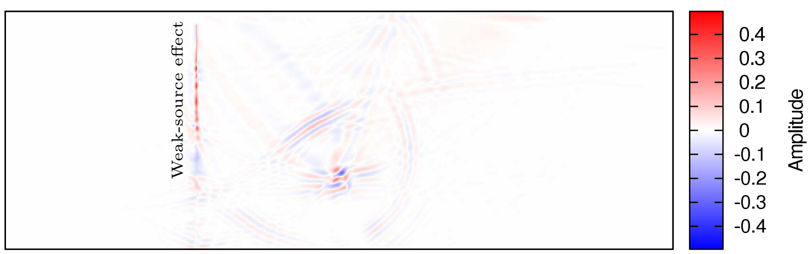

(c) HV

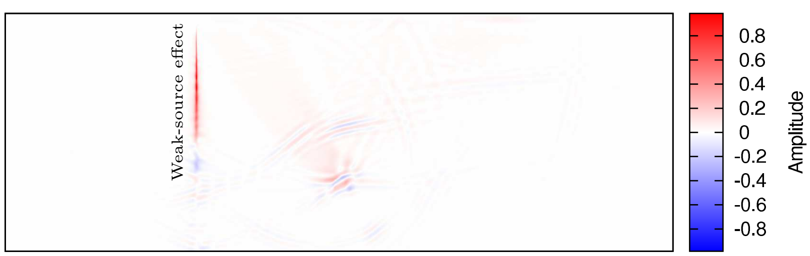

(d) HH

Figure 4.8: Far-away source shot imaging result of cross-correlation with source normalization.

The weak-source effect of imaging conditions is seen more evidently in the far-away source shot images of Figure 4.8.

I have tried some methods to suppress the weak-source effect within the frame of source normalized cross-correlation imaging condition. One method is to detect surrounding energy level, and decide an imaging threshold to avoid the false imaging. The method works well, especially when the source and the reflector are not in the same horizontal range. However, the method presented in the next subsection is a more general solution to the weak-source effect problem.

4.3.3 Source energy normalized cross-correlation imaging condition

By slightly modify the source normalized cross-correlation imaging conditions, I get another set of imaging conditions as follows.

$$I_{VV}(x_1,x_3) = \frac{\sum_t S_V(x_1,x_3,t)R_V(x_1,x_3,t)}{\sum_t \left(S_V^2(x_1,x_3,t)+S_H^2(x_1,x_3,t)\right)}, \tag{4.10a}$$

$$I_{VH}(x_1,x_3) = \frac{\sum_t S_V(x_1,x_3,t)R_H(x_1,x_3,t)}{\sum_t \left(S_V^2(x_1,x_3,t)+S_H^2(x_1,x_3,t)\right)}, \tag{4.10b}$$

$$I_{HV}(x_1,x_3) = \frac{\sum_t S_H(x_1,x_3,t)R_V(x_1,x_3,t)}{\sum_t \left(S_V^2(x_1,x_3,t)+S_H^2(x_1,x_3,t)\right)}, \tag{4.10c}$$

$$I_{HH}(x_1,x_3) = \frac{\sum_t S_H(x_1,x_3,t)R_H(x_1,x_3,t)}{\sum_t \left(S_V^2(x_1,x_3,t)+S_H^2(x_1,x_3,t)\right)}. \tag{4.10d}$$

The denominators on the right are the sum of zero-lag auto-correlation of both source components. And this is expected to help reduce the weak-source effect. Also, it makes more sense to use the whole source wave energy as the denominator than to use only one component - The reflections are caused by the whole source wave instead of one component, after all.

The acoustic imaging condition (Equation 4.8) is expected to extrapolate the acoustic reflection coefficients. Correspondingly, each of the four imaging conditions in Equation 4.10 can be interpretated as a linear combination of the PP, PS, SP, SS reflection coefficients, and each imaging condition is a brute approximation of the reflection coefficients: VV imaging condition is an approximation of PP reflection coefficients, VH is of PS, and so on.

Since the right side of the four equations in 4.10 has the same denominator, it is reasonable to try to stack the four images together as follows.

$$\begin{aligned} &Image(x_1, x_3) \\ =&I_{VV}(x_1, x_3) + I_{VH}(x_1, x_3) + I_{HV}(x_1, x_3) + I_{HH}(x_1, x_3) \\ =&\frac{\sum_t (S_V R_V + S_V R_H + S_H R_V + S_H R_H)}{\sum_t (S_V^2 + S_H^2)}. \end{aligned} \tag{4.11}$$

where S_V,S_H, R_V, and R_H are all functions of (x_1, x_3, t). The stacking operator in the above equation seems to be unclear in physical meanings, but it leads to sharper and clearer maps of subsurface structures, as shown later.

The sum of zero-lag auto-correlation of both source components has the physical interpretation of the wave energy. Thus, I call the above five equations 'source energy normalized cross-correlation imaging conditions'.

Figure 4.9 shows the resulting centre source shot images and Figure 4.10 shows the resulting far-away source shot images.

There are advantages of source energy normalized imaging conditions. On one hand, comparing to the imaging conditions without normalization (Figure 4.5 and 4.6), the source energy normalized imaging conditions do not lead to a strong-source effect. On the other hand, comparing to the source normalized imaging conditions

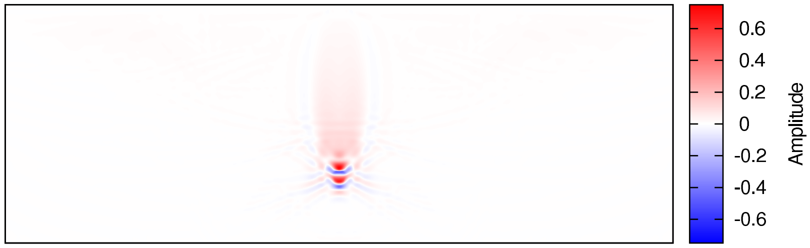

(a) VV

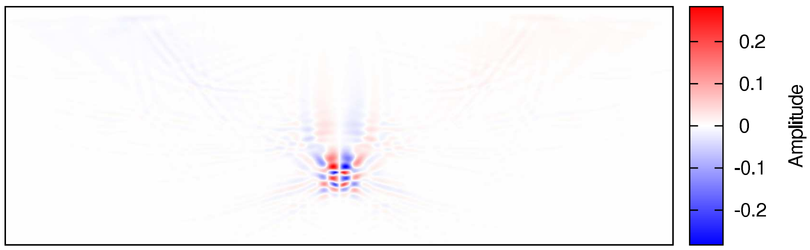

(b) VH

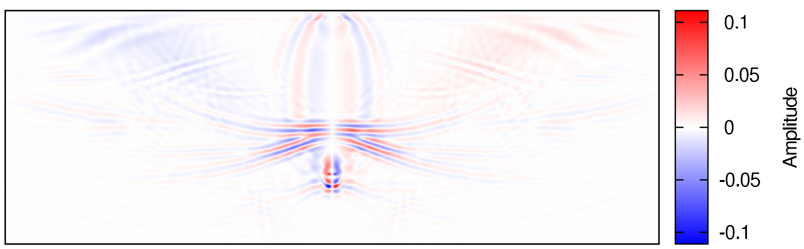

(c) HV

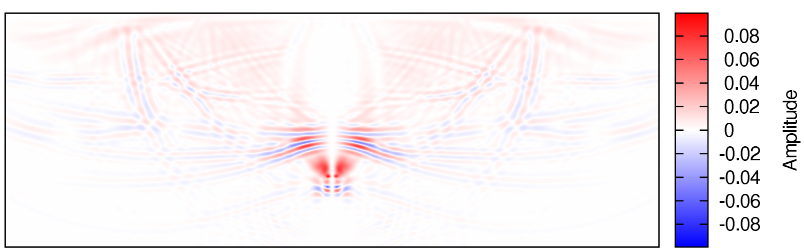

(d) HH

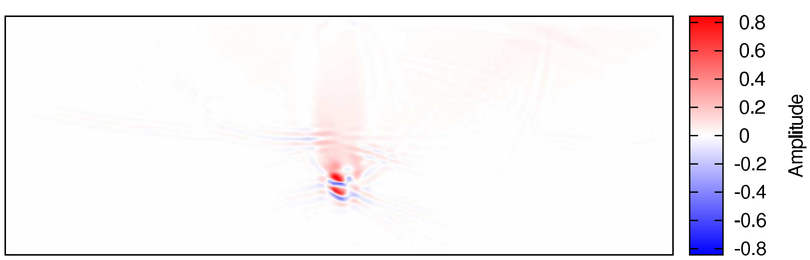

(e) Stack of above four images

Figure 4.9: Centre shot image with source energy normalization.

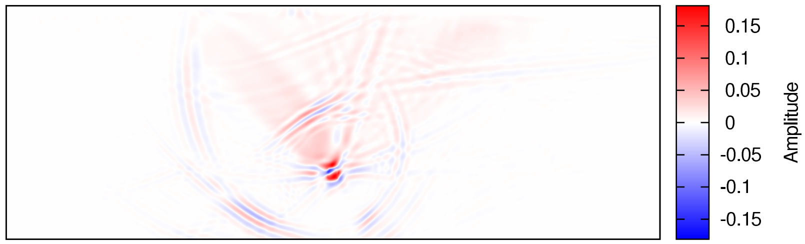

(a) VV

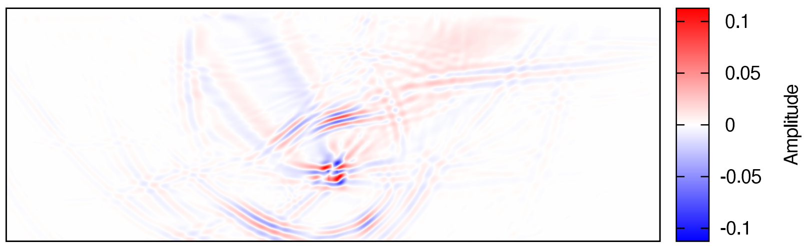

(b) VH

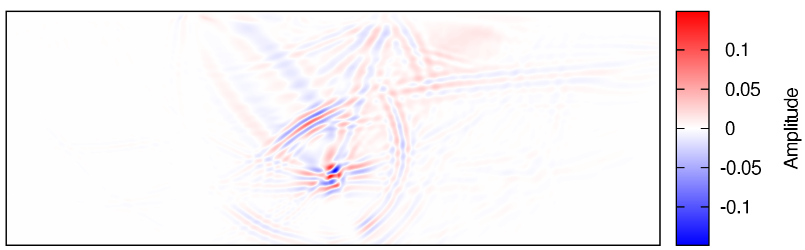

(c) HV

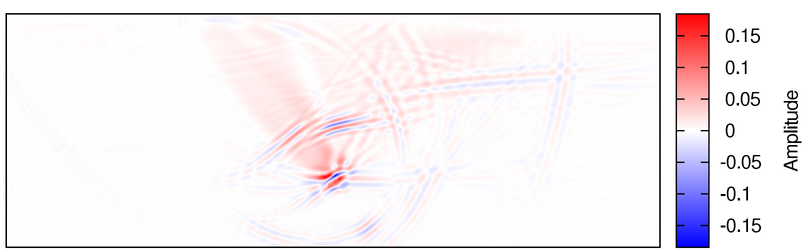

(d) HH

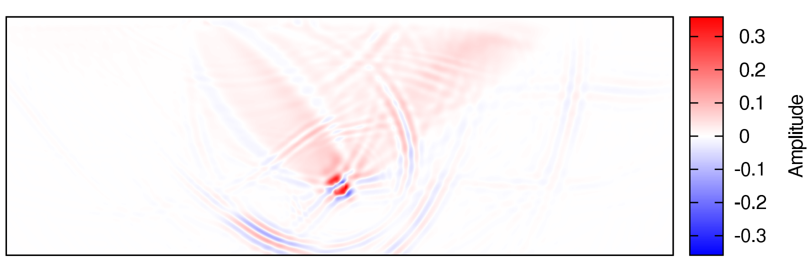

(e) Stack of above four images

Figure 4.10: Far-away source shot image with source energy normalization.

(Figure 4.7 and 4.8), the source wave energy, instead of one component of the wave, avoids the weak-source effect. In addition, the source energy normalized imaging conditions result in images with higher signal-to-noise ratio which can be easily recognized.

All the four multi-component imaging conditions in Equations 4.10 images the point reflector to some extent, while each of them has its own characteristics. First, generally speaking, the imaging quality of imaging condition in Equation 4.10a (VV imaging condition), which is resulted from the use of the vertical component of source wavefield and the vertical component receiver wavefield, is the best (Figure 4.9a and 4.10a). Second, imaging condition in Equations 4.10a and 4.10d (HH imaging condition) result in relatively higher vertical resolution than horizontal one, while imaging conditions in Equations 4.10b (VH imaging condition) and 4.10c (HV imaging condition) result in higher horizontal resolution than vertical one. Some researchers, such as Du et al. (2012), try some techniques to apply polarity reversal correction in imaging conditions. In my point of view, that correction hurts the image resolution, especially the horizontal resolution. Third, for a near offset subsurface target (Figure 4.7), the VV and VH imaging conditions work significantly better than the HV and HH imaging conditions, while for a far offset target (Figure 4.8), the HV and HH imaging conditions work not as bad as in the near offset case.

Imaging condition in Equation 4.11 (stacking imaging condition) results in even better image quality (Figure 4.9e and 4.10e). First, the overall imaging energy is the highest and the highest amplitudes are more focused on the point reflector better (see the legends in Figure 4.9 and 4.11, in which the highest amplitudes are the clip amplitudes). Second, the stacked images show both higher vertical and horizontal resolutions than all the other imaging conditions do.

4.3.4 Stacking shot images

The above discussion was about shot gather reverse-time migration. Eventually, stacking shot images results in a final image of the prestack reverse-time migration algorithm.

Figure 4.11 shows the stacked images of VV, VH, HV, and HH images from 27 shots, and the stack of the four stacked images.

4.4 Reverse-time extrapolation: shrunk Marmousi2

4.4.1 Marmousi, Marmousi2, and shrunk Marmousi2

There are two Marmousi subsurface models available in the literature.

The first one, Marmousi, was created by the Institut Francais du Petrole in 1988, based on a true geological profile. This is an isotropic heterogeneous acoustic model, with P-wave velocity profile only.

The second one, Marmousi2, was generated by the Allied Geophysical Laboratory at the University of Houston (Martin, 2004; Martin et al., 2006). It was based on the original Marmousi model. As the original model, Marmousi2 is isotropic and heterogeneous. However, Marmousi2 is elastic, profiled with not only P-wave velocities, but also S-wave velocities and densities.

In addition to the new elastic attribute, Marmousi2 is more complicated than the original Marmousi model. Geologically Marmousi2 is richer than Marmousi. Geometrically Marmousi2 is bigger. The lateral distance of the model is extended from the

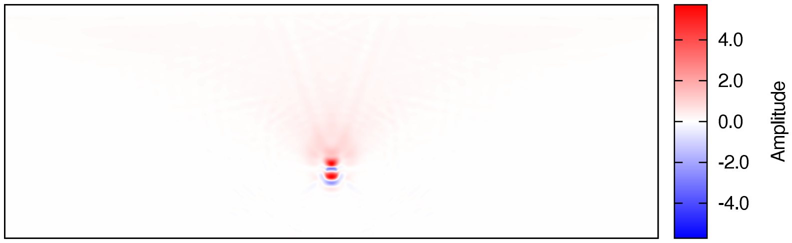

(a) VV

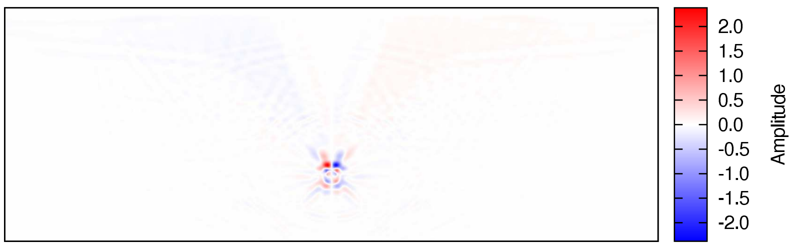

(b) VH

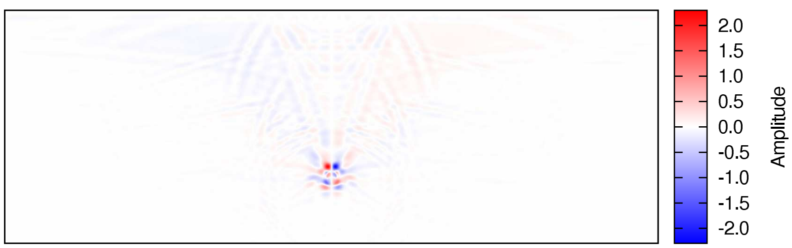

(c) HV

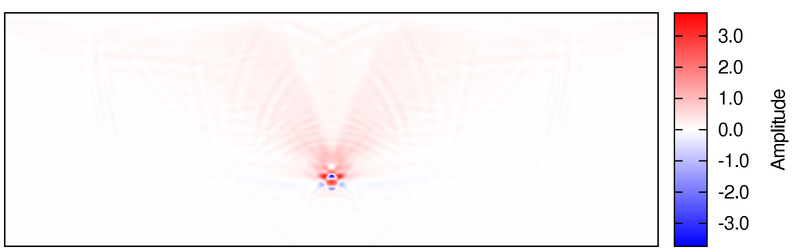

(d) HH

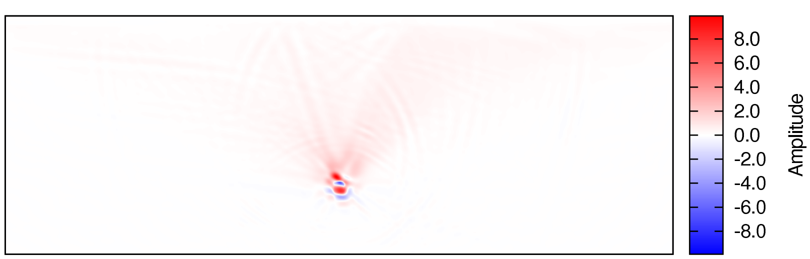

(e) Stack of above four images

Figure 4.11: Stacked image from 27 shot gathers, with source energy normalization.

original 9.2km to 17km, and the depth is extended from the original 3km to 3.5km.

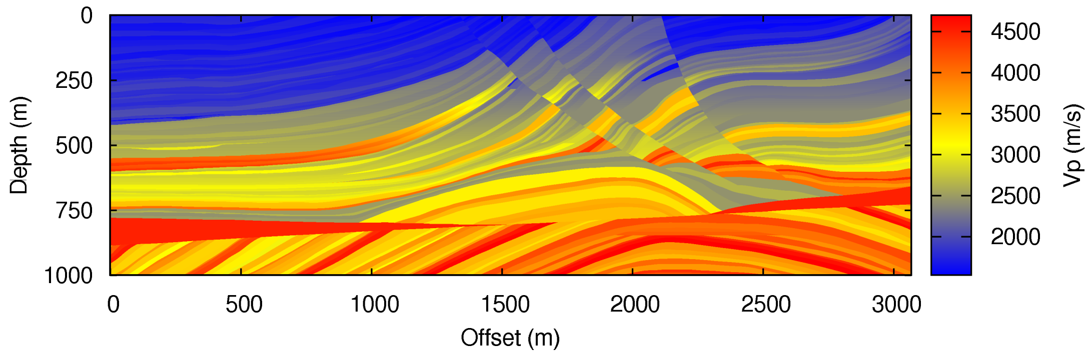

(a) P-wave velocity

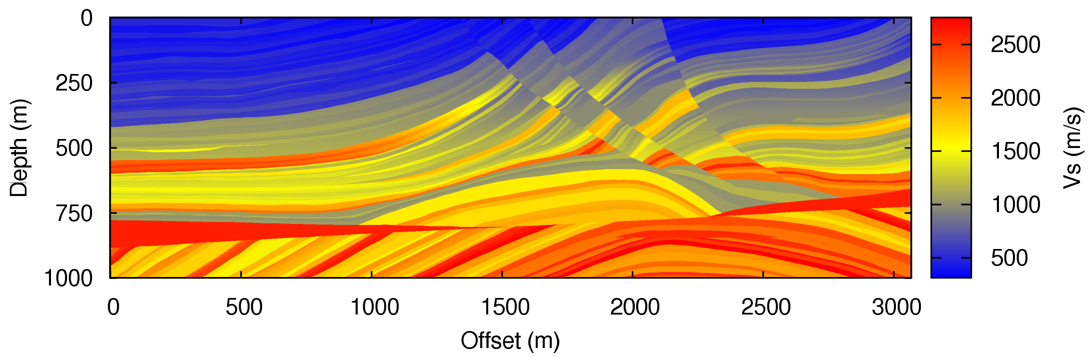

(b) S-wave velocity

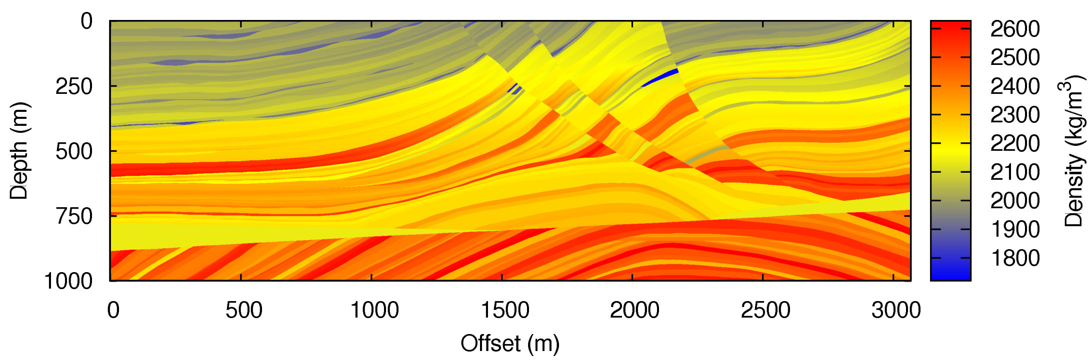

(c) Density

Figure 4.12: A new elastic Marmousi model cut and shrunk from Marmousi2.

I extracted part of Marmousi2 and shrunk it to create a much smaller subsurface model. There are 13601 horizontal nodes and 2801 vertical nodes in Marmousi2. First, the part from the grid node (3201, 405) to (10560, 2800) of the Marmousi2 model is extracted to obtain the structure. Note that the water layer is removed by this step. Then, one node from every three in both horizontal and vertical direction is extracted to obtain a down-sized Marmousi model. Now the new model has a grid of 2453×798 nodes, with a lateral length of $2066.25m$ and a depth of $997.5m$. Thus, the shrunk Marmousi model (Figure 4.12) keeps the complex structures of Marmousi2 model, but its size is much smaller, which has the advantage of less computational cost. However, with rock layers being shrunk to one third of the original thickness, it is more difficult to image.

Table 4.1: Wave velocity and density range of the shrunk Marmousi2 model.

Property	Low limit	High limit
P-wave velocity (m/s)	1530.56	4700.00
S-wave velocity (m/s)	311.53	2752.00
Density (kg/m^2)	1720.00	2627.00

Table 4.1 shows the rock property ranges for the new model. The low velocity and low density 'layers' are mainly at the shallow subsurface. These property set of P- and S- wave velocities and densities are translated to the property set of Lamé constants and densities when used in my finite-difference computing, as described in Chapter 2.

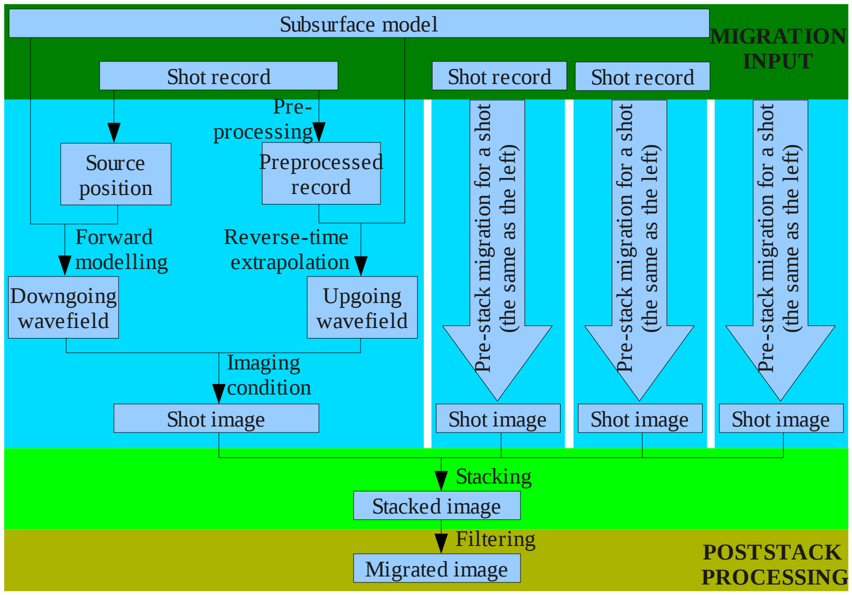

Figure 4.13: Prestack reverse-time migration workflow.

4.4.2 Prestack reverse-time migration workflow

There are four main steps in the prestack reverse-time migration workflow for the shrunk Marmousi2 model, as shown in Figure 4.13.

Input data for migration

The first step is to acquire surface records and to build subsurface model. In a real seismic survey, surface records are acquired from seismic surveys, and a subsurface model can be built from well logs, velocity analysis from surface record, full waveform inversion, and so on. In my numerical experiment, the subsurface model is the shrunk Marmousi2 model, and the surface record is acquired from wave modelling using the shrunk Marmousi2 model.

Figure 4.14 shows vertical component of some selected snapshots of centre shot modelling. The seismic source is put at the lateral distance of $1500m$, i.e. 1200^{th}

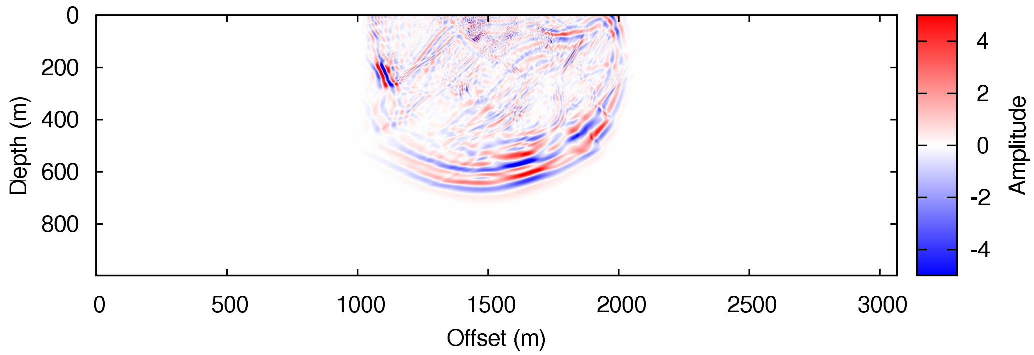

(a) t=0.30s, vertical component

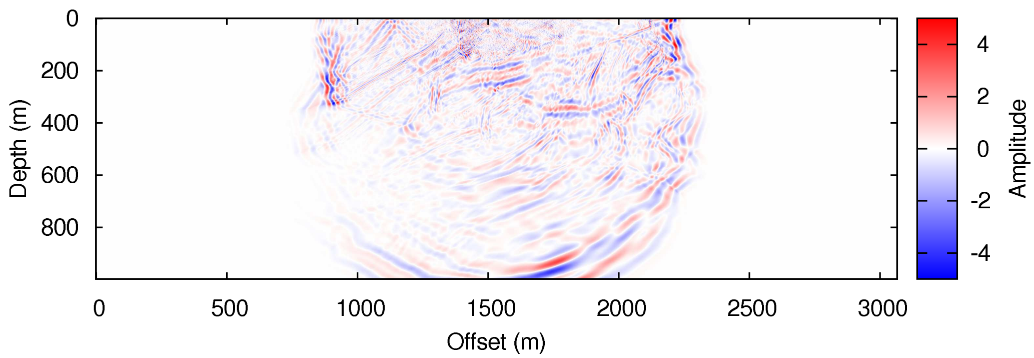

(b) t=0.42s, vertical component

Figure 4.14: Selected centre shot snapshots of shrunk Marmousi2: vertical component.

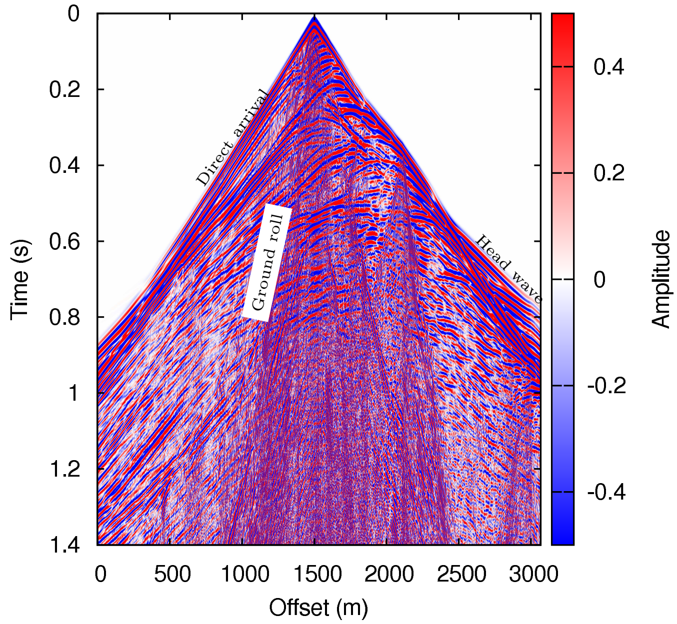

(a) Shot record - vertical component

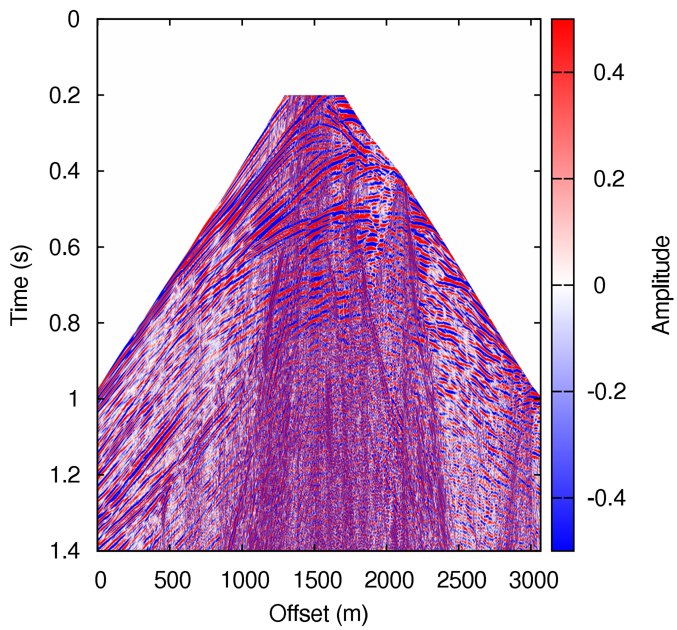

(b) Muted record - vertical component

Figure 4.15: Centre shot record of shrunk Marmousi2 [to be continued].

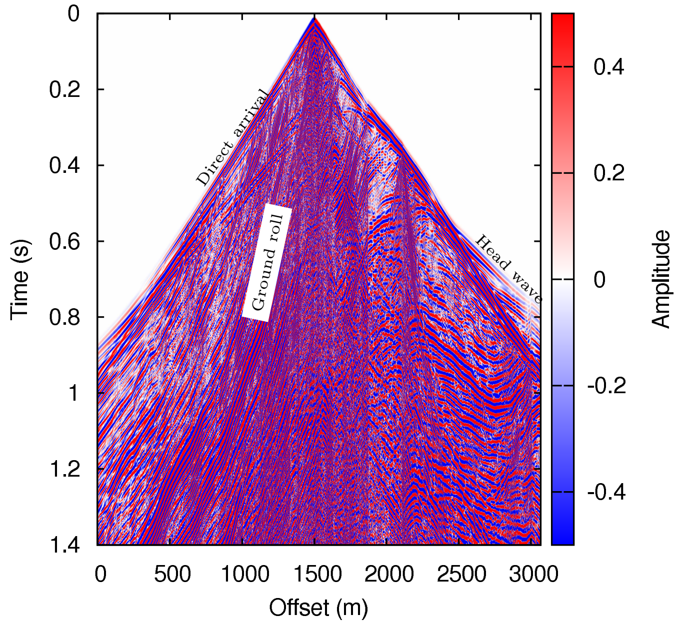

(c) Shot record - horizontal component

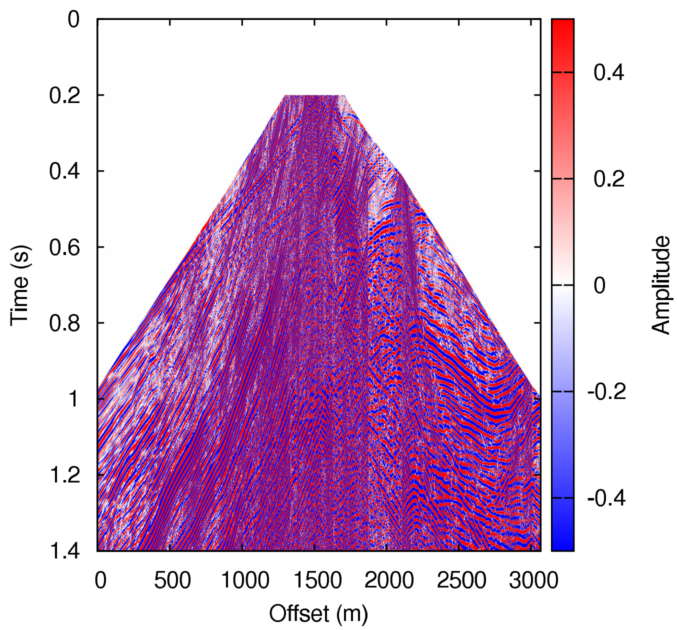

(d) Muted record - horizontal component

Figure 4.15: [Continued]

lateral node, close to the centre of the surface, and at the depth of $12.5m$, i.e. the 10^{th} node in depth. Due to the complex subsurface structure, it is difficult to interpret the wavefronts in the snapshots, as described for the point reflector modelling. However, one still is able to interpret some wave phenomena. For example, wave front in the depth direction travels faster than in the lateral direction; wave front in the right travels much faster than the part in the left; shear waves and Rayleigh waves are much slower and weaker than the P waves. All these wave phenomena are consistent with the subsurface model (Figure 4.12).

It is easy to recognize some common events from the surface records. Figure 4.15a and 4.15c show, respectively, the vertical and horizontal components of centre shot. First arrivals are direct waves and head waves. Hyperbolas are caused by reflectors in the subsurface. Ground roll travels at lower velocities, cutting through the hyperbolas in the time record.

Shot record reverse-time migration

The second step is reverse-time migration of shot records, which contains forward modelling, reverse-time extrapolation of surface records, and applying imaging conditions.

Muting ground roll here is not critical for reverse-time migration of the shrunk Marmousi2 model. There are three reasons. First, the ground roll energy will only affect the migration of near surface part. Second, ground roll in shot images will cancel each other in the next step, stacking. Third, the ground roll energy for the shrunk Marmousi2 model is relatively weak, due to the fact that the shallow part of the subsurface has very low S-wave velocities. Thus, the preprocessing of the surface record for reverse-time extrapolation is muting direct arrivals and head waves without getting rid of the ground roll in surface records (Figure 4.15b). This is different from the preprocessing for the point reflector model in Section 4.2, where direct arrivals, head waves, and ground roll are all muted.

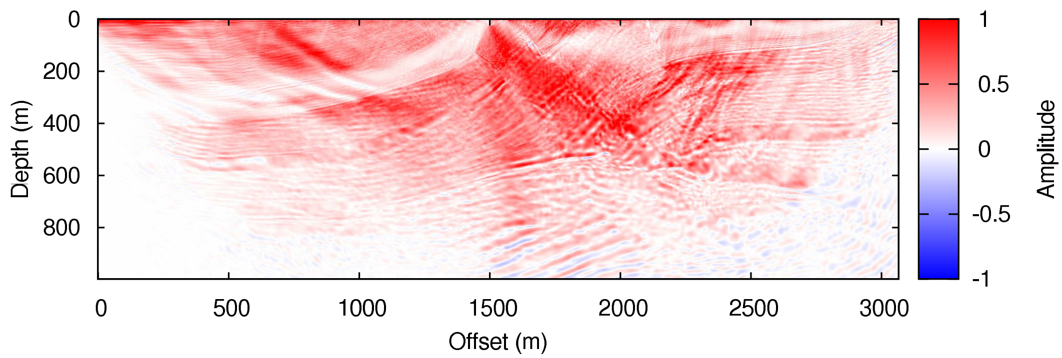

Figure 4.16: Centre shot migration of shrunk Marmousi2. Imaging conditions of Equation 4.11 are applied.

The centre shot image (Figure 4.16) shows subsurface structures with significant imaging artifacts. First, image amplitudes are mostly positive values, and the overall amplitude of the upper part is higher than the bottom part. It is not surprising that stacking of shot images will have the same feature. Second, the bottom-left and bottom-right corners are not imaged or poorly imaged. This is reasonable since seismic reflections from those parts can barely reach the surface receivers. If the seismic source is put close to the left part of the surface, one can expect the image of the bottom-left corner will be improved. It is the same with the bottom-right corner. In addition to the above two features, there is some other imaging artifacts, which might be the results of poor preprocessing of the surface record before reverse-time extrapolation. For example, the rough process of muting might be one of the causes.

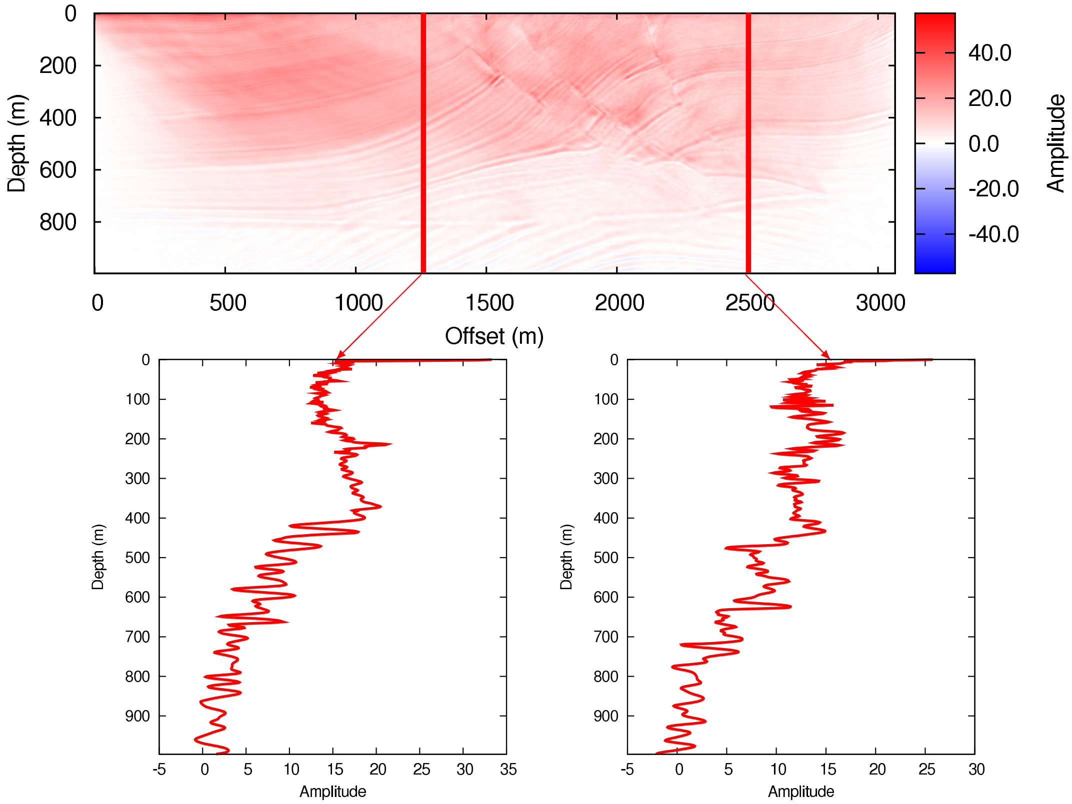

Figure 4.17: Stacked reverse-time migration image of shrunk Marmousi2. It is the stack of 49 shot images.

Stacking of shot images

The third step is stacking shot images obtained from the second step. The stack process improves signal-to-noise ratio, similar to the processing of CDP stacking.

The image shown in Figure 4.17 is the stacking result of 49 shots. Seismic sources are placed at lateral 50^{th} to 2450^{th} finite-difference nodes, with distances being 50 nodes. Imaging conditions of Equation 4.11 are applied.

Compared to the centre shot image, the areas close to bottom-left and bottom-right corners are better imaged. Also the subsurface structures are clearer, indicating a higher signal-to-noise ratio.

As shown in the two 'trace' wiggle plots, the upper part amplitudes are higher than those of the lower part. This has the effect that the signals of reflectivity appear riding on the low frequency artifacts.

Poststack processing - highpass filtering

A fourth step of poststack processing, applying a highpass filter on the stacked image to remove the very low frequencies in the stacked image, is necessary.

There are many ways to reduce low frequencies. I have tried three of them.

The first method is subtracting neighborhood average values for each sample in the stacked image, since in a small window of neighborhood samples along the traces, the values appear like an AC signal rides on a DC bias. Along each trace of the data, for each sample, a certain length (for example, 50 samples) of window centered by this sample is defined. The average amplitude of the samples in the defined window is calculated, and then this value is subtracted from the central sample value. In this way, each sample value is reduced by the neighborhood averages.

The second method is taking first derivatives along the traces in the stacked image.

This method is often used within Kirchhoff migration (Bancroft, 2006).

The third method is filtering the stacked image using a high pass filter since the artifacts are the low frequencies. The lowest frequency (actually it should be called 'wavenumber') of the signals is estimated, by counting wave circle numbers from the traces shown on the bottom in Figure 4.17, as 0.028 wavenumber per metre. Thus, the cutoff frequency for the high pass FIR filter is decided to be 0.026 wavenumber per metre.

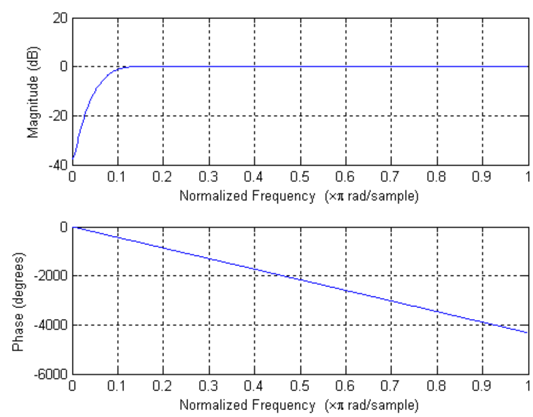

Figure 4.18: Frequency response of a high pass FIR filter, which is used to filter the stacked image.

Using MATLAB, a filter is designed, which is a Hamming-window based, linear phase, 48^{th} order finite impulse response (FIR) filter. Because the normalized cutoff frequency 1.0 corresponds to the Nyquist frequency of 0.4 wavenumber per metre (since the grid spacing is 1.25 m), and the cutoff frequency is decided to be 0.026 wavenumber per metre, the FIR filters normalized cutoff frequency is set to $0.026 \div$

$0.4 = 0.065$. Thus, the FIR filter coefficients are calculated in MATLAB by

$$h = FIR1(48, 0.065, `HIGH') \tag{4.12}$$

The resulting FIR filter coefficients are:

$$\begin{aligned} h(k) = \{&0.0010, 0.0012, 0.0013, 0.0016, 0.0018, 0.0020, 0.0019, 0.0016, 0.0008, \\ &-0.0006, -0.0027, -0.0055, -0.0091, -0.0135, -0.0187, -0.0244, -0.0305, \\ &-0.0369, -0.0431, -0.0491, -0.0544, -0.0588, -0.0622, -0.0642, 0.9341, \\ &-0.0642, -0.0622, -0.0588, -0.0544, -0.0491, -0.0431, -0.0369, -0.0305, \\ &-0.0244, -0.0187, -0.0135, -0.0091, -0.0055, -0.0027, -0.0006, 0.0008, \\ &0.0016, 0.0019, 0.0020, 0.0018, 0.0016, 0.0013, 0.0012, 0.0010\}. \end{aligned} \tag{4.13}$$

where k is the index of the coefficients. Then the traces in the stacked image are filtered by

$$y(n - \frac{K}{2}) = \sum_{k=0}^{K-1} h(k)x(n-k) \tag{4.14}$$

where x and y are, respectively, the input and output signals of the filter; n is the sample index in the trace; $K = 49$ is the length of the filter; $\frac{K}{2}$ is the group delay of the FIR filter.

The highpass filter method results in the best image. Figure 4.19e shows the filtered result of the stacked image in Figure 4.17.

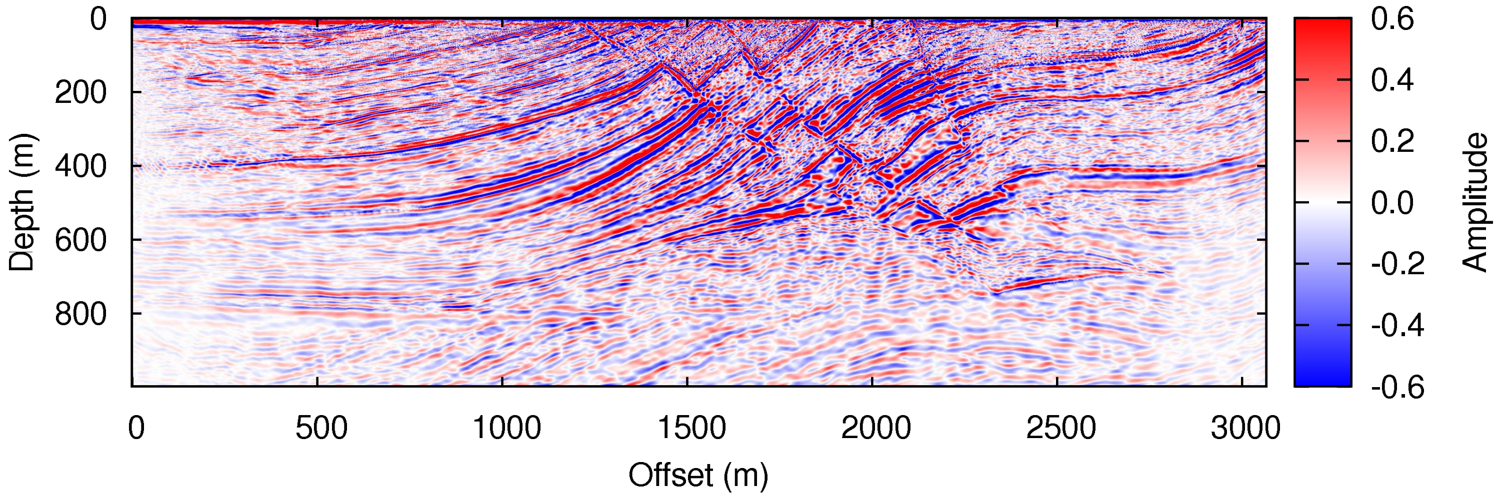

(a) HV

Figure 4.19: Migrated image for shrunk Marmousi2 [to be continued].

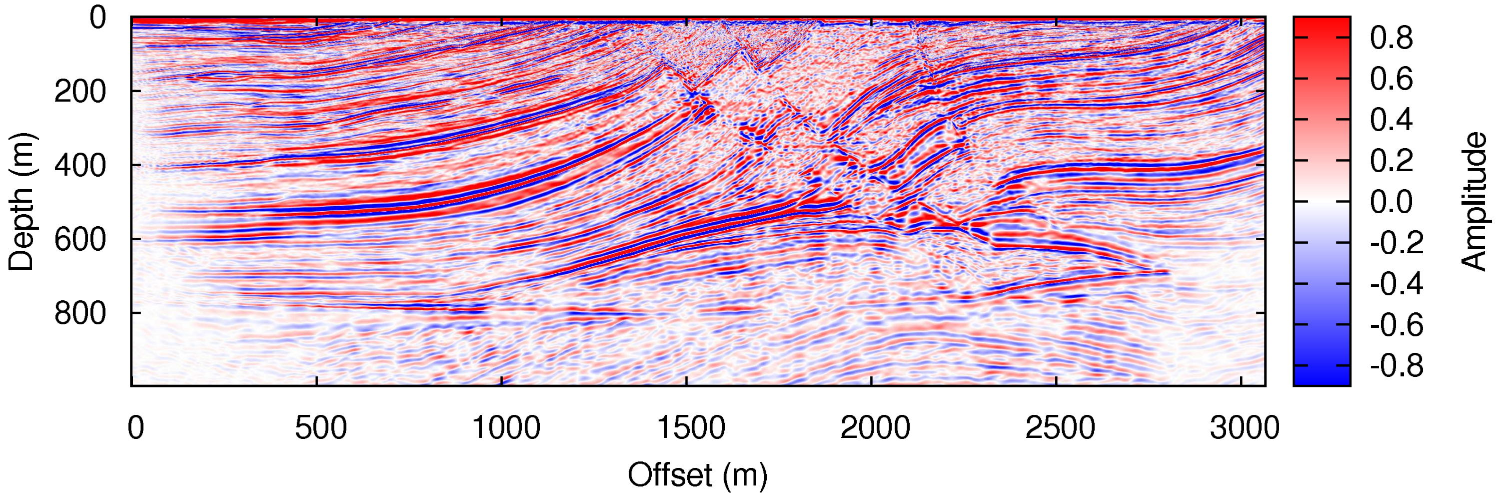

(b) HH

Figure 4.19: [to be continued]

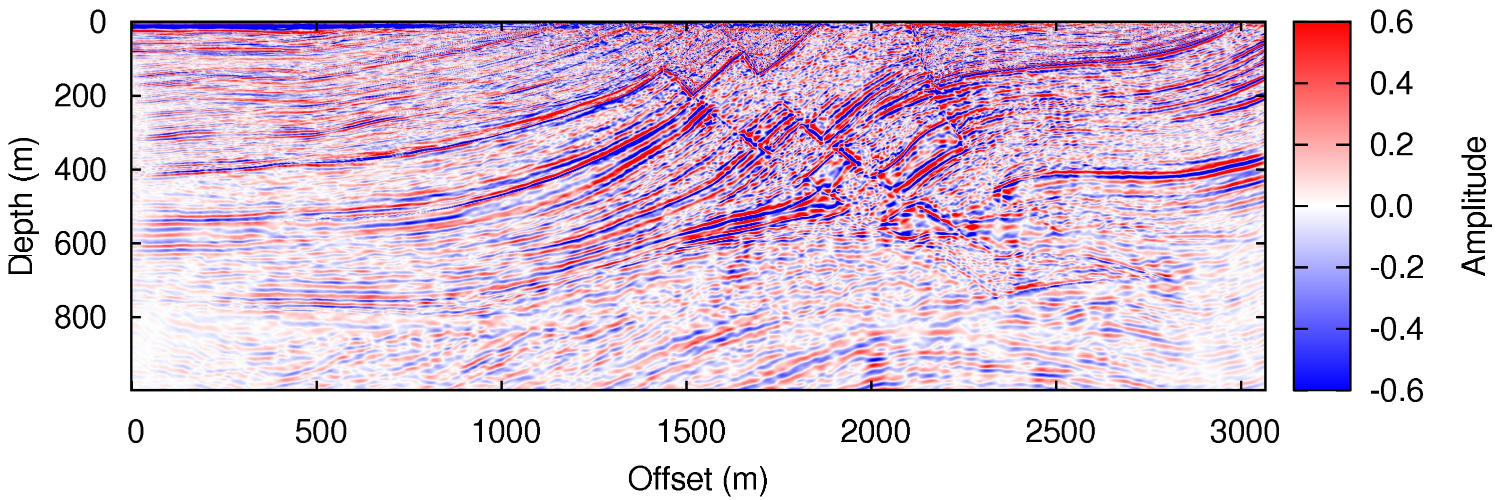

(c) VH

Figure 4.19: [to be continued]

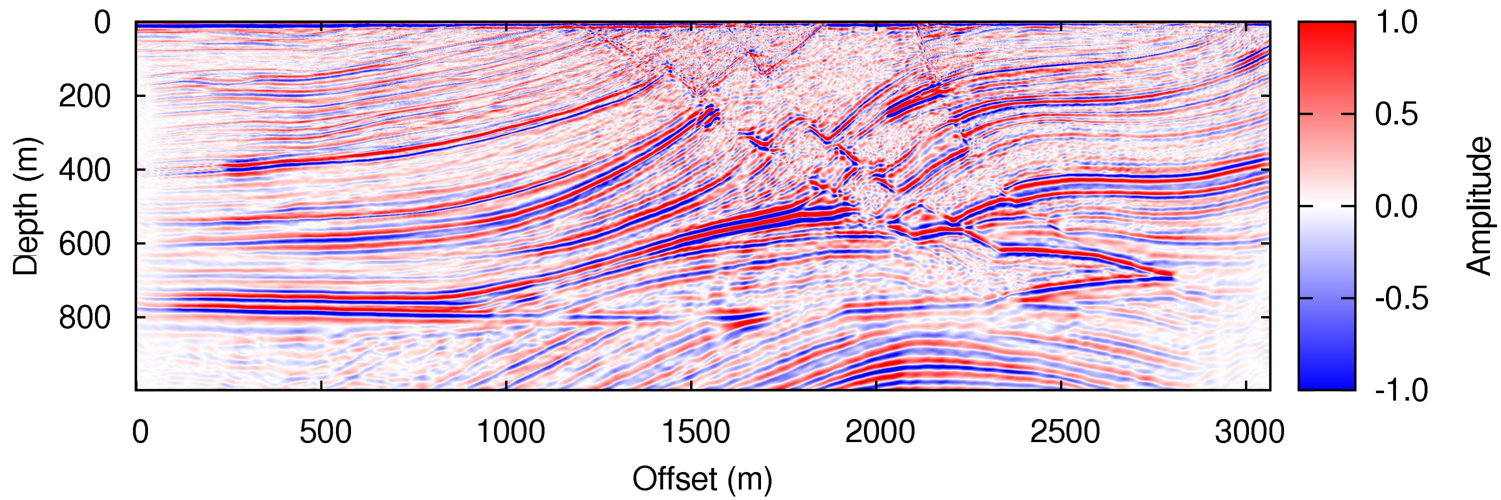

(d) VV

Figure 4.19: [to be continued]

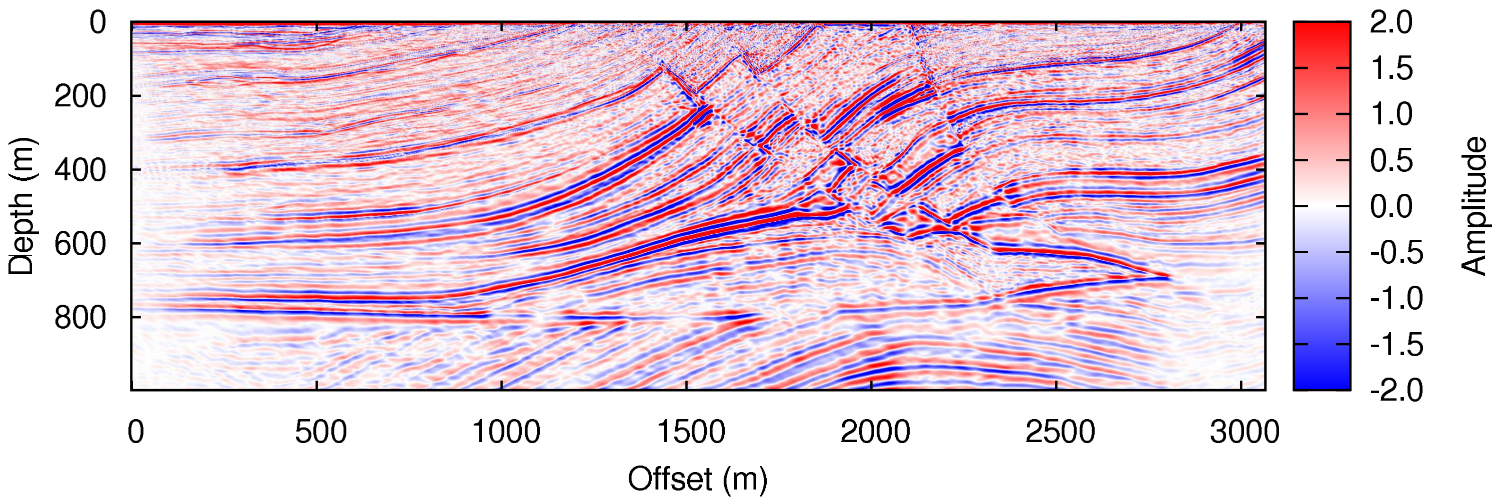

(e) Stack of above images

Figure 4.19: [Continued]

4.4.3 Migration results

Figure 4.19 shows results of the multicomponent prestack reverse-time migration of the shrunk Marmousi2. They are obtained by the workflow described in subsection 4.4.2. The only difference between the images shown in Figure 4.19 are imaging conditions. Each of the images corresponds to one of the source energy normalized imaging conditions in Equation 4.10 or 4.11.

Depth penetration and Resolution

The migrated images show different features, in terms of depths of penetration and resolutions. These features are connected to the imaging conditions applied.

Different imaging conditions provide different depths of penetration with the same input data and under the same processing workflow. The VV imaging condition (Equation 4.10a, see Figure 4.19d) provides the deepest depth of penetration among the first four imaging conditions. This is reasonable: usually P waves are the main contributers to the vertical component in seismic surveys, and with faster velocities they covers deeper depth.

Different imaging conditions provide different resolution of the subsurface geology in both the vertical and horizontal dimensions. Resolution is a measure of the ability to recognize individual, closely spaced reflectors. It is judged by image amplitudes and their continuity of the subsurface interfaces in the migrated images. In this sense, Figure 4.19d and 4.19b show better vertical resolutions than Figure 4.19c and 4.19a, while the latter two images show better horizontal resolutions. That is, the VV and HH imaging conditions provide better vertical resolutions, while the VH and HV imaging conditions provide better horizontal resolutions.

Figure 4.19e, which is the stack of Figure 4.19a, 4.19b, 4.19c, and 4.19d, shows the best image. First, it shows the deepest depth of penetration. Second, it shows the best resolution in both the vertical and horizontal dimensions. And third, as a result, it shows the highest signal-to-noise ratio overall. Thus, the stacking imaging condition is the best in all of the five proposed source energy normalized imaging conditions.

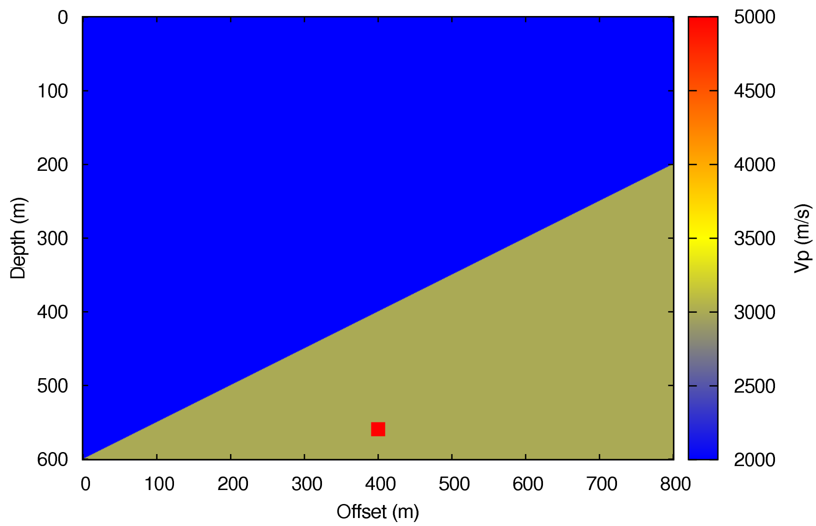

Figure 4.20: A P-wave velocity model with lateral velocity variation.

4.5 Migration of a dipping-layer model

Black and Brzostowski (1994) described time migration errors and provided formulas to calculate those errors (Section 1.1.2). This section shows some modelling and reverse-time migration results using a dipping-layer model that is similar to the one described by Black and Brzostowski (1994).

A dipping-layer model in Figure 4.20 is a model with lateral velocity variations.

It contains three media: a medium with lower P-wave velocity ($2000m/s$) sits on top of a medium with higher P-wave velocity ($3000m/s$), and there is a diffractor (P-wave velocity is $5000m/s$) in the bottom layer, positioned at the horizontal centre. Supposing Poisson's ratio to be 0.45, one can estimate the S-wave velocities and densities by the same method used in subsection 2.5.2.1.

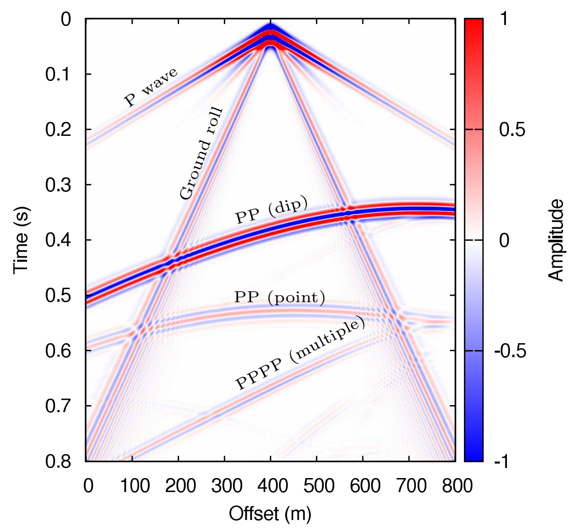

Figure 4.21: Centre shot record (vertical component) of the dipping-layer model shown in Figure 4.20. 'PP (dip)' is the P-wave reflection of the dip event, 'PP (point)' is the reflection of the point reflector, and 'PPPP (multiple)' is the multiple caused by the dip event and the free surface.

With time migration, the diffractor will be migrated upward and to the right of the real position (Figure 1.3). Why will this happen? The reason is that the lateral velocity variations above the point diffractor shifted the apex of the point diffractor hyperbola to the right, even though the diffractor itself is at the lateral centre of the model (Black and Brzostowski, 1994). One can confirm the apex shift by ray tracing, or by checking the modelled surface record shown in Figure 4.21.

Figure 4.21 is the vertical component of the centre shot record modelled from the dipping-layer model shown in Figure 4.20. In addition to P waves and ground roll, the main reflections in the surface record are (1) P-wave reflection of the source P wave from the dip event, annotated as 'PP (dip)' in the figure, (2) P-wave reflection of the source P wave from the point reflector, annotated as 'PP (point)', (3) P-wave multiple caused by the dip event and the free surface, annotated as 'PPPP (multiple)'.

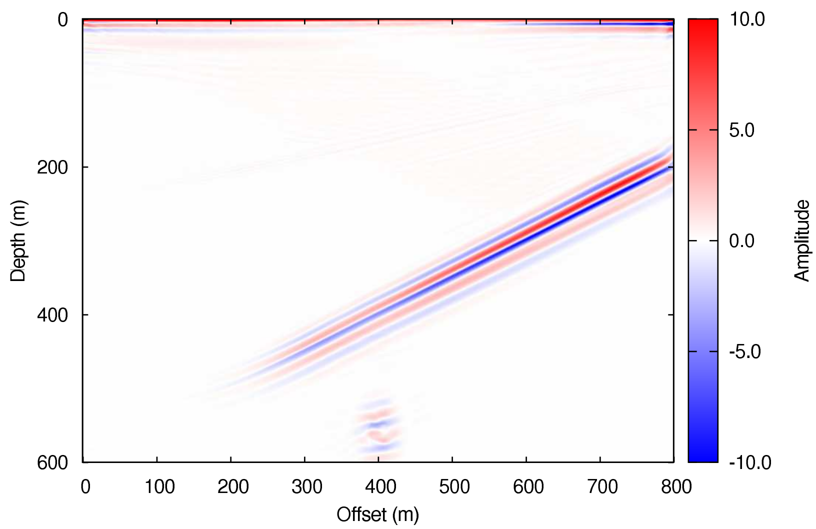

Figure 4.22: Reverse-time migration of the dipping-layer model shown in Figure 4.20.

With reverse-time migration, the diffractor can be correctly imaged (Figure 4.22). The migration workflow is similar to the one described in section 4.4.2.

4.6 Chapter summary

The reverse-time migration demonstrated in this chapter has three new features.

First, it employs a staggered-grid finite-difference scheme. The potential benefit is that the method will handle solid-liquid boundaries more accurately. Potential, this is a big advantage for Ocean-Bottom Seismic (OBS) data processing.

Second, an improved imaging condition for multicomponent imaging, so-called 'source energy normalized imaging condition', is proposed. The imaging condition suppresses both strong-source effect and weak-source effect of some other imaging conditions.

Third, it was found that ground roll suppression is not critical for reverse-time migration at all. This was proved by the shrunk Marmousi2 migration experiment - water layer was removed, so strong ground roll was generated. Hence, the procedure of noise attenuation in reverse-time migration may be able to exclude ground roll suppression.

Chapter 5

Computational resources

Prestack reverse-time migration is computationally expensive, which is a drawback for applying the migration method.

Program run times are long, in terms of the total number of CPU cycles, and it requires large amounts of hard disk free space. To accelerate computing, parallel computing is employed. Intel® Threading Building Blocks (TBB) and multi-core computers, are used for both the forward-time modelling and reverse-time migration phases of the computation. To solve the problem of limited free disk space, the forward modelling phase is conducted twice instead of once, which may seem counter-intuitive.

Two other enduring problems are described at the end of the paper: the requirement for large working memory, and limited access speeds of mass storage (hard disk) compared to the speed of computation in RAM memory.

5.1 Computational time

Elastic wave modelling based on finite-difference methods is time consuming. For example, it took Martin (2004) a total of 70,000 hours, or approximately 8 CPU years to do elastic wave modelling using the Marmousi2 model.

Prestack reverse-time migration based on finite-difference methods needs an even longer computational time. As described later in this chapter, the migration of one shot needs two forward modelling steps and one reverse-time extrapolation. Thus, it will take about 24 CPU years to migrate Marmousi2 data by the same hardware and software.

One of the solutions to the CPU intensiveness problem is parallel computing. Although both a distributed parallel computing technique, which uses multiple computers or a cluster computer, and a multi-core/multi-processor parallel computing technique, which uses a single computer with many CPU cores/threads are available, the author only used the latter for the computations in the dissertation.

5.1.1 Hardware for parallel computing: multi-core computers

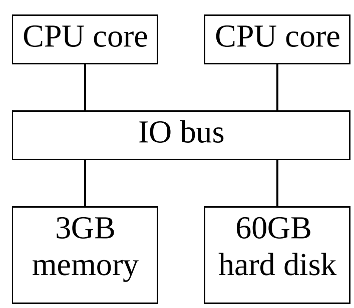

Figure 5.1: The logical architecture of the dual-core Lenovo R60e notebook computer.

My first parallel computing experiment was carried out on a dual-core PC. This is a Lenovo R60e notebook computer, which has an Intel® core 2 CPU (1.83 GHz) and 3 GB memory. The Intel® core 2 CPU has two CPU cores, which can be employed to do parallel computing. The logical architecture of the computer is shown schematically in Figure 1.4.

Multi-core parallel computing can also be done on cluster computers. Some nodes

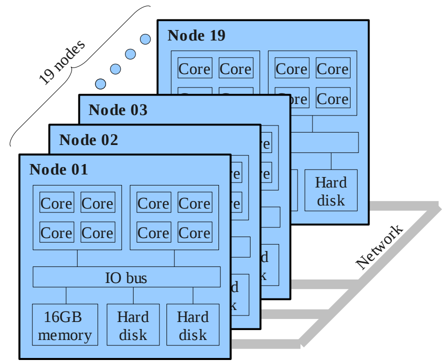

Figure 5.2: The logical architecture of the cluster computer Gilgamesh (adopted from Bonham et al. (2008).

on a cluster computer, called Gilgamesh, at the Consortium for Research in Elastic Wave Exploration Seismology (CREWES), are used to do most of the reverse-time migration computing for this study. There are totally 19 nodes on Gilgamesh (Figure 5.2). Each node of Gilgamesh is based on the Super Micro X7DVL-E system, with two Intel® Harpertown 2.66 GHz quad-core processors. The logical architecture of the Gilgamesh node is similar to that of the dual-core PC, except that the number of cores is 8 instead of 2, the RAM memory size is 16 GB instead of 3 GB, and the total space of 2 hard disks is 320 GB (Bonham et al., 2008).

5.1.2 Software: Intel® TBB

Intel® TBB is used to parallelize the modelling and reverse-time migration application. Intel® TBB is a C++ template library for writing software programs that take advantage of multi-core processors. There are two builds of it: commercial build and open source build. According to the website of Intel®, there are no differences between those versions except standard commercial support for the purchased version of TBB. The open source build is used in the dissertation.

The advantages of Intel® TBB are obvious. First, it is a very efficient way to write parallel code for an experienced C/C++ programmer. An example of migrating serial code to parallel code is shown in the subsection 5.1.2.1. Second, since it is a software library, there are minimal requirements on programming language and compiler support. If a software application is written in pure C++, the application of Intel® TBB is straight forward, since the interface is in C++. If a software system is based on other languages, such as C or FORTRAN, the techniques of mixing program languages can be employed to build an interface between the custom software system and Intel®. Third, Intel® TBB is portable across Windows, Linux, Mac OS X, Solaris and many other operating systems, according to the documentation. In fact, I have used it on both Windows and Linux. Fourth, Intel® TBB can co-exist and inter-operate with other parallel methods. It is especially beneficial to inter-operate Intel® TBB with a distributed parallel computing system. For example, a very powerful practice is to use both socket parallel and Intel® TBB in an software application. With the use of a socket, computing tasks can be sent to different computers as child processes; with the use of Intel® TBB in child processes, the child processes will be able to take advantage of all of the CPU cores on each specified computer on a local network.

5.1.2.1 An example of migration serial code to parallel code

The following is a simple example of migrating a piece of serial code to parallel code. The code shown here is from my C++ template class CMatrixT, which carries out matrix operations.

A simplified serial version of adding up two matrices by elements is shown in Program 1.

Program 1 Adding up two matrices element by element - serial version.

```
template <typename T>
CMatrixT<T>& CMatrixT<T>::operator +=(const CMatrixT &in_matrix)
{
  int i,j;
  // m_nD1 and m_nD2: dimensions of the matrices
  // m_entry: a 2D array
  for(i=0; i<m_nD1; i++)
    for(j=0; j<m_nD2; j++)
      m_entry[i][j] += in_matrix.m_entry[i][j];

  return *this;
}
```

A parallel version of the program is shown in Program 2. First, the function is migrated to use *parallel_for* to indicate that the computing task will be parallely finished by a C++ class *CPlusByElement*. Second, a C++ class *CPlusByElement* is written to carry out the computation. The core of the C++ class code is very similar to the serial code: two loops control the scan of matrices. The difference is the outside loop range.

5.1.3 Efficiency of parallelization and Amdahl's law

The efficiency of parallelization was first tested on the dual-core PC mentionsed above. A simplified model, which contains 872 nodes in the x_1 direction and 366 nodes in the x_3 direction, is used in reverse-time migration. For 10 shots, the parallelized program employs the dual-core CPU and the total computation time is reduced by 44.7%, i.e., the speedup is 180.69% (Figure 5.3).

A modelling program was then tested on a Gilgamesh node with eight CPU cores. The subsurface model contains 3000 nodes in the x_1 direction and 800 nodes in the

Program 2 Adding up two matrices element by element - parallel version.

```
template <typename T>
CMatrixT<T>& CMatrixT<T>::operator +=(const CMatrixT &in_matrix)
{
  #ifdef USETBB   // parallel
    tbb::parallel_for( tbb::blocked_range<int>(0, m_nD1),
      CPlusByElement<float>(*this, in_matrix) );
  #else           // serial
    int i,j;
    for(i=0; i<m_nD1; i++)
      for(j=0; j<m_nD2; j++)
        m_entry[i][j] += in_matrix.m_entry[i][j];
  #endif

  return *this;
}

template <typename T>
class CPlusByElement
{
  private:
    CMatrixT<T>& m_in1;
    const CMatrixT<T>& m_in2;

  public:
    CPlusByElement(CMatrixT<T> & in1, const CMatrixT<T> & in2)
    :m_in1(in1),m_in2(in2) {}

    void operator()(const tbb::blocked_range<int>& range) const
    {
      int i,j;
      for(i=range.begin(); i<range.end(); i++)
        for(j=0; j<m_in1.getD2Size(); j++)
            m_in1(i,j) += m_in2(i,j);
    }
};
```

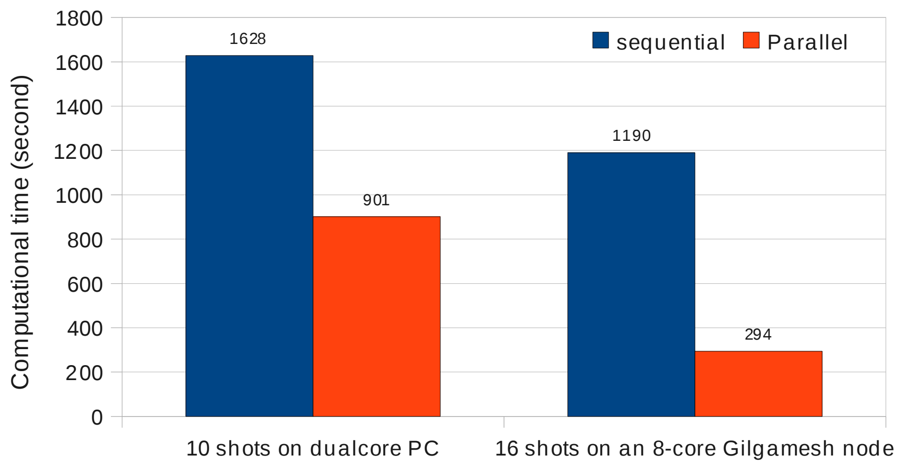

Figure 5.3: Computational efficiency with and without parallel computing.

x_3 direction. For 16 shots, the parallelized program employs the eight CPU cores and the total computation time is reduced by 75.3%, i.e., the speedup is 404.76% (Figure 5.3).

The computational efficiency gets improved more when there are more CPUs available. However, the improvement is not exactly proportional to the number of available CPUs. This is consistent with Amdahl's law, though.

Amdahl's law can be used to predict the speedup by parallel computing (Amdahl, 1967; Wikipedia, 2012). Suppose P is the paralleled proportion of a job in which N CPU cores are used. The speedup that can be achieved is

$$Speedup(N) = \frac{1}{(1-P) + \frac{P}{N}}, \tag{5.1}$$

where $1 - P$ is interpreted as the proportion of the job that remains in serial, and $\frac{P}{N}$ is interpreted as the speedup of the paralleled proportion of the job which uses N CPU cores. For example, if 50% of a job is parallelized by 2 CPU cores, the expected

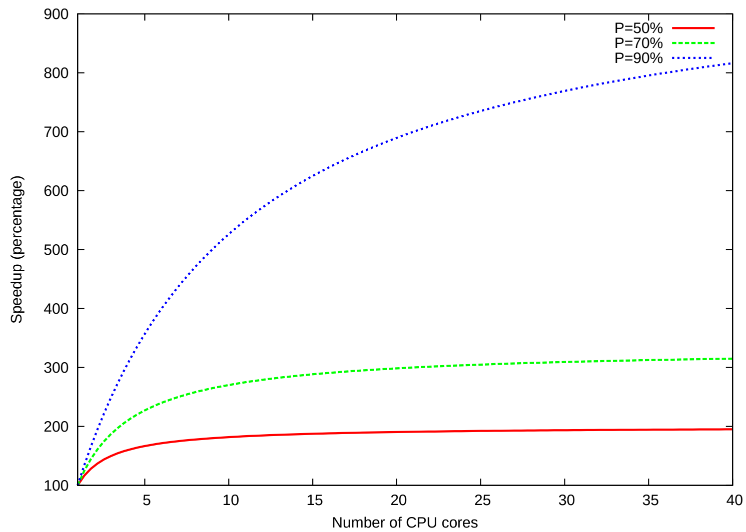

Figure 5.4: Amdahl's law, adopted from Wikipedia (2012). 'P' indicates paralleled proportion of a job.

speedup is 133.33% (Figure 5.4).

Some parts of my programs, like any other programs, cannot or are difficult to be parallelized. For example, disk I/O, including reading in subsurface model, reading and writing temporary processing data, writing the final results, and so on, is impossible to be parallelized. Thus, the speedup is impossible to be proportional to the number of CPU cores.

5.2 Disk space

The problem of limited hard disk free space arises when one tries to calculate cross-correlation imaging conditions (such as Equations 4.7, 4.9, and 4.10). Take the simpler acoustic imaging condition for example,

$$Image(x_1, x_3) = \sum_t S(x_1, x_3, t)R(x_1, x_3, t), \tag{5.2}$$

where $S(x_1, x_3, t)$ and $R(x_1, x_3, t)$ are , respectively, the source wavefield produced by modelling and the receiver wavefield produced by reverse-time extrapolation. Imagine that we have decided that we should compute the forward modelling by time steps $t = [1, 2, 3, ..., T-2, T-1, T]$. When we reach the last time T, we begin the reverse-time migration phase by time steps $t = [T, T-1, T-2, ..., 3, 2, 1]$. At each step t in the reverse-time calculation, the imaging condition requires cross-correlation with the corresponding t in the forward time calculation. This means stepping backward through the snapshots of the wavefield representation, which had been previously computed in the forward direction. Unfortunately, the disk space required to store every step in the forward calculation, would be prohibitive.

Take Marmousi2 model, which has a grid of 13601×2801 nodes, for example. Suppose it is padded with 150 nodes on both sides and on the bottom, it has a size of 13901×2951 nodes. To store the vertical component of one snapshot, one needs at least 164,087,404 bytes, i.e., approximately 156MB. For 5-second modelling time of a time step $100ms$, one needs free disk space of about 7,800TB. For a 2-component migration, the disk space requirement is doubled.

Even for the size-shrunk model used in this dissertation, the disk space requirement is still huge, if one needs to store every snapshot in the forward modelling. The shrunk model has a size of 2453×798 nodes. With padding, the size is increased to 2753. To store 1.2-second modelling snapshots of a time step $100ms$, one needs disk

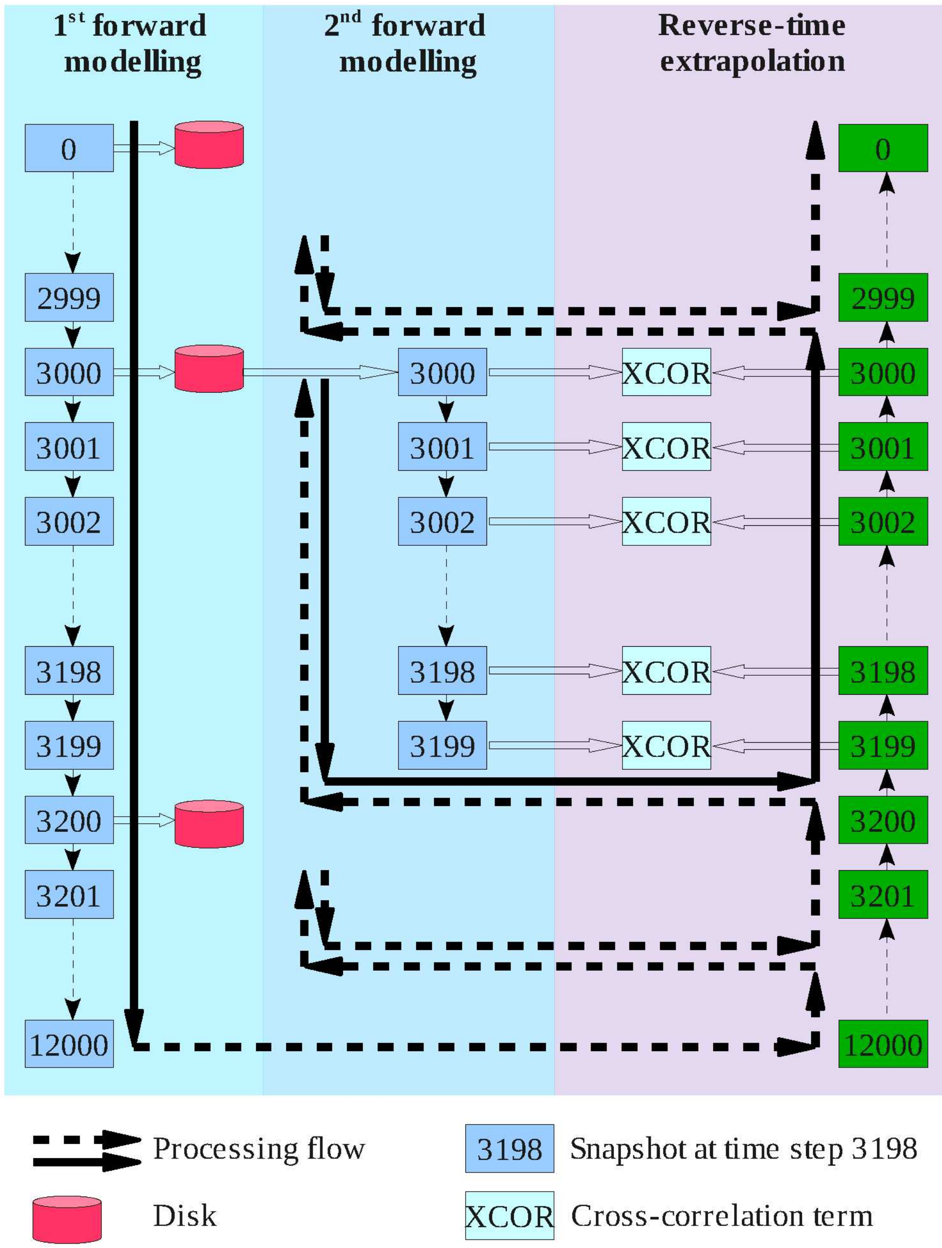

Figure 5.5: Modelling twice instead of once, to keep the disk space requirements within available limits.

The solution to the disk space challenge can be to use CPU time, doing modelling twice instead of once, to keep the disk space requirements within available limits. Modelling and reverse-time extrapolation is done with a total of 12,000 time steps. During the first forward modelling phase, instead of saving to disk all the wavefield snapshots (subsurface particle horizontal and vertical velocities) for each time step $t = [1, 2, 3, ..., 11999, 12000]$, one stores the wavefields (subsurface particle velocities and stresses) for only every 200^{th} time step, i.e., for $t = [200, 400, 600, ..., 11800]$. Computing backward in the reverse-time extrapolation, for $t = [12000, 11999, ..., 3, 2, 1]$, one can re-model each block of 200 snapshots from the stored wavefield state at the time it is needed for the cross-correlation. For example, when one has done reverse-time extrapolation of time 3200, one would re-model snapshots for time $t = [3001, 3002, 3003..., 3198, 3199]$ by reading the disk-stored wavefield state at time $t = 3000$, and re-modelling 200 time steps and keep the 400 snapshots (200 time steps, two components per time step) in memory. With the extrapolation in time-reversed order for time $t = [3199, 3198, ..., 3000]$, the re-modelled forward modelling snapshots are then used to do cross-correlation for those time steps (Figure 5.5). Thus, without storing all the modelling snapshots at every time step onto disk, the imaging condition can be implemented, although the modelling has to be done twice.

5.3 Other computational cost problems

There also exist some other problems in addition to the computing time and free disk space challenges. Here the author describes two of them: memory requirements and the bottleneck of hard disk drive I/O speed.

5.3.1 Memory requirement

Reverse-time migration needs a large amount of memory. Take the famous elastic Marmousi2 model for example. The model has a grid. Thus, totally there are 38,096,401 nodes. For each node, 4 bytes are needed to store a data type float, which means 152,385,604 bytes for the matrix. The elastic model has 3 parameter matrices: densities, P-wave velocities, and S-wave velocities, which are used in a non-staggered grid finite-difference method, or densities and lamé coefficients, which are used in a staggered-grid scheme. So, to load the model, 457,156,812 bytes, i.e., approximately 436 MB of memory, is needed. To calculate finite-differences, 5 more parameter matrices (2 particle velocities and 3 stresses in the case of staggered-grid scheme) of the same size as the grid need to be loaded in memory for each of 2 successive time steps. So the memory needed for finite-difference is 1,523,856,040 bytes, i.e., more than 1,453 MB. Thus, the total memory requirement for forward modelling or reverse-time extrapolation is at least 1,981,012,852 bytes, i.e., more than 1,889 MB.

3D processing needs even more memory. Take 3D wave modelling system described by Equations (2.6.1) for example. There are totally 26 quantities involved in each unit cell. With the use of single-precision floating point numbers for a small grid of dimension $300 \times 300 \times 300$, the memory requirement is at least $300 \times 300 \times 300 \times 26 \times 4 = 2808000000$ bytes, i.e., more than 2.6GB, if all the subsurface model parameters and one time snapshot are loaded into the memory simultaneously.

5.3.2 Disk I/O operation

Another problem is disk input and output (disk I/O) operation. Sometimes disk I/O could be the bottleneck of parallel computing. There are two reasons why hard disk

I/O can be the bottleneck of parallel computing. First, hard disk I/O speed is much slower than memory I/O. Secondly, CPU cores on cluster computers compete with each other for writing to and reading from the same disks. When there is a lot of disk I/O, a whole cluster node, or even the whole system could be slowed down. In fact, I actually observed this phenomenon: when all the eight CPU cores are computing without disk I/O, the percentage of CPU usage shown by the utility top, is usually 800% or close to this number, i.e., all the eight cores are fully made use of; when the eight CPU cores need to do disk I/O, the percentage sometimes can be as low as 200, i.e., six of the eight CPU cores are waiting for the disks at that moment.

If we must process large amounts of seismic data, or we must do a lot of disk I/O for some reasons, we will have to learn new tricks to overcome this challenge.

5.4 Chapter summary

Computational bottlenecks could be CPU time, disk space, RAM memory, disk I/O efficiency, network efficiency, and so on. This chapter attacked the problems of CPU time and disk space.

Intel® Threading Building Blocks (TBB) is a technique of multi-core parallel computing. Computational times are measured from two simple experiments to evaluate the technique. Utilizing two cores in a notebook computer, the speedup of the computation is 180.69%. With eight cores on a node of a cluster computer, Gilgamesh, the speedup is 404.76%. The computational time can be further reduced by shortening the serial part of programs and by using more CPU cores. However, there is a speedup limitation of the parallel computing, as stated in Amdahl's law.

It is a powerful practice to inter-operate Intel® TBB with a distributed parallel computing technique: Intel® TBB makes use of CPU cores available on a computer, while a technique of distributed parallel computing makes use of available computers on a local network.

To solve the problem of limited free disk space in reverse-time migration, a technique that seems counter-intuitive is used: the forward modelling is conducted twice instead of once.

Chapter 6

Conclusions and future directions

6.1 Conclusions

Wave modelling

The wave modelling method has been presented and discussed. The method integrates a staggered-grid finite-difference scheme, a seismic energy source, a free surface, computational boundaries, and elastic subearth models. The modelling method simulates wave phenomena in isotropic elastic media with very general and complete models, so modelling results usually are faithful to wave propagation in the physical world. The modelling method is used in the dissertation not only as a part of the reverse-time migration algorithm, but also as a tool to understand wave phenomena and seismic theory. Potentially, the method can be used to design seismic surveys, predict seismic experiment results, enhance interpretation, do inversion, test processing algorithms, and examine data noise.

Computational boundary

A method to reduce computational boundary reflections is proposed. The method combines a nonreflecting boundary condition and absorbing boundary conditions. It generates fewer computational boundary reflections. The method is demonstrated in a staggered-grid scheme of a finite-difference algorithm, but it is readily applied in non-staggered grid algorithms.

Reverse-time migration

A prestack reverse-time migration for multi-component seismic data processing is formulated. The feature of the migration method includes the employment of staggered-grid finite-difference scheme, the source energy normalized imaging conditions, and the unique workflow.

First, with the employment of staggered-grid finite-difference schemes, the migration method has the potential advantage of handling solid-liquid boundaries better.

Second, source energy normalized imaging conditions are proposed. They result in less source effect than other imaging conditions. Both the strong-source effect of cross-correlation imaging conditions and the weak-source effect in source normalized imaging conditions are suppressed.

Third, the workflow is unique in some way. For example, noise attenuation in reverse-time migration is very different from traditional seismic data processing. As demonstrated in Section 4.4, ground roll suppression is not necessary. In addition, it is well understood that seismic multiples in surface records help image subsurface structures in reverse-time migration.

Computational resources

Intel® Threading Building Blocks (TBB) is utilized in parallel computing to solve the problem of long computational time. The limitation is that it is designed to utilize multi-cores on a same computer. However, it is convenient to incorporate this technique with distributed parallel computing methods.

Another challenge of computational resources is disk space. The solution is to do modelling twice instead of once.

6.2 Future directions

6.2.1 Further studies

Further studies on wave modelling and reverse-time migration would be irregular topography, efficient 3D implementation, modelling based on more advanced medium descriptions, and wavefield decomposition.

Irregular topography

The wave modelling and reverse-time migration methods developed in the dissertation assumes plain horizontal free surface, which is usually not true in real seismic surveys. It is necessary for one to integrate an irregular topography algorithm into the modelling method. Fortunately, this is an area of rich literature. For example, Perez-Ruiz et al. (2005) presented an excellent and detailed paper on this topic.

Efficient 3D implementation

Although some preliminary 3D modelling results are presented in Chapter 2, the efficiency needs to be improved. When subearth models are too large to be fully processed in the computer memory, it is very slow to use a disk buffer.

Advanced medium descriptions

The implemented wave modelling method is based on isotropic elastic earth description. Although an isotropic elastic model of the earth is much more accurate than an acoustic model, there are still more advanced models available.

Imaging conditions based on wavefield decomposition

The imaging conditions discussed are based on elastic wavefields without being decomposed into P and S waves. Research on imaging conditions based on wavefield decomposition is also an interesting direction.

6.2.2 Applying reverse-time migration to real data

The reverse-time migration developed in the dissertation has been applied to synthetic datasets. However, to apply the method to real data, one needs to consider the following issues in addition to the aspects of wave modelling mentioned above.

Subsurface model building

An accurate subsurface velocity model is critical for a migration process. Depth migration is more sensitive to errors in subsurface models than time migration.

Noise attenuation

Noise attenuation in reverse-time migration is very different from traditional seismic data processing. Noise attenuation in reverse-time migration should be despiking, white noise attenuation, anti-aliasing filtering, and so on, excluding ground roll and multiple attenuation.

Interpolation

The question about interpolation arises when one compares the fine grids in finite-difference methods to the sparsely and irregularly sampled real seismic data.

In order to get accurate modelling and reverse-time extrapolation results, common practice in the literature is to set spatial grid step to the level of $1m$ and time grid step to the level of $0.0001s$. Usually seismic records are sparsely and irregularly sampled. Does one need to interpolate the surface records to those fine meshes? The answer is no, according to Zhu and Lines (1997). “Fortunately, reliable interpolation of missing traces is implicitly included in the reverse-time wave equation computations. This implicit interpolation is essentially based on the ability of the wavefield to ‘heal itself’ during propagation.”

Thus, explicit interpolation is not necessary for a reverse-time migration algorithm to use sparsely and irregularly sampled seismic data as the input.

Efficient algorithms

A more efficient reverse-time migration workflow (Jiang, Bancroft, and Lines, 2010) is not incorporated in the dissertation. That method does not have the problem of high demand of disk space, so it is not needed to do modelling twice for reverse-time cross-correlation operation. That means almost one third less computation and almost no disk I/O operations.

Bibliography

Aki, K., and Richards, P. G., 2002, Quantitative Seismology: Theory and Methods: University Science Books.

Alterman, Z., and Karal, F. C., 1968, Propagation of elastic waves in layered media by finite difference methods: Bulletin of the Seismological Society of America, **58**, No. 1, 367–398.

Amdahl, G., 1967, Validity of the single processor approach to achieving large-scale computing capabilities: AFIPS Conference Proceedings, **30**, 483485.

Bancroft, J. C., 2006, A practical understanding of pre- and poststack migration: University of Calgary.

Bevc, D., and Palacharla, J. L. B. G., 1995, Plumes: Response of time migration to lateral velocity variation: Geophysics, **60**, No. 4, 1118–1127.

Biondi, B., and Shan, G., 2002, Prestack imaging of overturned reflections by reverse time migration: SEG Eightieth Annual Meeting Expanded Abstract, 1284–1287.

Black, J. L., and Brzostowski, M. A., 1994, Systematics of time-migration errors: Geophysics, **59**, No. 9, 1419–1434.

Bonham, K., Hall, K., and R.J., F., 2008, The epic of gilgamesh: CREWES' new cluster computer: CREWES Research Report, **20**, 70.1–70.12.

Bording, R., and Lines, L., 1997, Seismic Modeling and Imaging with the Complete Wave Equation: Society of Exploration Geophysicists publication, Tulsa, Oklahoma.

Cerjan, C., Kosloff, D., Kosloff, R., and Reshef, M., 1985, A nonreflecting boundary-condition for discrete acoustic and elastic wave equations: Geophysics, **50**, No. 4, 705–708.

Chang, W., and McMechan, G., 1986, Reverse-time migration of offset vertical seismic profiling data using the excitation-time imaging condition: Geophysics, **51**, No. 1, 67–84.

Chang, W., and McMechan, G., 1987, Elastic reverse-time migration: Geophysics, **52**, No. 10, 1365–1375.

Chattopadhyay, S., and McMechan, G. A., 2008, Imaging conditions for prestack reverse-time migration: Geophysics, **73**, No. 3, S81–S89.

Claerbout, J., 1971, Toward a unified theory of reflector mapping: Geophysics, **36**, No. 3, 467–481.

Clayton, R., and Engquist, B., 1977, Absorbing boundary-conditions for acoustic and elastic wave-equations: Bulletin of the Seismological Society of America, **67**, No. 6, 1529–1540.

Collino, F., and Tsogka, C., 2001, Application of the perfectly matched absorbing layer model to the linear elastodynamic problem in anisotropic heterogeneous media: Geophysics, **66**, No. 1, 294–307.

Du, Q., Zhu, Y., and Ba, J., 2012, Polarity reversal correction for elastic reverse time migration: Geophysics, **77**, No. 2, S31–S41.

Gavrilov, D., Lines, L., Bland, H., and Kocurko, A., 2000, 3-d depth migration:

parallel processing and migration movies: The Leading Edge, **19**, 1282–1284.

Gray, S. H., Etgen, J., Dellinger, J., and Whitmore, D., 2001, Seismic migration problems and solutions: Geophysics, **66**, No. 5, 16221640.

Haines, S. S., and Ellefsen, K. J., 2010, Shear-wave seismic reflection studies of unconsolidated sediments in the near surface: Geophysics, **75**, No. 2, B59–B66.

Ion, 2012, Application of reverse time migration to complex imaging problems, [Online; accessed 22-April-2012].

URL `http://www.iongeo.com/content/documents/Resource%20Center/Case%20Studies/CS_GXT_RTM_North_Sea_080201.pdf`

Jiang, Z., Bancroft, J. C., and Lines, L. R., 2010, Reverse-time migration imaging with/without multiples: CREWES Research Report, **22**.

Kaelin, B., and Guitton, A., 2006, Imaging condition for reverse time migration: SEG Eightieth Annual Meeting Expanded Abstract, 2594–2598.

Kelly, K. R., Ward, R. W., Treitel, S., and Alford, R. M., 1976, Synthetic seismograms - finite-difference approach: Geophysics, **41**, No. 1, 2–27.

Krebes, E. S., 2006, Seismic theory and methods: University of Calgary.

Levander, A., 1988, 4th-order finite-difference P-SV seismograms: Geophysics, **53**, No. 11, 1425–1436.

Leveille1, J. P., Jones, I. F., Zhou, Z.-Z., Wang, B., , and Liu, F., 2011, Subsalt imaging for exploration, production, and development: A review: Geophysics, **76**, No. 5, WB3WB20.

Lines, L. R., and Newrick, R. T., 2004, Fundamentals of Geophysical Interpretation: Society of Exploration Geophysicists publication, Tulsa, Oklahoma.

Loewenthal, D., and Hu, L., 1991, 2-methods for computing the imaging condition for common-shot prestack migration: Geophysics, **56**, No. 3, 378–381.

Long, L., and Liow, J., 1990, A transparent boundary condition for finite-difference wave simulation: Geophysics, **55**, No. 2, 201–208.

Manning, P. M., 2008, Techniques to enhance the accuracy and efficiency of finite-difference modelling for the propagation of elastic waves: Ph.D. thesis, The University of Calgary.

Martin, G., 2004, The Marmousi2 model, elastic synthetic data, and an analysis of imaging and AVO in a structurally complex environment.

Martin, G., Wiley, R., and Marfurt, K., 2006, Marmousi2: An elastic upgrade for Marmousi: The leading Edge, 156–166.

McMechan, G., 1983, Migration by extrapolation of time-dependent boundary-values: Geophysical Prospecting, **31**, No. 3, 413–420.

Ohminato, T., and Chouet, B., 1997, A free-surface boundary condition for including 3d topography in the finite-difference method: Bulletin of the Seismological Society of America, **87**, No. 2, 494–515.

Pei, Z., Fu, L.-Y., Sun, W., Jiang, T., and Zhou, B., 2012, Anisotropic finite-difference algorithm for modeling elastic wave propagation in fractured coalbeds: Geophysics, **77**, No. 1, C13C26.

Perez-Ruiz, J., Luzon, F., and Garcia-Jerez, A., 2005, Simulation of an irregular free surface with a displacement finite-difference scheme: Bulletin of the Seismological Society of America, **95**, No. 6, 2216–2231.

Ryan, H., 1994, Ricker, Ormsby; Klander, Butterworth - a choice of wavelets: CSEG recorder, 8–9.

Shearer, P. M., 1999, Introduction to seismology: Cambridge University Press.

Stephen, R., 1988, A review of finite-difference methods for seismo-acoustics problems at the seafloor: Reviews of Geophysics, **26**, No. 3, 445–458.

Stewart, R. R., Gaiser, J. E., Brown, R. J., and Lawton, D. C., 2002, Converted-wave seismic exploration: Methods: Geophysics, **67**, 13481363.

Sun, R., and McMechan, G., 1986, Pre-stack reverse-time migration for elastic-waves with application to synthetic offset vertical seismic profiles: Proceedings of the IEEE, **74**, No. 3, 457–465.

Sun, R., and McMechan, G., 1988, Nonlinear reverse-time inversion of elastic offset vertical seismic profile data: Geophysics, **53**, No. 10, 1295–1302.

Virieux, J., 1984, SH-wave propagation in heterogeneous media - velocity-stress finite-difference method: Geophysics, **49**, No. 11, 1933–1942.

Virieux, J., 1986, P-SV wave propagation in heterogeneous media: Velocity-stress finite-difference method: Geophysics, **51**, No. 4, 889–901.

Wang, Y., 2000, Variable grid-size and time-step finite difference method for seismic forward modeling and reverse-time migration: Ph.D. thesis, The University of Utah.

Whitmore, N., 1983, Iterative depth migration by backward time propagation: 53rd Annual International Meeting, SEG, Expanded Abstracts, 382385.

Whitmore, N., and Lines, L., 1986, Vertical seismic profiling depth migration of a salt-dome flank: Geophysics, **51**, No. 5, 1087–1109.

Widess, M. B., 1973, How thin is a thin bed: Geophysics, **38**, No. 6, 1176–1180.

Wikipedia, 2012, Amdahl's law — Wikipedia, the free encyclopedia, [Online; accessed 22-April-2012].
URL `http://en.wikipedia.org/wiki/Amdahl's_law`

Yan, J., and Sava, P., 2007, Elastic wavefield imaging with scalar and vector potentials: SEG San Antonio 2007 Annual Meeting Expanded Abstract, 2150–2154.

Zhu, J., and Lines, L., 1997, Implicit interpolation in reverse-time migration: Geophysics, **62**, No. 3, 906–917.